AD-A175 388 OPTICAL SIGNAL PROCESSING(U) HARRIS CORP MELBOURNE FL 1/1
GOVERNMENT SYSTEMS SECTOR A VANDERLUGT 31 OCT 86
ARO-20917.12-PH DAAG29-83-C-0033

UNCLASSIFIED F/G 20/6 NL

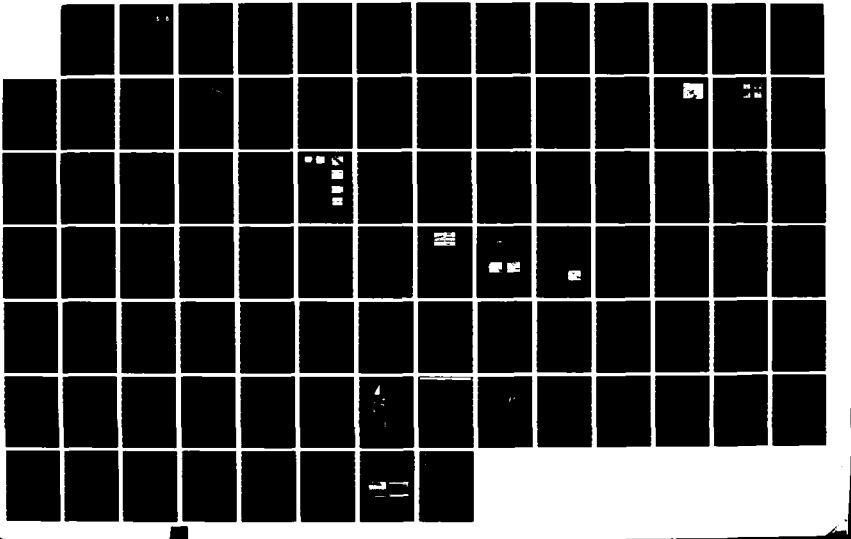

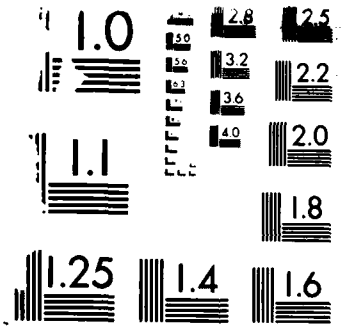

ARO 20917.12-PH

(2)

Optical Signal Processing

FINAL REPORT
20917-F

A. Vanderlugt

U.S. ARMY RESEARCH OFFICE

Contract No. DAAG29-83-C0033

31 October 1986

HARRIS

HARRIS CORPORATION GOVERNMENT SYSTEMS SECTOR
P.O. BOX 37, MELBOURNE, FLORIDA 32902, (305) 727-4000

UNCLASSIFIED

SECURITY CLASSIFICATION OF THIS PAGE (When Data Entered)

REPORT DOCUMENTATION PAGE		READ INSTRUCTIONS BEFORE COMPLETING FORM
1. REPORT NUMBER ARO 20917.12-PH	2. GOVT ACCESSION NO. N/A	3. RECIPIENT'S CATALOG NUMBER N/A
4. TITLE (and Subtitle) Optical Signal Processing		5. TYPE OF REPORT & PERIOD COVERED Final Report 1 Oct. 83 - 30 Sept. 86
		6. PERFORMING ORG. REPORT NUMBER
7. AUTHOR(s) A. VanderLugt		8. CONTRACT OR GRANT NUMBER(s) DAAG29-83-C-0033
9. PERFORMING ORGANIZATION NAME AND ADDRESS Harris Corporation Government Systems Sector Melbourne, FL 32902		10. PROGRAM ELEMENT, PROJECT, TASK AREA & WORK UNIT NUMBERS
11. CONTROLLING OFFICE NAME AND ADDRESS U. S. Army Research Office Post Office Box 12211 Research Triangle Park, NC 27709		12. REPORT DATE 31 October 1986 13. NUMBER OF PAGES
14. MONITORING AGENCY NAME & ADDRESS(if different from Controlling Office)		15. SECURITY CLASS. (of this report) Unclassified 15a. DECLASSIFICATION/DOWNGRADING SCHEDULE

16. DISTRIBUTION STATEMENT (of this Report)

Approved for public release; distribution unlimited.

17. DISTRIBUTION STATEMENT (of the abstract entered in Block 20, if different from Report)

NA

18. SUPPLEMENTARY NOTES

The view, opinions, and/or findings contained in this report are those of the author(s) and should not be construed as an official Department of the Army position, policy, or decision, unless so designated by other documentation.

19. KEY WORDS (Continue on reverse side if necessary and identify by block number)

Optical signal processing, interferometric spectrum analyzers, Bragg cells, adaptive optical processing, transversal filtering, acoustic spreading in Bragg cells, Fresnel Transforms, optical switches.

20. ABSTRACT (Continue on reverse side if necessary and identify by block number)

We developed new analytical tools for predicting the performance of adaptive optical processors using feedback. Such systems are potentially unstable; new computer simulations were developed to model the instabilities and to guide corrective modifications of the hardware. We also developed new diagnostic tools that helped measure the complex valued impulse response of the system. We achieved notch depths of more than 32 dB over a 50 MHz bandwidth with an optical sytem having the equivalent of 500 tap weights. We also

DD FORM 1 JAN 73 1473 EDITION OF 1 NOV 65 IS OBSOLETE

UNCLASSIFIED

SECURITY CLASSIFICATION OF THIS PAGE (When Data Entered)

studied a generalization of the crossed Bragg cell architecture often used in signal processing. We derived the necessary geometry to obtain correlation functions that have an arbitrary spatial or an arbitrary temporal scaling; with these geometrics the optical processors can perform a wider variety of operations.

We analyzed the properties that a reference waveform needs to function as a distributed local oscillator in heterodyne spectrum analyzers. The key finding is that the temporal spectrum of the reference bias term may contribute energy in the passband of interest, thereby reducing the dynamic range. We introduce the concept of the mixed transform that accurately represents the spatial and temporal structure of the reference waveform. We found that these effects can be controlled by placing a harmonic of the periodic reference waveform at the center of the passband and then to control its level through aperture weighting of the Bragg cell.

We performed an analysis of Fresnel transforms and their application to processing real-time signals. Such transforms are space/time variant and, although difficult to analyze in a general sense, have useful properties for scrambling wideband analog signals. We also show how arbitrary permutations, cincluding the perfect shuffle, can be performed on frames of digital data. These permutations suggest ways to use the Fresnel transform and Bragg cells to implement a dynamic optical switch that can connect N input parts to N output parts in an arbitrary configuration.

OPTICAL SIGNAL PROCESSING

FINAL REPORT
20917-F

A. VANDERLUGT

31 OCTOBER 1986

U. S. ARMY RESEARCH OFFICE

DAAG29-83-C-0033

HARRIS CORPORATION
GOVERNMENT SYSTEMS SECTOR
MELBOURNE FLORIDA, 32902

TABLE OF CONTENTS

LIST OF APPENDICES

OPTICAL SIGNAL PROCESSING

1.0 INTRODUCTION

As the bandwidth of signals increase and as the electromagnetic environment becomes increasingly dense, processing operations such as convolution, spectrum analysis, correlation, ambiguity function generation and filtering become computationally intensive operations. Optical systems have the capability to perform a large number of complex multiplications and additions per unit time. As the bandwidth increases, the number of computations increase as the square of the bandwidth because the degrees of freedom of the signal is linearly proportional to bandwidth and the allowable computational time interval is a inversely proportional to bandwidth. Optical processing provides high-speed, parallel computations so that digital post-processing techniques can be used for lower-speed, serial computation.

The research effort described in this report has resulted in several innovative optical processing techniques for improved performance; it covers the three-year period from 1 October 1983 to 30 September 1986. The major accomplishments can be divided into three areas: (1) adaptive optical processing based on transversal filtering with feedback, (2) reference beam waveforms for interferometric spectrum analyzers, and (3) Fresnel transforms for signal scrambling and optical switching. In the following paragraphs, we summarize the key results in each area; further details can be found in the referenced journal articles that have been published and included in the Appendices.

2.0 Adaptive Optical Processing

The basic theory for an adaptive optical processor that uses transversal filtering techniques was developed under Contract No. DAAG29-80-C-0149 and reported in Reference 1. Under the current contract, we performed additional analytical and experimental work to gain further insight into the process and to validate the theory. In this processor the Bragg cells are arranged in an orthogonal configuration to produce the cross-product of two optical signals. Bragg cells used for processing wideband signals are typically used in one of three configurations: (1) the cells are parallel and the signals propagate in the same direction, (2) the cells are parallel and the signals counter-propagate with one signal being

time-reversed, or (3) the cells are orthogonally oriented to better use the two-dimensional processing power of the optical system.

We studied the generalized case of two Bragg cells crossed at an arbitrary angle to seek ways to increase the flexibility of the processing operations. The two main objectives were to find configurations for which the spatial scaling of the correlation function can be varied and for which the time compression factor can be controlled. The first objective is gained by changing the angle between the two cells. For example, when the angle is 60 degrees, the spatial scale factor is unity so that no magnification changes are needed when further processing operations are done. An arbitrary time compression factor can be achieved if the stored reference signal is clocked at a rate different from that of the received signal. As a result, signal acquisition can be achieved without the need to time-reverse one of the signals (a significant advantage), the correlation function is displayed in space, and the time compression factor can be made to be unity. More detailed results of this analysis are given in Reference 2; a reprint is included in Appendix A.

The stability of optical systems using feedback is a critical issue that must be resolved. The application we studied is adaptive notch filtering for use in signal excision. To date there have been no published results showing high performance levels; the problem is that the systems are very difficult to stablize. We attacked this problem by developing new analytical models that more accurately account for the analog nature of the processing operation. We first developed diagnostic tools to measure the state of the system. Since measurements in the closed loop mode perturb the system response, we probed the system response in the open loop mode; in effect, we measured the envelope of the impulse response of the system directly. We also developed a novel diagnostic tool to measure complex valued frequency response of the system. In most physical systems the impulse response is, of course, real valued; in optical systems, however, aberrations can contribute a phase term to the impulse response. From these measurements, then, we identified and corrected a serious phase aberration in the impulse response of one of the Bragg cells.

The key analytical tools are new models that more accurately predict the system transient response as well as the notch depth. We developed several computer simulations, taking great care to account for anomalies

introduced by discrete sampling, to numerically calculate the optimum impulse response for a given level of phase or gain margin desired for system stability. An interesting and important result is that the optimum impulse response under a strong stability constraint is a linear taper from t = 0 to t = T, where T is reciprocally related to the required notch bandwidth. We then found a closed form analytical solution that confirmed the validity of the simulations and showed that a phase stability margin of 90° could be obtained, with no loss in notch depth; this allows the system to operate with realistic error budgets.

As a result of the interaction between the analytical and experimental results, we increased the notch depth to 32 dB where it is presently limited by a combination of insufficient laser power and photodetector sensitivity. The system as configured has a bandwidth of 50 MHz and a notch bandwidth of the order of 200 KHz so that the system has the equivalent of 500 tap weights. This combination of a large number of taps and a wide bandwidth is the chief advantage of the optical approach. Details of this work are given in References 3, 4, and 5; reprints of these papers are included as Appendices B, C and D.

3.0 Reference Waveforms for Heterodyne Spectrum Analyzers

We previously developed the use of a distributed local oscillator, generated by a reference wavefront, that provides for heterodyne detection of spatial frequencies. We further analyzed the necessary properties of the reference waveforms. The motivation for this study was that unwanted energy from the reference beam bias term may be present in the bandpass of the filter, along with the desired signal. We studied the case of a generalized periodic reference waveform having equal Fourier coefficients within the band limit of the Bragg cell. Since the spatial frequency output of the spectrum analyzer is subjected to further processing, we defined a mixed transform of the reference signal that characterizes it in terms of both spatial and temporal frequencies. The first key result is that the magnitude of the mixed transform is completely independent of the specific waveform of a repetitive reference signal. This means that impulse trains, pseudorandom sequences, and chirp waveforms all have the same mixed transform. A direct consequence of this result is that the duty cycle of, for example, a chirp waveform has no effect on the form of the

mixed transform; a high duty cycle chip is preferred to efficiently use the available laser power.

A second important result is that the aperture weighting function, which includes the amplitude profile of the illuminating beam, the acoustic attenuation and the size limitations of the Bragg cell, can be used to control spurious modulation introduced by the reference bias term. The spurious modulation is caused by higher order harmonics of the periodic reference waveform that are in the passband of the filter. If we cause one of the harmonics to be coincident with the center frequency of the filter and simultaneously use the aperture weighting function to create a null at this temporal frequency, the spurious modulation can be reduced significantly. Although it may seem strange that spatial frequency nulls correspond directly to temporal frequency nulls, this result is also predicted by the analysis. In particular, we showed that the spatial aperture weighting function is, for certain periodic signals, also imposed on the output signal as a temporal modulation. This conversion of spatial to temporal modulation can be easily visualized for a chirp waveform because each spatial frequency component travels underneath the aperture weighting function.

We also analyzed spurious modulation for a chirp waveform that has a fixed phase increment from pulse-to-pulse. This waveform leads to a mixed transform in which the harmonics, in both space and time, are not integer multiples of the fundamental repetition frequency. The improved performance obtainable as a result of this analysis, as well as other details of the study, have been published in Reference 6 and is included as Appendix E.

A related activity was the start of a study of a class of architectures, used for heterodyne spectrum analysis, that require fewer photodetector array elements. In such systems the high performance is obtained by using an array of discrete elements; each element is followed by a preamp, a bandpass filter, a nonlinear device, a rectifier and a low pass filter. As a result of this complexity, arrays having large numbers of elements (more than 100) are unattractive. We can trade some system performance by decimating the array and scanning the spectrum across the remaining elements. We thereby time-multiplex the spatial frequency

information onto the detector elements. The basic tradeoffs are in terms of laser power and dynamic range.

4.0 Fresnel Transforms for Signal Scrambling and Optical Switching

The analysis of signal processing systems is generally performed using either time or frequency domain concepts. In optical systems the Fourier transform plane physically exists, so that operations such as spectrum analysis or correlation can be performed by placing photodetectors in the Fourier domain. Between the time (or space) plane and the Fourier plane there are a continum of Fresnel transform planes. Detailed analyses of systems using Fresnel transforms are not usually made since these systems are space- or time-variant. It is often difficult, therefore, to obtain results that are as generally applicable as those obtained from Fourier transform theory.

We performed an analysis of the use of Fresnel transforms and their application to processing real-time signals in a Bragg cell processor. The initial motivation for this study was the question of how to scramble or protect wideband analog signals without bandwidth expansion. The normal technique of digitizing and coding the signal results in significant transmission channel bandwidth expansion. Scramblers that segment the signal into frequency bins and rearrange the frequency components have been shown, at least in the audio range, to be relatively ineffective. Rearranging the time samples seems to be more effective, but requires a storage device so that a frame of information can be processed without losing information.

Since the Fresnel transform plane in an optical system lies between the equivalent time plane and other frequency plane, the question arises whether techniques can be developed for analog signal protection that share some of the features of time and frequency scrambling. We find that, given the constraint of real-time processing, we can obtain a signal that is dependent on both the time and frequency structure of the signal. The major phenomena induced by the Fresnel transform is a dispersion of the elements of the signal; the space-variance of the system can then be used to introduce some random coding schemes such as time perturbations that are frequency dependent. Additional scrambling techniques are available if some bandwidth expansion is allowed; considerable bandwidth expansion can, of course, be tolerated before we reach that required for full digitization.

It is also possible to perform arbitrary permutations on blocks of information, including the so-called perfect shuffle. Details of this work were published in Reference 7 and a reprint is included in Appendix F.

The fact that permutation can be achieved suggest ways that the Fresnel transform can be applied to optical computing. Since the Fresnel transform is a space/time variant transform, the response to a short pulse is a function of both its time-of-arrival and its frequency. One way to take advantage of this property is to permute a data sequence to implement operations such as shuffles, exchanges and bypasses. A wide range of algorithms can be implemented by these operations.

Another possibility is to use the Fresnel transform to implement a NXN non-blocking crossbar switch. Such a switch might have, as its input, an N-element fiber optic array representing the communication links to N processors, for example. By using the Fresnel transform in conjunction with Bragg cell processor, we can connect these N input ports to N output in a completely arbitrary fashion. Furthermore, we can accomplish the interconnection very rapidly and without the need for multiple passes through replicated switches, as is often needed in electronic switches. Multiple connections from one input port to many output ports (fan out) can be made, as well as the complementary connection (fan in). Details of this work are given in Reference 8 and a preprint is given in Appendix G.

5.0 Miscellany

A paper entitled "Acoustic Spreading in Multichannel Bragg cells was presented at an SPIE Conference on Spatial Light Modulators and Applications. This work was based on work already reported in Reference 1; we include a reprint of the paper in Appendix H and it is listed as Reference 9.

During the week of 4 November 1985, A. VanderLugt, along with Dr. B. D. Guenther of the U. S. Army Research Office, co-chaired a Palantir Study on the Role of Photodetectors in Optical Signal Processing. Other panel members were Dr. G. W. Anderson from NRL, Dr. J. Hynecek from Texas Instruments, and Dr. R. J. Keys from Lincoln Laboratories. Photodetectors have historically been developed for image sensing applications. We focused on two key needs for optical processing: more dynamic range and on-chip processing to reduce the output transfer rate. The committee has started to prepare a paper based on the results of this study.

During this contract, A. VanderLugt visited Dr. Graeme Duthie and Dr. Jay Loomis at MICOM to discuss potential applications of optical processing to phased array antenna systems.

6.0 Scientific Personnel

The principal investigator on this contract was A. VanderLugt. A. M. Bardos, Senior Scientist, and W. R. Beaudet, Associate Principal Engineer, assisted in some portions of the work and were partially supported by this contract.

7.0 References

1. Optical Signal Processing, U. S. Army Research Office, Final Report, No. 17614-F, 30 November 1980.
2. A. VanderLugt, "Crossed Bragg Cell Processors," Applied Optics, Vol. 23, p. 2275 (1984).
3. A. M. Bardos, W. R. Beaudet, and A. VanderLugt, "Stability Considerations for Adaptive Optical Filtering," Applied Optics, Vol. 25, p. 2314 (1986).
4. A. M. Bardos, "Optical Adaptive Filter; Analytical Model," Proc. SPIE, Optical Information Processing II, Vol. 639, in Press.
5. W. R. Beaudet, A. M. Bardos, and A. VanderLugt, "Optical Adaptive Filter; Experimental Results," Proc. SPIE, Optical Information Processing II, Vol. 639, in Press.
6. A. VanderLugt and A. M. Bardos, "Spatial and Temporal Spectra of Periodic Functions for Spectrum Analysis," Applied Optics, Vol. 23, p. 4269 (1984).
7. A. VanderLugt, "Fresnel Transforms and Bragg Cell Processors," Applied Optics, Vol. 24, p. 3846 (1985).
8. A. VanderLugt, "Fresnel Transforms and Optical Computing," SPIE Advanced Institute on Hybrid and Optical Computing, Leesburg, Virginia, March 1986.
9. A. VanderLugt, G. S. Moore, and S. S. Mathe, "Acoustic Spreading in Multichannel Bragg Cells," Proc. SPIE, Spatial Light Modulators and Applications, Vol. 465, p. 152 (1984).

APPENDIX A

CROSSED BRAGG CELL PROCESSORS

REPRINTED FROM APPLIED OPTICS

VOLUME 23, PAGE 2275, JULY 15, 1984

Reprinted from Applied Optics, Vol. 23, page 2275, July 15, 1984

Crossed Bragg cell processors

A. VanderLugt

In optical signal processing applications, two Bragg cells are sometimes crossed at an angle to display a correlation function in space. In this paper we show how the angle can be adjusted to control the scale of the correlation function. For signal acquisition, the received signal and the reference signal must be synchronized electronically. If the reference signal is time-reversed, the crossed cell geometry displays the correlation function in both space and time so that the optical system indicates the time at which the signals are synchronized. If the reference signal has a clock rate difference relative to the received signal, the correlation function still exists in both space and time but with the additional advantage that acquisition can be obtained without the need to time-reverse the reference signal.

I. Introduction

Bragg cells can be used in many different configuration to implement various signal processing operations. The most common way to use two Bragg cells for implementing correlation is to orient them so that the acoustic waves propagate in either the same or opposite directions.[1-4] If the waves propagate in the same direction, only a single value of the correlation function $c(\tau)$ is obtained. Furthermore, the peak value of the correlation function is obtained only if the two signals arrive at the Bragg cell transducers at the same time. In a signal acquisition application, a received signal must be synchronized with a reference code signal. The acquisition process may require a significant amount of time as the reference code is stepped through all possible values in the search for $c(0)$. The search can also be done in a continuous fashion by increasing the rate of the reference signal slightly; the process is still slow, however, since the time scale also changes, and the rate difference must be kept well under 1% to maintain the correlation peak value for highly structured codes.

When the two Bragg cells are oriented at some arbitrary angle θ, the correlation function is displayed in space instead of time. Said and Cooper[5] described a cross-path optical correlator wherein the Bragg cells were oriented at 45°. A more common method is to orient the Bragg cells orthogonally to achieve correlation or ambiguity function generation.[6-9] In these configurations, the scale of the correlation function is dependent on θ, and the tolerance on having the signals precisely synchronized is somewhat relaxed. Nevertheless, the time delay between the two signals cannot exceed certain bounds established by the angle θ. We will examine further these relationships and other implications of the crossed cell geometry in detail.

An alternative method to achieve signal acquisition is to time-reverse the reference signal and orient the Bragg cells so that the signals counterpropagate. The full range of possible time delays is thereby displayed sequentially so that, at some instant in time, the correlation peak is detected. The correlation function is compressed in time by a factor of 2 when using this geometry, which may place severe bandwidth requirements on the photodetectors when the signals are wideband. When the two Bragg cells are oriented at an arbitrary angle for the counterpropagating geometry, the correlation function is also displayed in both space and time. The correlation function propagates at a rate that always maintains the time compression factor of 2, however.

A third method for achieving signal acquisition that combines several advantages of the first two is a crossed cell geometry wherein the reference code is generated at a clock rate different from that of the received signal. There is no need to time-reverse the reference signal. The correlation function is displayed in space with a scale that is dependent on both the angle θ and the rate difference. The correlation function flows through the system at a rate that can be controlled by the reference code clock.

In this paper we first consider the results obtained for Bragg cells oriented at an arbitrary angle. The acoustic waves initially propagate in the same direction, but if the angle is >90°, a counterpropagating component is introduced. We then consider the general case for

The author is with Harris Government Systems Sector, Advanced Technology Department, P.O. Box 37, Melbourne, Florida 32902.
Received 27 December 1983.
0003-6935/84/142275-07$02.00/0.

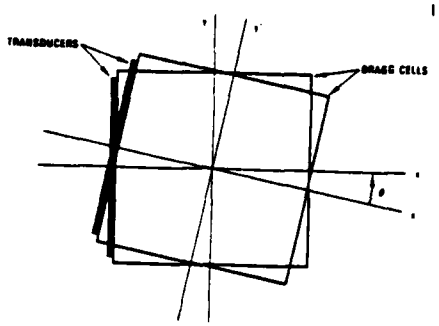

Fig. 1. General crossed-cell geometry.

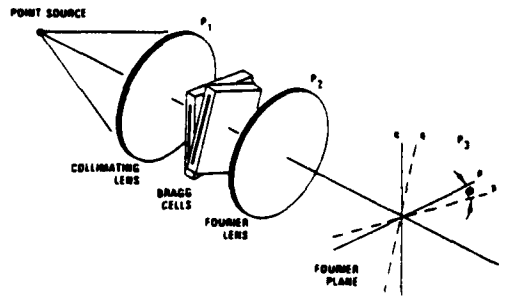

Fig. 2. Fourier transform of crossed cells.

counterpropagating signals with the reference signal being time-reversed. The final topic is that of driving the reference code signal at a different rate from that of the received signal.

II. General Crossed Cell Geometry

The correlation function for two signals $f(t)$ and $g(t)$ plays a central role in signal acquisition and other processing applications; it is defined as

$$c(\tau) = \int_{-\infty}^{\infty} f(t)g(t+\tau)dt, \tag{1}$$

and its Fourier transform is

$$C(\omega) = F(-\omega)G(\omega). \tag{2}$$

Both signals must have finite durations for Eq. (2) to be defined.

The general geometry for the crossed Bragg cells is shown in Fig. 1. We make several assumptions to simplify the geometry and analysis. First, we show the Bragg cells as though they are in contact; generally one Bragg cell will be imaged onto the other with suitable intervening optics. Second, we show the cells with the transducer height equal to the length of the cell. This is normally not done in practice, but the same effect can often be achieved by the intervening optics. Third, we will not consider how the Bragg illumination angles are influenced by the use of a carrier frequency. We will drop the carrier frequency from the analysis and assume that the signals are at baseband. The most important results of the analysis are thereby preserved.

Suppose that $f(t)$ is applied to the first Bragg cell so that the acoustic wave propagates in the positive x direction. In the y direction the acoustic wave has a constant value. The signal $g(t)$ is applied to the second Bragg cell oriented at an angle θ with respect to the first cell; $g(t)$ propagates in the x' direction. Within the boundary defined by the overlapping area of the two cells, the diffracted amplitude transmittance function is given by $f(t - T/2 - x/v)g(t - T/2 - x'/v)$, where T is the time delay associated with the Bragg cell and v is the velocity of the acoustic wave.

We can obtain the function $C(\omega)$ by producing the 2-D Fourier transform of the amplitude transmittance along with an equivalent integration operation. Figure 2 shows a Fourier transform system for the crossed Bragg cells. Collimated light from a coherent source illuminates the two cells, and, given the assumptions listed above, the Fourier transform $A(p,q,t)$ is centered on the optical axis:

$$A(p,q,t) = \iint_{P_1} f(t - T/2 - x/v)g(t - T/2 - x'/v) \times \exp[j(px + qy)]dxdy. \tag{3}$$

The variables p and q in plane P_3 are radian spatial frequencies, and the region of integration is over the overlapping area of the Bragg cells in plane P_1. We now want to show that, for some region in plane P_3, we obtain the result that $A(p,q,t) \propto F(-\omega)G(\omega)$. We use a coordinate transformation in plane P_1 for which

$$\begin{aligned} x' &= x\cos\theta - y\sin\theta, \\ y' &= x\sin\theta + y\cos\theta, \end{aligned} \tag{4}$$

and a similar coordinate transformation in plane P_3 for which

$$\begin{aligned} p &= p'\cos\phi - q'\sin\phi, \\ q &= p'\sin\phi + q'\cos\phi. \end{aligned} \tag{5}$$

In plane P_1, θ is the angle from the x' axis to the x axis, whereas in plane P_3, ϕ is the angle from the p axis to the p' axis. If we substitute Eqs. (4) and (5) into Eq. (3), we have that

$$\begin{aligned} A(p',q',t) = \iint_{P_1} & f(t - T/2 - x/v) \\ & \times g\left(t - T/2 - \frac{x}{v}\cos\theta + \frac{y}{v}\sin\theta\right) \\ & \times \exp\{j[x(p'\cos\phi - q'\sin\phi) \\ & + y(p'\sin\phi + q'\cos\phi)]\}dxdy. \end{aligned} \tag{6}$$

We can separate Eq. (6) into the product of two integrals by first integrating on y and then on x to get $A(p',q',t) = B_1(p',q',t)B_2(p',q',t)$. The integrals are

$$B_1(p',q',t) = \frac{v}{\sin\theta}\exp[-ja(t - T/2)]\int q(u)\exp(jau)du, \tag{7}$$

$$B_2(p',q',t) = -v\exp[jb(t - T/2)]\int f(r)\exp(-jbr)dr, \tag{8}$$

where

$$\begin{aligned} a &= \frac{v}{\sin\theta}(p'\sin\phi + q'\cos\phi), \\ b &= v\left[p'\left(\cos\phi + \frac{\sin\phi}{\tan\theta}\right) - q'\left(\sin\phi - \frac{\cos\phi}{\tan\theta}\right)\right]. \end{aligned} \tag{9}$$

We note at this point that the integrals in Eqs. (7) and (8) are the Fourier transforms of $g(t)$ and $f(t)$ with the

product being of the form $F(+b)G(-a)$; the variables a and b are functions of p', q', and θ and ϕ. One condition that we impose is that both transforms must have the same frequency scale. This means that $|a| = |b|$ for all values of p' and q' as well as for all values of ϕ, given the value of θ. If we equate the coefficients of p' and q' from Eqs. (9), we find that the frequency scale is equal in magnitude when $\phi = -\theta/2$. A second condition is that the Fourier transform must be a function of either p' or q'; if we evaluate the integrals along the line $p' = 0$, we obtain the result that $a = b = -vq'/2 \sin\phi$. When this value is used in Eqs. (7) and (8), and we form the product of the two integrals, we have

$$A(q') = \frac{-v^2}{\sin\theta} \int g(u) \exp(-jq'vu/2 \sin\phi)du \times \int f(r) \exp(jq'vr/2 \sin\phi)dr; \quad \theta \neq 0. \tag{10}$$

If $\theta = 0$, the value of $A(p',q',t)$ can be obtained from Eq. (6) directly. The form of Eq. (10) shows that the scale, or measure, of the frequency variable is a function of the angle ϕ. Furthermore, since the product $q'v$ is equivalent to a temporal frequency variable, we define $\omega = q'v/2 \sin\phi$. We then find that $A(\omega) \propto F(-\omega)G(\omega)$, which is what we wished to show.

The result given by Eq. (10) reveals a number of interesting features. First, the relationship of $A(\omega)$ to $C(\omega)$, as given by Eq. (2), is clear. Second, the frequency scaling is a function of the angle θ. Third, evaluating Eq. (6) along the line $p' = 0$ is equivalent to integrating the space function in plane P_1 along lines parallel to the bisector of the angle θ. Fourth, since Eq. (10) does not contain any time factors, the correlation function is fixed in space at plane P_1. Some of these features become more apparent if we examine the equivalent operations in the space plane.

Figure 3 shows the Bragg cells crossed at $\theta = 45°$. We represent the duration of the independent time samples along the Bragg cells by T_0. As we noted above, evaluating Eq. (6) along the frequency axis $p' = 0$ is equivalent to integrating the cross product of $f(t)$ and $g(t)$ along lines parallel to the bisector of θ. The intersection of the time samples are parallelograms; the appropriate samples corresponding to no relative time delay between the two signals are shown as shaded areas. We can represent a time delay axis by extending the line of integration to some convenient point outside the overlapping region and by drawing a line perpendicular to the line of integration. We note that these two lines form an angle ϕ with respect to the original x and y axes. The intersection of these two constructed lines represents the point at which the value $c(0)$ occurs.

The basic reason for using a crossed-cell geometry is to display the correlation function in space instead of time. We must be careful, therefore, to establish a notation that connects space coordinates with time-delay coordinates. For example, as the signals propagate through the Bragg cells, the amplitudes at each sample position along the Bragg cells change. The correlation function, however, does not propagate as a function of time; the line of integration representing no

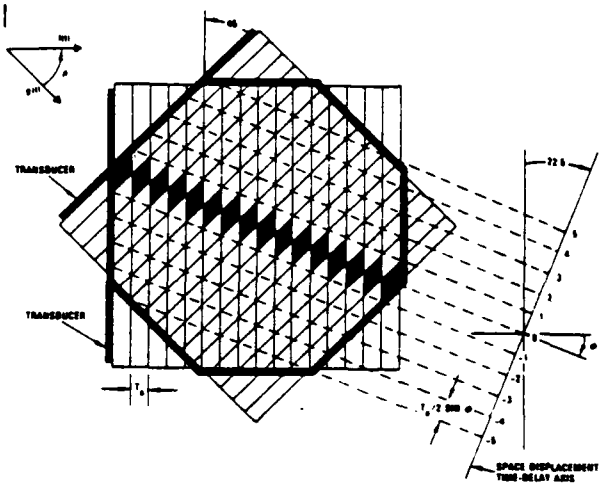

Fig. 3. Cells crossed at 45°.

relative time delay always passes through the origin about which the Bragg cell is rotated. As a result, in one sense it is appropriate to represent the time delays along a space-displacement axis as shown in Fig. 3. However, I prefer to retain an explicit time domain notation and will generally refer to the space-displacement axis as the time delay or τ axis.

The physical spacing of the τ values can be related to T_0 through the observation that if $g(t)$ is delayed by one time sample T_0 relative to $f(t)$, the shaded area representing the correlation peak line is shifted upward so that the intersection with the τ axis now occurs at

$$\tau_d = T_0/2 \sin\phi; \quad 0 \leq \phi \leq 90°. \tag{11}$$

This relationship is consistent with the formulation given by Eq. (10); if the frequencies are compressed or expanded by a scale factor of $2 \sin\phi$, the scale of the τ axis must be expanded or compressed by the same factor.

We note that, if $\tau = 0$, the number of samples that contribute to $c(\tau)$ changes. The integration is over the octogonal boundary defining the region of overlap. The effect of this integration is the same as that of a weighting function whose general normalized form, given in terms of τ, is

$$w(\tau) = 1 - \frac{2|\tau|}{T} \sin\phi, \ |\tau| \leq \frac{T}{2\cos\phi(1 + \tan\phi)};$$
$$= \left(1 - \frac{2|\tau|}{T} \cos\phi\right) \Big/ \tan\phi, \ \frac{T}{2\cos\phi(1 + \tan\phi)} \leq |\tau| \leq \frac{T}{2\cos\phi};$$
$$= 0, \ |\tau| \geq \frac{T}{2\cos\phi}, \tag{12}$$

where T is the total time duration of the Bragg cell.

The weighting function is shown in Fig. 4 for several values of ϕ. For $\phi = 0$ the boundary becomes a square, and the weighting function is rectangular over the interval from $-T/2$ to $T/2$. For $\phi = 45°$, the boundary is a diamond, and the weighting function is triangular over the interval $-T/\sqrt{2}$ to $T\sqrt{2}$. At all other values of $0 < \phi < 45°$, the weighting function consists of two straight line segments as indicated by Eq. (12). If θ

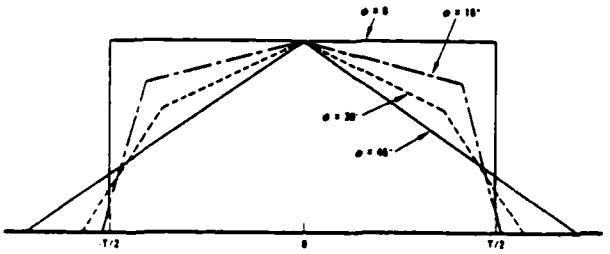

Fig. 4. Weighting function due to region of integration.

exceeds 90° so that $\phi > 45°$, Eq. (12) is no longer valid. The weighting function can be readily found, however, by substituting $(90° - \phi)$ for ϕ in Eq. (12) when $\phi > 45°$.

The weighting function is related to the physical boundaries of the Bragg cells. We must use Eq. (11) to determine how many values of τ occur within the weighting function as given by Eq. (12). For example, if $\phi = 0$, Eq. (11) shows that τ_d is infinity. Therefore, within the weighting function given in Fig. 4, there is only one time delay value available so that the correlation peak occurs only when the signals are synchronized electronically.

We can find the number of τ samples for any other value of ϕ by noting that the zero values of the weighting function occur at $T/2 \cos\phi$ for $0 \le \phi \le 45°$ and at $T/2 \cos(90 - \phi)$ for $45° \le \phi \le 90°$. Since $T = 2NT_0$, where N is the time–bandwidth product, we can use Eq. (11) to find that the number of τ increments is

$$\begin{aligned} N_\tau &= 2N \tan\phi; \quad && 0 \le \phi \le 45°, \\ &= 2N; && 45° \le \phi \le 90°. \end{aligned} \tag{13}$$

This result shows that for values of $\phi < 45°$ we do not generate all possible τ values. In some applications involving the correlation of wideband signals, only a few values near $\tau = 0$ may be necessary to achieve the desired results.

Some examples of special interest will now be examined. The first case is when there is no rotation of the Bragg cells so that $\theta = \phi = 0$. We return to Eq. (6) and find, after a change of variables, that

$$A(0,q',t) = c \operatorname{sinc}(q'vT/2) \int f(u)g(u)du, \tag{14}$$

where c is a constant. In terms of Fig. 3, the integration is along lines parallel to the direction of propagation, and the weighting function, as shown in Fig. 4, is constant over the extent of the Bragg cells. The integration in the vertical direction produces the sinc-function, so that Eq. (14) has the form of $c(\tau)$ if the photodetector in plane P_3 is located at $p' = q' = 0$. Only a single value of τ is thereby obtained; if the two signals are synchronized, the value is that corresponding to $\tau = 0$. If the signals are not synchronized, the light amplitude at $p' = q' = 0$ is proportional to $c(\tau)$, where τ now represents the time delay between the two signals. If the received signal is Doppler shifted and the signals are not at baseband, the correlation value will occur at some other value of p'. Thus all the information concerning two Bragg cells having signals propagating in the same direction can be derived from the general case.

If we now allow θ to increase, we find that more time delay values become available. To help visualize how the correlation function develops, it is useful to make transparencies of the signal histories and to overlay them at various angles as illustrated in Fig. 3. For example, when $\theta = 60°$ we find that the scales of the τ axis is exactly the same as the time scale as indicated by Eqs. (10) and (11). This may be a useful feature in some applications where we wish to perform a double correlation directly by the use of a third Bragg cell. Since the time scales are the same, no change in magnification is needed. Unfortunately, implementing a geometry in which $\theta = 60°$ is generally not feasible in systems that use 1-D Bragg cells.

It is feasible to orient the two Bragg cells at $\theta = 90°$ so that $\phi = 45°$. We then find that the full range of τ values is available as shown by Eq. (13). The correlation function $c(\tau)$ occurs (after integration) along a line inclined at 45° to the vertical axis, and, in the frequency plane, $C(\omega)$ lies along the q' axis, which is at 45° to the vertical axis. The scaling of the τ axis is compressed by a factor of $\sqrt{2}$ relative to the real-time scale; the Fourier transform, in turn, is expanded by the same factor. As a result, further processing involving $c(\tau)$ or $C(\omega)$ may require some magnification changes.[8,9]

If we let $\theta > 90°$, we begin to note some interesting features. First, the scale of the τ axis continues to compress according to Eq. (11). Second, the weighting function is similar to those shown in Fig. 4; if $\theta = 120°$, the appropriate $w(\tau)$ is that for $\phi = 30°$. Third, the full range of τ values is displayed as indicated by Eq. (13). Although the two acoustic waves now have a counterpropagating component, a correlation function can still be obtained, and it is stable in space. The peak value decreases, however, as θ increases because fewer cross-product terms contribute to the correlation. From geometric considerations we find that the number of cross products contributing to the correlation peak at $\tau = 0$ is

$$\begin{aligned} M &= 2N, && 0 \le \phi \le 45°; \\ &= 2N/\tan\phi, && 45° \le \phi \le 90°. \end{aligned} \tag{15}$$

We could incorporate the reduction in the correlation peak by dividing the weighting function $w(\tau)$ by $\tan\phi$ for $45 \le \phi \le 90°$. In terms of the functions shown in Fig. 4, the amplitudes would then be scaled by $1/\tan\phi$ when θ exceeds 90°.

Figure 5 summarizes how some of the key parameters vary as a function of the rotation angle. The number of τ values increases from 0 to $2N$ as the angle increases from 0 to 90°; the number remains constant thereafter. The number of cross products is fixed at $2N$ until θ reaches 90°; the number then decreases to zero as θ reaches 180°. The reciprocal of the ratio of the τ sample spacing to the time-delay spacing increases from 0 to 2 (right-hand scale) as θ increases from 0 to 180°. In all cases the correlation function is a pure space function even though the two waves may have a counterpropagating component; it is a function of time only to the extent that the signal statistics are not stationary.

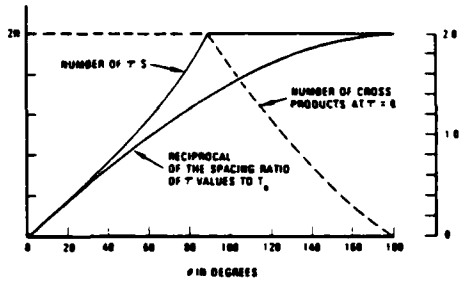

Fig. 5. Key performance parameters as a function of angle.

III. Time-Reversed Signals

When θ exceeds 90°, we found that the number of cross-product terms decreases so that, at some angle, the cross-correlation function may no longer be useful. To achieve a full strength correlation function, a possible option is to time-reverse one of the signals. We have noted that the correlation function has a τ scaling that depends on θ and that there is a specific value of θ for which the τ scale and the time scale are the same. We now examine the situation for time-reversed signals to see if a similar τ scaling in both space and time exists as a function of θ.

We return to the crossed-cell geometry of Fig. 1 but with the transducer of one of the cells placed at the opposite end. As a result, the two acoustic waves are both counterpropagating and time-reversed. To achieve correlation, the reference signal must be time delayed by an amount T_1, which, for example, might represent one or more frames of a signal that is periodic or changes in a known way from frame to frame. The product of the two waves leaving the crossed Bragg cells can be written as $f(t - T/2 - x/v)g[T_1 - (t - T/2 + x'/v)]$. The Fourier transform of this product, given that the cell containing $g(t)$ is at an angle θ with respect to the horizontal axis, is

$$A(p,q,t) = \iint_{P_1} f(t - T/2 - x/v) \times g(T_1 - t + T/2 - x'/v)\exp[j(px + qy)]dxdy. \quad (16)$$

We follow the same procedure as before using Eqs. (4) and (5) to obtain

$$B_1(p',q',t) = \frac{v}{\sin\theta}\exp[ja(t - T_1 - T)]\int g(u)\exp(jau)du, \quad (17)$$

$$B_2(p',q',t) = -v\exp[jb(t - t/2)]\int f(r)\exp(-jbr)dr, \quad (18)$$

where a and b have the same values as given in Eq. (8). We see that Eqs. (17) and (18) have the same form as Eqs. (7) and (8) except for slightly different exponential multipliers. By equating a and b and evaluating the function $A(p',q',t)$ along the line $p' = 0$, we get

$$A(\omega,t) = \frac{-v^2}{\sin\theta}\exp[j\omega(2t + T_1 - T/2)] \cdot \int g(u)\exp(-j\omega u)du \int f(r)\exp(j\omega r)dr \quad (19)$$

This result is similar to that given by Eq. (10). The exponential factor, however, is now a function of the present time t, the time delay T_1 of the signal $g(t)$, and the Bragg cell processing time T. This term considerably alters the nature of the temporal display of the correlation function $c(\tau)$ as we shall see later.

When the two acoustic waves are counterpropagating and time-reversed, the basic geometry is similar to that shown in Fig. 3 except that the transducer to which $g(t)$ is applied is on the opposite side of the Bragg cell. Many of the same results apply; for example, the weighting function which is based on geometric boundary considerations and given by Eq. (12) is still valid. The key difference is that the entire spatial correlation function now propagates along the τ axis, whereas it is stationary when the signals are not time-reversed.

The rate at which the correlation function moves relative to the time delay interval τ_d can be found by noting that, during a time interval T_0, the correlation function moves an amount given by $T_0/\sin\phi$. From Eq. (11) we find that, when the signals propagate one time resolution element, the correlation function propagates two time-delay resolution elements. Since this factor of 2 is independent of θ, it is always present when one signal is time-reversed.

It is, therefore, interesting that we could find an angle for which the spatial τ scale and the time scale are equal when one signal is not time-reversed but that such a condition does not exist for the temporal τ scale when one signal is time-reversed. In the first case, we used the crossed-cell geometry to display the τ values as a function of space. Since the correlation function does not move, independently of whether the signals are copropagating or counterpropagating, the angle between the Bragg cells can be used to change the spatial scaling. When one signal is time-reversed, the correlation function has similar spatial characteristics so that the Fourier transforms as given by Eq. (19) are the same as those given by Eq. (11) but only at a particular instant in time. At any other time, the Fourier transform is that of some asymmetric segment of $c(\tau)$. When the correlation peak occurs at the $\tau = 0$ spatial position at time $t = (T - 2T_1)/4$, the signals are said to be matched. In the communication theory literature the time-reversed counterpropagating mode of correlation is referred to as matched filtering because the presence of the reference signal in the received signal can, in principle, be found for any time delay. Furthermore, the processing operation is continuous, subject to some constraints on the ability to properly time-reverse the reference signal.

We would like to develop a technique wherein a true matched filtering operation can be performed without time-reversing the reference signal. Another desired feature would be to control the compression factor for the temporal scale of the correlation function. Finally, we would like to display the entire correlation function $c(\tau)$ in space, possibly with the same scale as the time-received signal. In the next section, we show how these features can be obtained.

IV. Differential Rate Correlation

Let us return to the geometric configuration given in Fig. 3. Suppose that we drive the reference code signal $f(t)$ at a higher rate than that of the received signal. We assume here that the reference signal is controlled by a clock whose rate can be varied. If $f(t)$ is an analog signal, similar results can be obtained by using a Bragg cells having different velocities of acoustic propagation. We let k be the ratio of the time base of the reference signal to that of the received signal.

We could analyze this case for an arbitrary angle θ as before, but the results are somewhat cumbersome. In general, the same results apply in a qualitative sense. One note of caution, however, is that θ must reach some minimum value, depending on the parameter k before correlation occurs at all. Two useful results from the detailed analysis will be given here. The first relates the angle ϕ of the line of integration to the rotation angle θ and the rate parameter k:

$$\phi = \arctan\left(\frac{1}{k\sin\theta} - \frac{1}{\tan\theta}\right); \qquad \arcsin\left(\frac{1-k^2}{1+k^2}\right) \le \theta \le 90°. \quad (20)$$

The second relationship is that the τ values are separated by

$$\tau_d = kT_0\cos(\phi - \theta)/\sin\theta. \quad (21)$$

The specific case that we will describe is that for $\theta = 90°$ and $k = \frac{1}{2}$ as shown in Fig. 6. The received signal $g(t)$ propagates downward with time resolution elements of duration T_0. The reference signal propagates to the right with elemental time resolution kT_0. From Eq. (20) we find that $\phi = 63.4°$ when $k = \frac{1}{2}$, and from Eq. (22) we find that $\tau_d = 0.45T_0$. The cross-product terms that contribute to the value of $c(\tau)$ at the origin of the τ axis are shown shaded, and the region of integration is a rectangle, which in turn produces a triangular weighting function identical to that shown in Fig. 4. The full range of possible τ values is displayed in space as before.

The major difference in the performance of the crossed-cell configuration using a different rate for the reference signal is that the correlation function now moves at a rate determined by k. During a time interval of T_0 sec, both signals move the same physical distance; this distance, however, represents one time sample for the received signal but $1/k$ samples for the reference signal. As a result, the correlation function will drift through the system, assuming that the reference code starts ahead of the received signal code, so that the correlation peak will eventually pass through the origin of the time-delay axis.

One other special case of some interest is that when $\theta = 45°$ and $k = \sqrt{2}/2$, we find that ϕ is also equal to 45° and that $\tau_d = T_0$. This set of conditions states that the spatial scaling of the τ axis is identical to that of the received signal so that further processing involving $c(\tau)$ and the time signals will not require a change in magnification.

We have developed, therefore, a useful technique whereby matched filtering can be achieved without a time-reversal of the reference signal. The correlation

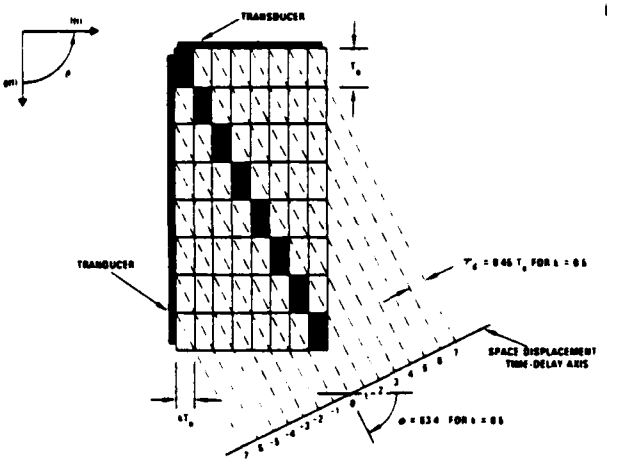

Fig. 6. Differential rate geometry.

function is still displayed in space so that all τ values are available, and, by changing k, we can vary the time compression factor to fill in the range between the two discrete values (0 or 2) that are produced by the other configurations. As k is changed, both ϕ and τ_d change so that an array of photodetectors may be required if we wish to operate at variable rates. We note that, for this processing configuration, the peak value of the correlation function is less sensitive to Doppler effects on the received signal since the system is much more forgiving of small changes in the signal time base.

V. Summary and Conclusions

The use of two Bragg cells crossed at an arbitrary angle θ serves to display the correlation function in space as well as in time. We showed that when the two waves propagate in the same direction only one relative time-delay value is available. As the angle between the cells increases, the number of time delays displayed in space increases because the spacing between adjacent delay values decreases. A particularly interesting condition arises when $\theta = 60°$, because the scaling factor for the τ axis is the same as that for the time axis. As a result, some triple-product operations can be achieved directly without the need to change the magnification.

The most often used configuration is that for which the two cells are orthogonally oriented ($\theta = 90°$). In this case, the maximum number of time-delay values are produced, and the correlation peak is still at full strength. The scale of the time-delay axis is now compressed by a factor of $\sqrt{2}$ relative to the time axis. When θ exceeds 90°, the two acoustic waves have a counterpropagating component, but the correlation function remains stationary. The number of cross products that contribute to the correlation peak begins to decrease, however, leading to a reduction in the performance of the system.

We investigated the crossed-cell geometry when the signals are time-reversed and counterpropagating. We found that the correlation function always propagates.

for any value of θ, with a compression factor of 2. Aside from being able to display a large range of τ values in space, there is little advantage to any geometry other than that of $\theta = 0$, for which the two signals propagate in opposite directions.

We developed a variation of the first geometry wherein the two signals propagate in the same direction without time-reversal but at different rates. It is now possible to display the correlation function in space, to cause it to move along the τ axis, and to control the relative rate of motion (the compression factor). In this most general case, then, we can achieve a compression factor ranging from zero, when the rates are the same, to any desired factor given by $(1 - k)/k$, where k is the ratio of the signal rates. When $k = \frac{1}{3}$, this optical processing architecture yields a compression factor of 2, which is the same as that for the counterpropagating time-reversed case but without the requirement that one signal be time-reversed.

Although the analysis given here was based on the use of Bragg cells as the signal input devices, the analysis is valid, with some modifications, for some other types of spatial light modulator as well. For example, a 2-D spatial light modulator, in which the same data are inserted in a column and the data flow through the system, behaves in a manner similar to that of a Bragg cell when its data are spread out in the direction orthogonal to the direction of propagation. A combination of two such modulators or one 2-D light modulator and a Bragg cell may be useful for achieving the most general geometries described in this paper.

This work was supported by the U.S. Army Research Office.

References

1. N. F. Izzo, "Optical Correlation Technique Using a Variable Reference Function," Proc. IEEE **53**, 1740 (1965).
2. E. B. Felstead, "A Simplified Coherent Optical Correlator," Appl. Opt., **7**, 105 (1968).
3. C. Atzeni and L. Pantani, "Optical Signal-Processing Through Dual-Channel Ultrasonic Light Modulators," Proc. IEEE **58**, 501 (1970).
4. W. T. Rhodes, "Acousto-Optic Signal Processing: Convolution and Correlation," Proc. IEEE **69**, 65 (1981).
5. R. A. K. Said and D. C. Cooper, "Crosspath Real-Time Optical Correlator and Ambiguity-Function Processor," Proc. IEE **120**, 423 (1973).
6. T. M. Turpin, "Time Integrating Optical Processors," Proc. Soc. Photo-Opt. Instrum. Eng. **154**, 196 (1978).
7. P. Kellman, "Time Integrating Optical Processors," Proc. Soc. Photo-Opt. Instrum. Eng. **185**, 130 (1979).
8. J. D. Cohen, "Ambiguity Processor Architectures Using One-Dimensional Acousto-Optic Transducers," Proc. Soc. Photo-Opt. Instrum. Eng. **180**, 134 (1979).
9. A. VanderLugt, "Adaptive Optical Processor," Appl. Opt. **21**, 4005 (1982).

APPENDIX B

STABILITY CONSIDERATIONS FOR ADAPTIVE OPTICAL FILTERING

REPRINTED FROM APPLIED OPTICS

VOLUME 25, PAGE 2314, JULY 15, 1986

Reprinted from Applied Optics, Vol. 25, Page 2314, July 15, 1986

Stability considerations for adaptive optical filtering

A. M. Bardos, W. R. Beaudet, and A. VanderLugt

We report analytical and experimental results from an interferometric optical system configured to implement a least mean square error filtering operation with an adaptive filtering loop. We describe the basic operation, experimental optical system, and simulation model; we then compare the results of the model and hardware. We find that the time delay must be minimized in the closed loop signal path to achieve good performance. Optical aberrations must also be controlled depending on the degree of phase margin required to maintain stability. We show that 30–35 dB of stable gain can be achieved with reasonable hardware and system tolerance requirements.

I. Introduction

In this paper we give the results of experiments conducted with an interferometric system which allows for adaptive processing of wideband signals. We designed, built, and tested an optical transversal filtering system with feedback, yielding a flexible architecture for various applications. The system can be configured, for example, to remove agile jammers in a wideband spread spectrum system performing an operation which requires a filter having many taps and a wide bandwidth. Other applications are channel equalization for wideband communication systems and the processing of signals from phased array radar systems for null steering or beam forming applications. These applications often require computational rates that cannot be met by current digital technology; even future developments such as VHSIC are likely to fall short of meeting the current and projected needs because communication and collection requirements continue to expand.

In adaptive filtering the system response function changes according to some measure of the characteristics of the received signal. In the application we chose to study, a wideband signal is corrupted by narrowband interference; the frequency, amplitude, and phase of the interferer are unknown. The task of the optical system is to measure these unknown parameters and to construct a notch filter to eliminate the unwanted signal. The desired wideband signal therefore has an improved SNR.

The authors are with Harris Corporation, Government Systems Sector, P.O. Box 37, Melbourne, Florida 32901.

Received 23 December 1985.
0003-6935/86/142314-12$02.00/0.

We begin with a brief review of adaptive filtering based on some earlier analyses. We simplify the development somewhat and view the basic operation from a different vantage point to set the stage for some new system modeling. In Sec. III we describe the hardware that we constructed in support of the experimentation and describe some new diagnostic techniques for aligning the system and monitoring its performance. The model development is given in Sec. IV in which we established criteria by which optimally stable systems can be designed. In Sec. V we give the major experimental results and show how they relate to the modeling results.

II. Background

In earlier analyses of adaptive filtering,[1,2] we described the basic operation of a frequency domain processor in terms of an analogy to a discrete transversal filter. Related work on adaptive filtering has been reported by Rhodes and Brown,[3] Rhodes,[4] and Psaltis and Hong.[5] The transversal filter includes a tapped delay line that contains the discrete time samples of the received signal. The output of each tap is weighted, as determined by the processing operation, and summed to provide an estimate of a signal. These operations are called linear predictor or estimator operations. If the estimated signal is subtracted from the received signal to provide a residual signal which controls the tap weights, the system is called an adaptive linear predictive system.

For this analogy, we note that Bragg cells accept wideband signals and behave as a continuous delay line that can be tapped optically. The basic adaptive operations can be described mathematically as a combination of convolution and correlation. The optimum weights are obtained by correlating the residual signal $z(t)$ with the received signal $s(t)$; the received signal is for this application assumed to consist of a wideband

signal $g(t)$ and a narrowband interference signal or jammer. The continuous tap weights $c(\tau)$ are then given by[1]

$$c(\tau) = G \int_{t-T_1}^{t} z(u)s(u-\tau)du, \tag{1}$$

where G is the gain in the feedback loop, T_1 is the integration time of the correlation loop, and τ is the continuous-time equivalent of the discrete delay time between samples of a digital system. The estimate is then given by convolution of the tap weights and the received signal:

$$\hat{s}(t) = \int_0^T c(\tau)s(t-\tau)d\tau, \tag{2}$$

where T is the total delay time of the Bragg cell. The estimate $\hat{s}(t)$ is subtracted from $s(t)$ to form the residual signal $z(t)$. At steady state, the strongly correlating jammer signal has been removed from the received signal, and the residual signal is the best approximation of the signal $g(t)$ in a least mean square error sense.

When we substitute Eq. (1) into Eq. (2), we obtain a time domain representation:

$$\hat{s}(t) = G \int_0^T \int_{t-T_1}^{t} z(u)s(u-\tau)s(t-\tau)dud\tau. \tag{3}$$

By means of the convolution theorem, we can also express $\hat{s}(t)$ as an integral in the frequency domain:

$$\hat{s}(t) = G \int_{-\infty}^{\infty} Z_T(\omega,t)\,|S_T(\omega,t)|^2 \exp(j\omega t)d\omega, \tag{4}$$

where Z_T and S_T are the instantaneous Fourier transforms of those portions of $z(t)$ and $s(t)$ within the Bragg cells of duration T. We can easily see from the frequency domain representation how the estimate is developed. The $|S_T(\omega,t)|^2$ factor puts a strong weight on the spectrum at those dominant spectral terms that represent the jammer. In effect, the instantaneous power spectrum of $s(t)$ is used as a template to separate the jammer from the signal so that it can be used in the feedback loop.

Figure 1 shows only the key elements of the interferometric optical system and suggests how we plan to model its system response in a feedback loop. We represent all three Bragg cells with idealized transducer heights that render the region of interaction between light and acoustic waves into a square format. The idealization shown generates the same results as obtained by using Bragg cells with suitable anamorphic optical systems described in Sec. III. The Bragg cells, with respect to an observation plane external to the interferometer, appear to overlap as shown in Fig. 2(a). We refer to this plane as the tap weight plane. The transducer of the Bragg cell that is disposed at 45° to the first two must lie on the bisector established by the other two transducers.

We have two ways in which the Bragg cells can be driven. If we drive the two orthogonal Bragg cells with $s(t)$ and $z(t)$, all the cross-product terms required to establish $c(\tau)$ as given by Eq. (1) are formed at the tap weight plane. In principle, we must integrate the light along lines parallel to the bisector to obtain $c(\tau)$.[6] For the moment, if suffices to visualize that the action of

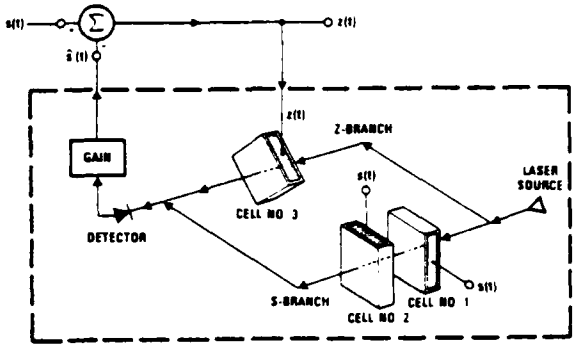

Fig. 1. Simplified system schematic.

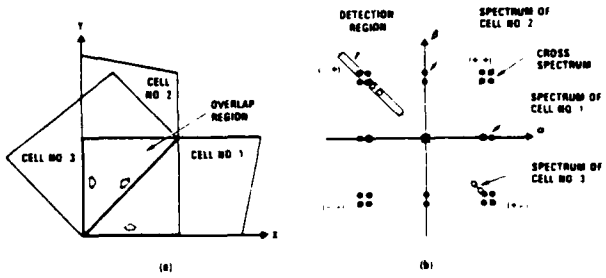

Fig. 2. Signal geometry: (a) tap weight plane; (b) spectral plane.

the third Bragg cell is to convolve $s(t)$ with the stationary 2-D cross products in the overlap region illustrated in Fig. 2(a) to provide the estimate $\hat{s}(t)$ as given by Eq. (2). The required integration is effectively performed by the photodetector because it detects light only in the overlapping region.

The second way to drive the cells is to drive both orthogonal cells with $s(t)$ as we show in Fig. 1. This connection tends to emphasize the frequency domain representation as given by Eq. (4); in this case we focus our attention on the Fourier plane where the photodetector is located. The orthogonal Bragg cells of the S-branch produce $|S_T(\omega,t)|^2$, which selects the strong periodic signals from $Z_T(\omega,t)$, produced by the Z-branch, for use as feedback signals.

Figure 2(b) shows the equivalence of these two connection schemes. Suppose that $s(t)$ consists of two cw signals which appear at both positive and negative frequencies along the two spatial frequency axes; we assume Raman-Nath operation for the sake of this illustration. The signals interact to also provide a set of four spectral components in each frequency quadrant; these components are shown as filled circles. The upper right quadrant is marked (++) to indicate that both cells 1 and 2 produce a frequency upshift. In our model the upper left quadrant is used; in this quadrant the frequencies have a downshift/upshift structure. The region in the upper left quadrant occupied by the photodetector covers the domain of overlapping frequencies.

Suppose that the third cell is driven by $z(t)$, which also consists of two frequencies shown as open circles;

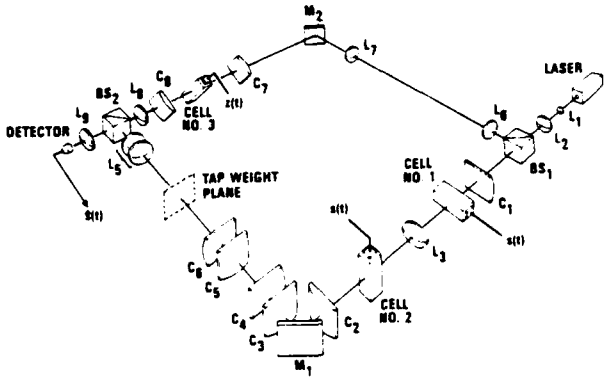

Fig. 3. Optical subsystem layout.

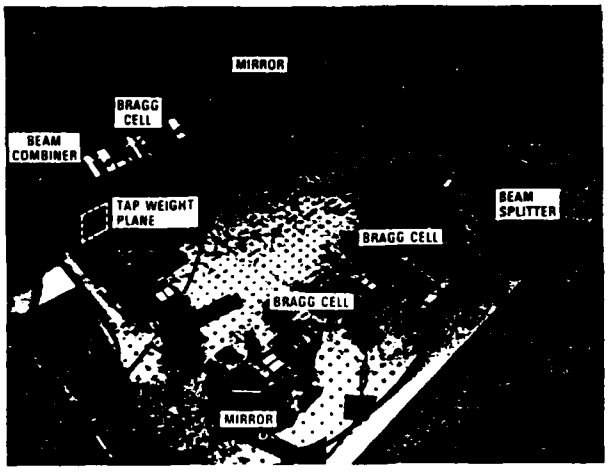

Fig. 4. Experimental hardware.

these signals are shown with a slightly lower frequency so that we can visualize some important relationships. It is easy to see that these frequency components overlap on the diagonal provided that the frequencies of $z(t)$ equal those of $s(t)$ and that the optical system magnifies the spectrum of cell 3 by $\sqrt{2}$. We cannot then distinguish the two alternative Bragg cell drive configurations, and we are free to select the signal connection scheme that optimizes system performance. For the purpose of model development, we prefer the connection scheme shown in Fig. 1. We now describe the experimental hardware and discuss some preliminary results that set the stage for discussion of the enhanced model.

III. Hardware

Figure 3 is a schematic of the optical system as implemented, and Fig. 4 shows the associated hardware. The basic configuration is that of a Mach-Zehnder interferometer. Other interferometer architectures, such as a more nearly common path interferometer,[7] may be less sensitive to vibrations, thermal gradients, air currents, or acoustic coupling. As a preliminary experimental system, however, the Mach-Zehnder configuration is convenient to use and easy to modify as needed. The light source is a 15-mW He–Ne laser, whose output beam is expanded by lenses L_1 and L_2 and divided into two beams by beam splitter BS_1. Cylindrical lens C_1 focuses the light into a horizontal line to illuminate efficiently the first Bragg cell driven by $s(t)$. The Bragg cells are constructed from TeO_2 material which is oriented to operate in the slow shear mode. The bandwidth of each cell is 50 MHz, centered at 90 MHz, and the cell fill time is 40 μs. A quarterwave plate, not shown in Fig. 3, produces circularly polarized light at the entrance to the Bragg cell to improve diffraction efficiency and spectral band uniformity.

Lens L_3 produces a 2-D Fourier transform of the first cell at the entrance to the second Bragg cell. This cell is similar to the first, except that its tranducer is made larger to accommodate the Fourier transform from the first Bragg cell. Lens L_3 collimates the light in the vertical direction to illuminate the second cell at the Bragg angle. This second cell may be driven by $s(t)$ or $z(t)$, yielding equivalent results.

Cylindrical lenses C_2 through C_6 serve to mutually image the two Bragg cells into a square format at the tap weight plane. It is not necessary that this plane be displayed explicitly; doing so, however, provides a convenient reference plane that can be used for diagnostic purposes. For example, if both Bragg cells are driven by a square wave test signal, a triangular shaped periodic autocorrelation function appears at the tap weight plane. If the test signal is a pseudorandom sequence, the autocorrelation peak defines the $\tau = 0$ line; this information is useful for properly positioning the third Bragg cell. It is also convenient to reference all amplitude weighting functions and phase aberrations to this plane. We note in passing that the autocorrelation functions are oriented at 45° to the transducer faces of the cells.

The hardware causes the correlation, as described by Eq. (1), to take place through a multiplication of the Fourier transforms of two signals, as described by Eq. (4). Lens L_5 serves to create the Fourier transform of the tap weight plane at the spectral plane just beyond beam combiner BS_2. A relay lens L_9, operating at a demagnification of two, images the spectral plane onto a single-element high-speed photodetector. In the second branch of the interferometer, a telescope consisting of lenses L_6 and L_7 and a cylindrical lens C_7 shape the Bragg cell illuminating beam. This cell is disposed at 45° relative to the other two so that the signal travels in a direction parallel to that of the correlation function established at the tap weight plane in the first branch. Lenses C_8 and L_8 create the Fourier transform just beyond the beam combiner at the spectral plane where the two Fourier transforms are joined to make heterodyne detection possible.

One Bragg cell in the S-branch is operated in the downshift mode, while the second one is operated in the upshift mode; as a result, there is no net frequency shift of the light in this branch. The cell in the Z-

branch is operated in the upshift mode so that the heterodyne action is centered at 90 MHz. It is relatively easy, therefore, to subtract the estimated signal from the received signal at rf; there is no need to demodulate the signal to baseband.

Figure 4 shows the hardware as implemented. Most of the components and their positions can be readily identified by comparing Fig. 4 with Fig. 3. We identify the tap weight plane in the S-branch by dotted lines. The Bragg cell assembly in the Z-branch, consisting of C_7, the Bragg cell, C_8, and L_8, is mounted so that the assembly can be adjusted in angle and position relative to the components in the S-branch. The effective focal length of the pair of lenses, denoted L_5 in Fig. 3, can be adjusted to equalize the scale of the transforms. We use prisms after each Bragg cell to bring the diffracted beam to the original axis, thereby keeping the system collinear.

The electronic part of the system consists of rf drivers for the Bragg cells, a specially designed preprocessing and postprocessing electronic system, and various test electronics such as signal sources, oscilloscopes, rf network analyzers, and spectrum analyzers. The signal source module provides a 90-MHz carrier that can be modulated in either a BPSK or QPSK format by an external signal source such as a pseudorandom sequence generator. This wideband signal is combined with one or more jammers from another external source to represent the received signal.

The photodetector subsystem detects the light and amplifies the signal through several stages of amplification; the output signal is then brought to the signal processing electronics where it is subtracted from the received signal to yield the residual signal. This signal is fed to the third Bragg cell to close the loop. The residual signal can also be fed to a demodulation module which then recovers the pseudorandom sequence and provides a means for making SNR measurements at the output. The signal processing electronics also include the necessary rf level adjusting pads, bandpass filters, mixers, and amplifiers.

We developed several open loop diagnostic procedures for the precision alignment needed to obtain proper system performance. Initial alignment to obtain a heterodyne signal output requires that the two branches of the interferometer be coincident and collinear. To equalize the scale of the Fourier transforms in the two branches, we drive all Bragg cells with two frequencies. The Fourier plane contains two spots of light from each branch; we adjust the spacing of lens combination L_5 to achieve overlap, thus equalizing the scale. The single Bragg cell branch has a rotational provision so that we can match the angle of the separate Fourier transforms. Finer adjustments are then obtained by maximizing the photodetector current as the parameters are varied. At some point in the adjustment, further increases in the output signal could not be made, and we attempted closed loop operation.

We found the system to be stable over only a small frequency range even though the alignment seemed adequate. The problem is that maximizing the amplitude of the output is not a sufficiently sensitive measure of the phase response of the system. We therefore developed a technique in which we used an rf network analyzer to help improve system alignment. We repeated the tests with the cw signal using the open loop mode. As a single frequency is swept over the passband, the network analyzer displays the amplitude and phase of the resultant heterodyned light output. Figure 5(a) shows the amplitude and phase response as displayed by the network analyzer at the initial state of alignment. The linear phase is shown by the sawtooth waveform; one vertical division represents 90° of phase, and the horizontal scale is 100 kHz/division. As we see, the phase changes by 360° at ~100-kHz intervals for this stage of alignment.

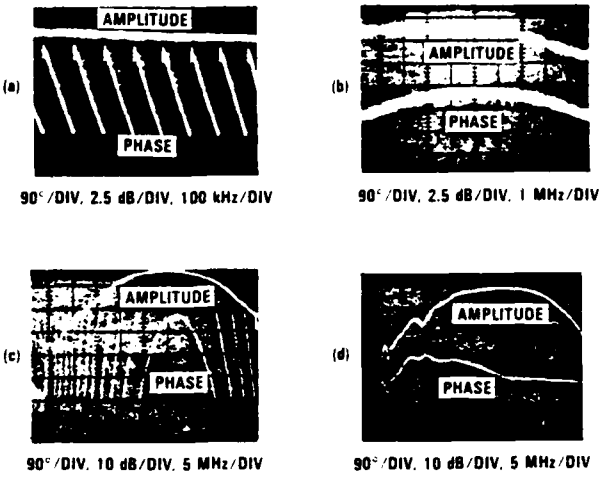

Fig. 5. Network analyzer traces for system alignment: (a) initial amplitude and phase; (b) response with linear error removed; (c) full bandwidth view with residual quadratic phase errors; (d) response after alignment.

The principal cause of the linear phase across the spectral band is the time delay differences between the two branches caused by the relative displacement of the three Bragg cells along the acoustic propagation direction. By adjusting the positions of the Bragg cells, we removed the linear component of the phase change to the degree shown in Fig. 5(b). Here we see that the phase is nearly flat over ~10 MHz of the passband. A slightly curved residual phase change is now evident; this is indicative of a difference in the wave-front curvatures from the two branches of the system.

The curvature is a second-order effect that is not easy to detect until the linear phase has been nearly compensated; it represents several wavelengths of departure from the ideal telecentric Fourier transform and has no impact on the light intensities in the system. The phase curvature is more readily observed in Fig. 5(c) where we extend the bandwidth to display the response in the passband from 70 to 110 MHz. The phase varies slowly near 90 MHz and then with increasing rapidity near the band edges as is characteris-

tic of a quadratic function. Figure 5(d) shows the next stage of correction where most of the quadratic phase curvature has been removed by moving the Bragg cell of the Z-branch along the optical path. After this adjustment, there is still a 90° phase shift over the bandpass and a significant change in the amplitude response. We found the amplitude response to be a strong function of the interaction between the Bragg angle and polarization of the illumination. Although we could have adjusted the Bragg angle to make the response more uniform, we decided to optimize the response at midband to get the highest possible SNR. At this stage of system alignment we obtained ~12 dB of jammer suppression; to obtain more suppression we needed to analyze further the basic causes of system instability and find ways to modify further the hardware based on the analytical results.

IV. Model Development

The experimental results clearly indicated the need for an enhanced model that describes the hardware more precisely, especially phase effects unique to the coherent optical implementation. A half-wavelength change in the length of one branch of the interferometer, for example, will change the sign of the detected signal, thus converting the loop from a negative to a positive feedback system and creating a runaway condition. We have found that it is the phase of the open loop response that is the most useful predictor of system stability.

We developed a linear model that describes the optical system in terms of real-valued transfer function G, referred to as the grand system kernel. The electrical system model represents the optical system as a time-dependent (adaptive) frequency response in a feedback system which subtracts the signal estimate $\hat{s}(t)$ from the signal input $s(t)$, generating the error function $z(t)$ as shown in Fig. 6(a). To make a linear model possible, we treat the inputs to the three Bragg cells as independent functions even though the same signal might be driving two of those cells.

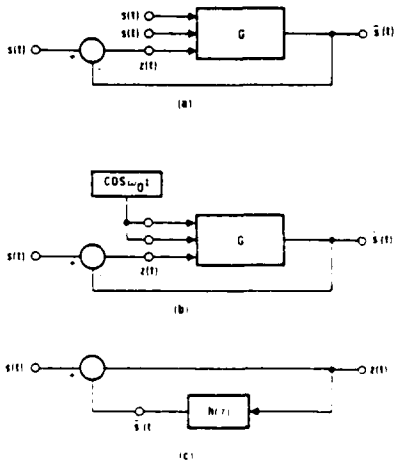

Fig. 6. System response models: (a) full model; (b) pure jammer model; (c) impulse response model.

The signal estimate $\hat{s}(t)$, the output of the detection subsystem (detector, filter, amplifier, etc.), can be expressed as a function of the signal input $s(t)$ which drives the two orthogonal cells, the residual function $z(t)$ which drives the third cell, and the transfer function G:

$$\hat{s}(t) = \iiint_{-\infty}^{\infty} s(t')s(t'')z(t''')G(t',t'',t''',t)dt'dt''dt'''. \quad (5)$$

The system kernel function G describes all the physical properties of the optical system, that is, all the phase and amplitude effects as well as the convolution and correlation nature of the architecture. Even causality is embedded in the kernel; instead of using finite limits of integration, we require that G vanish for noncausal combinations of the four arguments to prevent the future from influencing the present. The kernel function G is the transfer function of the optical subsystem shown enclosed by dashed lines in Fig. 1.

The advantage of the linear transfer function formulation, in spite of its apparent complexity, is that the transfer functions of the various subsystems can be chained, or cascaded, to yield a linear transfer function for the overall system. Let us first consider a Bragg cell whose inputs are the amplitude $a(x,y,t)$ of the illuminating beam and the rf drive signal $r(t)$; its output $a_1(x,y,t)$ is the amplitude of the diffracted light. In its most general form, the linear transfer function model would permit all combinations of spatial and temporal values of the two input functions to contribute to all values of the output function. To express the output light amplitude as a function of three variables, we would need to use a kernel function of seven variables and fourfold integration over the four space–time input variables. The integrals over three variables can be completed, however, by using a simplified model, in which the Bragg cell is treated as a planar time-varying phase mask, so that the illumination wave-front and the output light amplitude interact only at a single space-time point. Therefore, we seek a Bragg cell transfer function P of the following form:

$$a_1(x,y,t) = \int_{-\infty}^{\infty} a(x,y,t)r(t')P(t',t,x,y)dt'. \quad (6)$$

This formalism has sufficient power to express the relevant performance characteristics of a Bragg cell which performs five key functions: (1) it bandlimits the electrical signal; (2) it generates a propagating acoustic wave; (3) it performs a spatial aperture weighting operation due to acoustic attenuation and the finite length of the cell; (4) it converts acoustic pressure waves into multiplicative perturbations of the input optical wave, thus generating the diffracted output light; and (5) it selects either the negative or positive spatial frequencies depending on the illumination geometry.

We shall combine the effects of temporal band limitation and Bragg selectivity into a single composite transfer function that converts the input rf drive func-

tion into an effective complex drive signal containing only positive temporal frequencies for an upshift configuration or negative ones for a downshift geometry. This band limitation can be expressed as a multiplication by the frequency response in the frequency domain or as a convolution with the impulse response in the time domain. The effective complex drive signal $r'(t)$ thus becomes

$$\begin{aligned} r'(t) &= F^{-1}[B(f)F[r(t)]] \\ &= \int\int_{-\infty}^{\infty} B(f)r(t')\exp[j2\pi f(t-t')]df dt' \\ &= \int_{-\infty}^{\infty} r(t')b(t-t')dt', \end{aligned} \tag{7}$$

where $B(f)$ is the composite frequency response, $b(t)$ is the corresponding complex impulse response given by

$$b(t) = \int_{-\infty}^{\infty} B(f)\exp(j2\pi ft)df. \tag{8}$$

For an upshift Bragg cell geometry with bandwidth δf, centered at f_c, and uniform frequency response, we have

$$\begin{aligned} B^+(f) &= \text{rect}[(f-f_c)/\delta f], \\ b^+(t) &= F^{-1}|B(f)| = \delta f \exp(j2\pi f_c t)\,\text{sinc}(\delta f t). \end{aligned} \tag{9}$$

For a downshift configuration we need only to use a negative carrier frequency in these equations to obtain $B^-(f)$ or $b^-(t)$.

The propagation of the signal in the x direction with acoustic velocity v and temporal offset t_0 can be described by replacing the time variable t with $t - x/v - t_0$. However, in keeping with the cascaded linear model, we perform this operation using the sifting property of the delta function. The effective signal $r''(x,t)$ traveling in the Bragg cell can be expressed in terms of the bandlimited signal $r'(t)$, and, by using Eq. (7), we can show its relationship to the drive signal $r(t)$:

$$\begin{aligned} r''(x,t) &= \int_{-\infty}^{\infty} r'(t'')\delta[t'' - (t - x/v - t_0)]dt'' \\ &= \int_{-\infty}^{\infty} r(t')b(t - x/v - t_0 - t')dt'. \end{aligned} \tag{10}$$

We shall model the conversion of the traveling acoustic pressure waves into light amplitude by assuming that the input light is retarded by the index waves as expressed by an exponential multiplier $\exp[j\epsilon r''(x,t)]$. If the argument is small, this multiplier is approximated by $1 + j\epsilon r''(x,t)$. We drop the unity term which represents the undiffracted light normally blocked in the optical system. We define the amplitude weighting aperture function as $w(x,y)$; the output light amplitude is therefore given as

$$a_1(x,y,t) = j\epsilon w(x,y)r''(x,t)a(x,y,t) \tag{11}$$

We combine Eqs. (10) and (11) to obtain the complete Bragg cell transfer function P postulated in Eq. (6):

$$P(t',t,x,y) + j\epsilon w(x,y)b(t - x/v - t_0 - t'). \tag{12}$$

By cascading Eq. (11) through two crossed Bragg cells, we have

$$a_{12}(x,y,t) = -\epsilon^2 w_1(x,y)w_2(x,y)r_1^*(x,t)r_2^*(y,t)a(x,y,t). \tag{13a}$$

By using Eq. (10), we obtain an expression in terms of the two drive signals $r_1(t)$ and $r_2(t)$ using the linear transfer function formalism for this subsystem:

$$a_{12}(x,y,t) = \int\int_{-\infty}^{\infty} k_{12}(x,y,t,t',t'')r_1(t')r_2(t'')dt'dt'', \tag{13b}$$

where

$$\begin{aligned} k_{12}(x,y,t,t',t'') &= -\epsilon^2 w_1(x,y)w_2(x,y)b^-(t - x/v - t_1 - t') \\ &\quad \times b^+(t - y/v - t_2 - t'')a(x,y,t). \end{aligned} \tag{13c}$$

In the Z-branch of the interferometer we have a single Bragg cell that is rotated 45° with respect to those in the S-branch and is scaled optically so that its spectrum matches the scale of the cross-spectral terms of the S-branch. The propagation is along the diagonal of the second quadrant with an effective acoustic velocity of $v/\sqrt{2}$ to properly stretch the spectrum; the distance from the transducer of an arbitrary point with coordinates x,y is $(y - x)/\sqrt{2}$. The acoustic propagation time, the ratio of distance and effective velocity, is therefore $(y - x)/v$ for this Bragg cell. The optical output of cell 3, referenced to the tap weight plane, can be written as

$$a_3(x,y,t) = j\epsilon w_3(x,y)r_3^*(x,y,t)a'(x,y,t), \tag{14a}$$

or, in kernel form, as

$$a_3(x,y,t) = \int_{-\infty}^{\infty} k_3(x,y,t,t''')r_3(t''')dt''', \tag{14b}$$

where

$$\begin{aligned} k_3(x,y,t,t''') &= j\epsilon w_3(x,y) \\ &\quad \times b^+(t - y/v + x/v - t_3 - t''')a'(x,y,t). \end{aligned} \tag{14c}$$

The light amplitudes a_{12} and a_3 of the respective tap weight planes are Fourier transformed in the variables x and y to obtain the spectral plane amplitudes A_{12} and A_3 as functions of the spatial radian frequencies α and β. We need only to Fourier transform the kernels in Eqs. (13b) and (14b) because the time-dependent terms are unaffected by the spatial transforms. The spectral plane amplitudes are

$$A_{12}(\alpha,\beta,t) = \int\int_{-\infty}^{\infty} K_{12}(\alpha,\beta,t,t',t'')r_1(t')r_2(t'')dt'dt'', \tag{15a}$$

where

$$\begin{aligned} K_{12}(\alpha,\beta,t,t',t'') &= \int\int_{-\infty}^{\infty} k_{12}(x,y,t,t',t'') \\ &\quad \times \exp[j(\alpha x + \beta y)]dxdy, \end{aligned}$$

and

$$A_3(\alpha,\beta,t) = \int_{-\infty}^{\infty} K_3(\alpha,\beta,t,t',t''')r_3(t''')dt''', \tag{15b}$$

where

$$K_3(\alpha,\beta,t,t''') = \iint_{-\infty}^{\infty} k_3(x,y,t,t''') \times \exp[j(\alpha x + \beta y)]dxdy.$$

The two branches are combined by a beam splitter so that the light intensity at the spectral plane is

$$I(\alpha,\beta,t) = |A_{12}|^2 + |A_3|^2 + 2\,\mathrm{Re}|A_{12}A_3^*|.$$

The first two terms are baseband signals whose possible effects in generating spurious in-band frequency terms we ignore in this analysis. The cross term provides the in-band signal term that is integrated by the detector whose aperture function is $D(\alpha,\beta)$. The signal estimate generated by the detector is

$$\hat{s}(t) = \iint_{-\infty}^{\infty} D(\alpha,\beta)2\,\mathrm{Re}|A_{12}(\alpha,\beta,t)A_3^*(\alpha,\beta,t)|d\alpha d\beta. \quad (16)$$

By using Eq. (15) and collecting terms, we obtain the grand system kernel formulation of Eq. (5) with

$$G(t',t'',t''',t) = \iint_{-\infty}^{\infty} D(\alpha,\beta)2\,\mathrm{Re}|K_{12}(\alpha,\beta,t,t',t'') \times K_3^*(\alpha,\beta,t,t''')|d\alpha d\beta. \quad (17)$$

The detector collection aperture needs to be small enough to reject spurious terms yet large enough to gather the desired signal located around the diagonal of the second quadrant. While the illustration in Fig. 2(b) shows all the spectral terms that acoustic cells operating in the Raman-Nath regime would generate, our model of the Bragg selective devices has already rejected most of the undesirable terms. Only the off-diagonal cross-spectral terms of the S-branch survive. It is important to observe that these terms do not contribute to the signal estimate if they are sufficiently far off-axis, since the spectrum due to the Z-branch, and hence the product terms in Eq. (16), are zero at those locations. We conclude, therefore, that an open detector aperture, i.e. integration over the complete spectral plane, leads to a good representation for most cases.

This model does not preclude, however, performance differences between this open detector configuration and one with a narrow slit on the diagonal. For the case of two jammers, for example, the off-diagonal terms may begin to beat with the diagonal spectral terms as the two jammer frequencies come within few resolution elements of one another. Additional differences may exist in the analysis of transient phenomena which cause momentary spreading of the spectral spots. We further conjecture that similar subtle differences can be observed between the performance of the two alternative signal connection schemes.

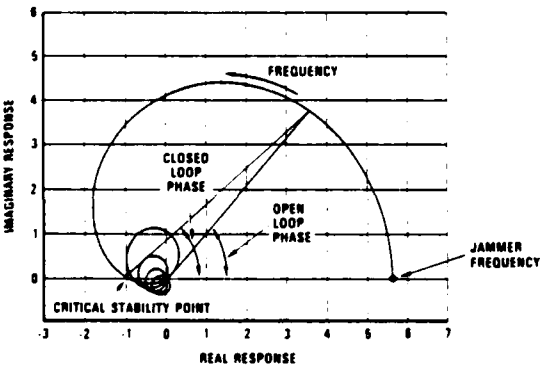

Fig. 7. Complex frequency response.

We obtain the system kernel function and the signal estimate for the open detector case by substituting $D(\alpha,\beta) = 1$ into (17), and we express it in terms of the tap weight plane variables by using Eq. (15):

$$G(t',t'',t''',t) = \mathrm{Re}\left\{\iint_{-\infty}^{\infty} k_{12}(x,y,t,t',t'') \times k_3^*(x,y,t,t''')dxdy\right\}. \quad (18)$$

$$\hat{s}(t) = 2\,\mathrm{Re}\left\{\iint_{-\infty}^{\infty} a_{12}(x,y,t)a_3^*(x,y,t)dxdy\right\}.$$

For the open detector case, therefore, detection could have been performed in the tap weight plane without performance differences. For this case, then, we see the significance of the triangular overlap region of Fig. 2(a), since the integral of Eq. (18) has nonzero terms only in that domain. As one would expect, the kernel is time stationary in the sense that it depends on time only through the differences $t - t'$, $t - t''$, and $t - t'''$. We shall now examine a very important special case where the time dependence can be reduced to a single variable $\tau = t - t'''$, simplifying the system kernel model to a convolution with an impulse response.

A. Impulse Response Model

Let us examine the case of a pure jammer input to the system without a wideband signal term present, as shown in Fig. 6(b). For a sinusoidal input of frequency f_0 in the two orthogonal cells, the effective drive defined in Eq. (7) becomes a complex exponential. By using Eq. (10), we write the effective signal traveling in the x direction in the downshifted first cell and in the y direction in the upshifted second cell in the following form:

$$r_1^*(x,y,t) = \exp[-j2\pi f_0(t - x/v - t_1)];$$
$$r_2^*(x,y,t) = \exp[j2\pi f_0(t - y/v - t_2)]. \quad (19)$$

If we use plane wave illumination in both branches, with a phase difference of ϕ, define a joint window function $w(x,y)$, and collect all phase terms into θ, we have

$$a(x,y,t) = \exp(j\omega_0 t),$$
$$a'(x,y,t) = \exp(j\omega_0 t - j\phi),$$
$$w(x,y) = e^3 w_1(x,y)w_2(x,y)w_3^*(x,y), \quad (20)$$
$$\theta = \phi + 2\pi f_0(t_1 - t_2) - \pi/2.$$

Substitution of Eqs. (13a), (14a), and (20) into Eq. (18) yields

$$\hat{s}(t) = 2\,\mathrm{Re}\left\{\iint_{-\infty}^{\infty} w(x,y)\exp(j\theta) \times \exp[-j2\pi f_0(y-x)/v]r_3^*(x,y,t)\,dx\,dy\right\}. \quad (21)$$

Let the input to the third cell be $z(t)$ so that the effective signal propagating along the $y-x$ direction is

$$r_3(x,y,t) = \int_{-\infty}^{\infty} z(t')b(t - y/v + x/v - t_3 - t')\,dt'. \quad (22)$$

The detected signal given by Eq. (16) can be formulated as a convolution:

$$\hat{s}(t) = \int_{-\infty}^{\infty} z(t')h(t-t')\,dt',$$

$$h(\tau) = \iint_{-\infty}^{\infty} 2\,\mathrm{Re}[w(x,y)\exp[j2\pi(y-x)f_0/v + j\theta] \times b^*(\tau - y/v + x/v - t_3)]\,dx\,dy. \quad (23)$$

The complete optical system and the two input signals r_1 and r_2 are combined into this real-valued impulse response $h(\tau)$. This unique case, in spite of its simplicity, yields powerful analytical and experimental results that helped to control instabilities. The exponential term shows that the phase shifts by 180° for a halfwave change in the optical path difference between the two interferometer branches; time varying phase changes must, therefore, be well controlled to preserve the phase of the feedback signal. The window function $w(x,y)$ must also have constant phase. Otherwise contributions from various locations will cancel on integration; optical aberrations, therefore, need to be controlled in both interferometer branches.

B. Stability Criteria

Let us consider a negative feedback system having a filter in the return path with impulse response $h(\tau)$, as shown in Fig. 6(c). The condition for stability can be stated in terms of the Laplace transform $L(s)$ of the impulse response of the feedback path. We require that all zeros of $1 + L(s)$ be in the left half-plane of s. For the feedback system analyzed, we may paraphrase the stability condition: the poles of the system transfer function $1/[1 + L(s)]$ must all fall in the left half-plane.

Our attempts to use the root method as a diagnostic and predictive tool ran into practical difficulties; our computer program, capable of finding the complex roots of real polynomials, often reported numerical overflow with sixty-fourth-order polynomials. To overcome these limitations, we seek alternative formulations for the stability condition.

We express stability in terms of the complex frequency response of the feedback path: the transform $H(\omega)$ must not circle -1, the critical stability point in the complex plane. A sufficient condition of stability may be stated as requiring that the Fourier transform of the impulse response must not have any negative real values left of the -1 point on the real axis, i.e., the system should have less than unity gain at any frequency with a 180° phase shift.

We found the Fourier transform techniques easy to use both experimentally and analytically; fast Fourier algorithms and network analyzers provide the necessary tools. Figure 7 illustrates a frequency response that is stable because it does not circle the -1 point of the complex plane. The system response has a positive real value at the jammer frequency; as the frequency increases, the response becomes complex valued and its magnitude decreases. The phase of the open loop frequency response $H(\omega)$ along with that of the closed loop response $1/[1 + H(\omega)]$ are shown for a particular frequency. As the open loop phase angle reaches π, $H(\omega)$ crosses the negative real axis. Since the negative crossings cannot go past the -1 point, the maximum achievable gain can be determined from the ratio of the maximum and minimum values on the real axis.

C. Optimization Criteria

While exercising the model, we generally sought conditions for which we can obtain the deepest jammer suppression notch. To determine the closed loop stability of the single-jammer situation using the Fourier transform criterion, we write the open loop impulse response $h(t)$ in the following form:

$$h(t) = \begin{cases} w(t)\cos(\omega_0\tau), & \beta T \le \tau \le T; \\ 0, & \text{elsewhere.} \end{cases} \quad (24)$$

Here ω_0 represents the jammer frequency we desire to suppress, βT is a delay generated by hardware limitations, T is the Bragg cell fill time, and $w(t)$ is a window function describing the amplitude profile of the impulse response produced by the geometry and illumination of the optical system. The closed loop frequency response $F(\omega)$ can be expressed as

$$F(\omega) = 1/[1 + H(\omega)]. \quad (25)$$

The stability criterion, expressed in terms of $F(\omega)$, is that the closed loop frequency response phase never reaches 180° regardless of gain.

We generated computer optimized window functions over various blocking ratio values β, which expresses the inaccessible fraction of the aperture time T. We use the stability criterion that the open loop frequency response $H(\omega)$ must have less than unity gain at any frequency where its phase equals 180°. Slowly varying functions (Gaussian, linear, cosine) and their sums were used to shape the impulse response. Figures 8(a) and (b) show the results of this optimization for a delay equal to 1.5% of the length of the impulse response ($\beta = 0.015$). From Fig. 8(b), we note that a stable gain of 45 dB is theoretically predicted for the window function shown in Fig. 8(a). This stable gain is obtained by measuring the amplitude at the π crossings relative to the peak amplitude. However, even the slightest phase error in the system will suddenly create instabilities at the point where the phase nearly reaches 180° inside the central lobe, limiting its stable performance to only 28 dB of suppression. This optimization criterion, therefore, leads to systems that are intolerant of small phase errors.

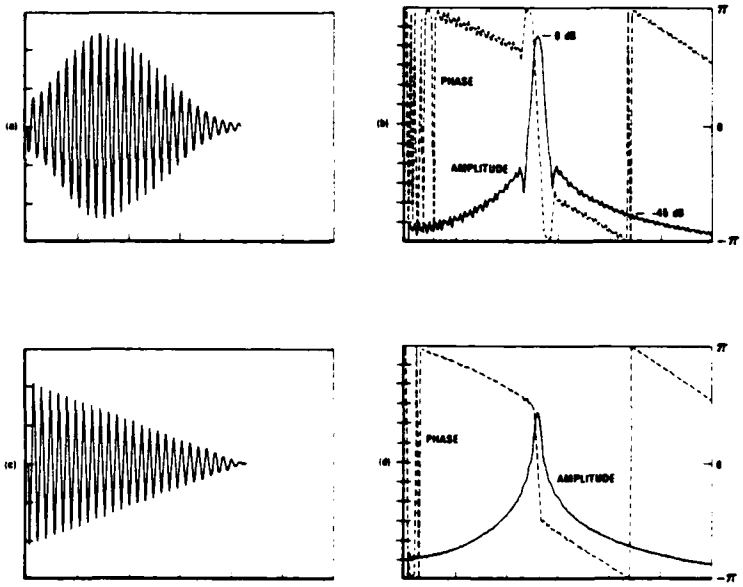

Fig. 8. Optimized system responses: (a) Gaussian impulse response; (b) frequency response for Gaussian model (5 dB/div); (c) linearly apodized impulse response; (d) frequency response of linear model (5 dB/div).

We therefore recast the question into the following form: "What is the maximum suppression that can be achieved for a given irreducible time delay with a given system phase error margin, and what is the optimum impulse response shape?" We first defined a more stringent stability criterion that requires that the phase of the closed loop frequency response remain between −90 and 90°. Stated in terms of the open loop frequency response, we require that the real part of $H(\omega)$ be greater than −1 at all values of ω. We refer to this condition as the strong stability criterion; it ensures a softer, more nearly monotonic frequency response, which in turn guarantees a more gradual performance degradation as phase errors are introduced. Whereas the frequency response shown in Fig. 7 is stable, it does not meet the strong stability criterion because the locus of $H(\omega)$ crosses into the region left of the line where the real part of the response is equal to −1. In that region, the closed loop phase exceeds 90°, thereby violating our strong stability criterion.

For a blocking ratio of $\beta = 0.015$, we can achieve a strongly stable suppression of 32 dB with the optimum impulse function as shown in Fig. 8(c). From Fig. 8(d) we see that the phase response approaches 180° much more gently than in Fig. 8(b), and therefore it offers a more graceful degradation of performance with the introduction of phase errors. This concept of strong stability and the demonstrated experimental results can be used to design a rugged realizable system that has maximal tolerance to phase errors induced by environmental conditions such as vibration and temperature changes.

Computer optimizations based on the strong stability criterion yield an interesting result: the optimum window function is a linear taper from the initial maximum to zero at $t = T + \beta T$. Coincidentally, the triangular geometry of the tap weight plane would generate just such a sawtooth weighting for uniform optical illumination, as suggested by the shaded region shown in Fig. 2. Let us analyze the stability of a linearly tapered impulse response at baseband. We introduce the parameter B to define the impulse response and note the relationship that $\beta = (1 - B)/(1 + B)$. We then have

$$h(\tau) = \begin{cases} (2 - \tau)/2B, & (1 - B) < \tau < (1 + B); \\ 0, & \text{elsewhere.} \end{cases} \tag{26}$$

The real part of the frequency response is

$$G(p) = \mathrm{Re}[H(p)] = \mathrm{Re}\left\{\int_{-\infty}^{\infty} h(\tau) \exp(jp\tau) d\tau\right\}. \tag{27}$$

By using the coordinate transformation $x = \tau - 1$, we obtain

$$G(p) = \frac{1}{2B}\int_{-B}^{B} (1 - x)\cos[(1 + x)p]dx.$$

$$= \frac{\sin p}{p} \cdot \frac{\sin Bp}{Bp} + \frac{\sin Bp}{Bp}\cos p - \frac{\sin p}{p}\cos Bp. \tag{28}$$

The derivative of $G(p)$ in integral form is

$$G'(p) = -\frac{\sin p}{2B}\int_{-B}^{B} (1 - x^2)\cos px dx. \tag{29}$$

To find the maximum and minimum values of $G(p)$, we observe that the derivative is zero at $p = n\pi$ for all integer n with additional roots at p values where the integral vanishes. The maximum of the function can be found at $p = 0$ and the first minimum at $p = \pi$. This minimum was shown by computer analysis to be the

largest minimum value of $G(p)$. The values of $G(p)$ at these two extremes are

$$G(p) = \begin{cases} 1, & \text{at } p = 0 \text{ (maximum);} \\ -\dfrac{\sin\pi B}{\pi B}, & \text{at } p = \pi \text{ (minimum).} \end{cases} \tag{30}$$

The greatest strongly stable amplitude gain, the negative of the ratio of the maximum and minimum values of $G(p)$, is $1/\text{sinc}B$. We can express the gain in decibels as

$$\text{gain} = -20\log(\text{sinc}B) = -20\log\left[\frac{\sin[(1-\beta)/(1+\beta)]}{\pi(1-\beta)/(1+\beta)}\right]. \tag{31}$$

Let us compare the stable gain result with that produced by an impulse response of uniform amplitude over the same time interval of length B:

$$h(\tau) = \begin{cases} 1/2B, & (1-B) < \tau < (1+B); \\ 0, & \text{elsewhere.} \end{cases} \tag{32}$$

The frequency response is

$$H(p) = \int_{-\infty}^{\infty} h(\tau)\exp(j\tau p)d\tau = \frac{\sin Bp}{Bp}\exp(jp). \tag{33}$$

The maximum response is at $p = 0$, and, if we confine our attention to the real axis, the largest minimum occurs at $p = \pi$. The associated values of $H(p)$ are

$$H(p) = \begin{cases} 1, & \text{at } p = 0 \text{ (maximum magnitude)} \\ -\dfrac{\sin\pi B}{\pi B}, & \text{at } p = \pi \text{ (minimum on real axis).} \end{cases} \tag{34}$$

The maximum stable amplitude gain is, therefore, the same $1/\text{sinc}B$ function we derived for the linearly apodized impulse response under stricter stability constraints. The apodization for this case did not, therefore, affect the amount of stable gain available. Rather, it improved the quality of that gain. The apodization provides a 90° closed loop phase margin allowing the system to operate with realistic error budgets.

In Table I we show the amount of stable gain available, indicative of the achievable notch depth, for various blocking ratios at the transducer end of the Bragg cell. The blockage must be carefully controlled to achieve a large stable gain. For example, to achieve a 60-dB notch depth, the blocking ratio must be <0.0005; if the Bragg cell has a time–bandwidth product of 1000, the blockage cannot exceed one-half of a resolution element.

Table I. Stable Gain as a Function of the Blocking Ratio at the Transducer End of the Bragg Cell

Blocking ratio	Stable gain (dB)
0.0001	73.9
0.0002	67.9
0.0005	60.0
0.001	54.0
0.002	47.9
0.005	40.0
0.01	33.9
0.02	27.8
0.05	19.7
0.10	13.5

A comparison of modeling results using continuous and sampled digital techniques gives us a simple technique for estimating the accuracy of the discrete presentation. The sampling of the impulse response at $\Delta\tau$ intervals can be interpreted in the following way. The first sample, which is located at $\Delta\tau$, represents the impulse response in the adjacent region from time $\Delta\tau/2$ to $3\Delta\tau/2$, omitting the time interval from zero to $\Delta\tau/2$. Therefore, sampling introduces an effective half-sample time delay into the system. Differences in the stability values obtained by discrete and continuous models can be reconciled with remarkable accuracy by noting that sampling effectively nulls the first $\Delta\tau/2$ interval of the continuous impulse response. Using the previous numerical example, we conclude that at least 1000 impulse samples must be used in a digital model if gains as large as 60 dB are to be modeled accurately.

V. Experimental Results

The impulse response model allows us to relate the closed loop system performance to the open loop response. As noted before, attempts to observe or measure light amplitudes at various planes in the system operating in the closed loop mode influence system performance. We can measure the impulse response directly without perturbing the system and compare it with the model description to estimate the closed loop system performance. We measured the open loop response in a manner similar to that discussed in Sec. III in connection with Fig. 5 with a pure cw tone driving the two orthogonal Bragg cells.

A time domain representation of the impulse response can be obtained by using a short rf burst in the Z-branch as the probe signal. The detector output is displayed on an oscilloscope as shown in Fig. 9(a); the horizontal axis is 1 μs/div, and the vertical axis is a linear scale. The upper trace shows the 1-μs envelope of the rf burst signal that drives the third Bragg cell. The spectral characteristics of the impulse response can be measured as the frequency of the input signal to the Z-branch is swept past the cw reference tone. The use of a network analyzer allows us to measure both the amplitude and phase response as shown in Fig. 9(b). The network analyzer receives two inputs known as reference and test channels. The reference channel is the probe frequency input to Bragg cell in the Z-branch of the interferometer, and the test channel is the detector output.

The vertical scaling in Fig. 9(b) is $\pi/4$ rad/div for the phase response; π crossings therefore occur at the upper and lower extremes of the display. The measured stability is evaluated by subtracting the log amplitude response at the π phase crossings from the response where the phase is zero. Due to the asymmetry, the higher of the two amplitude readings at the π crossings occurs below the central frequency and limits the stable gain to 18 dB.

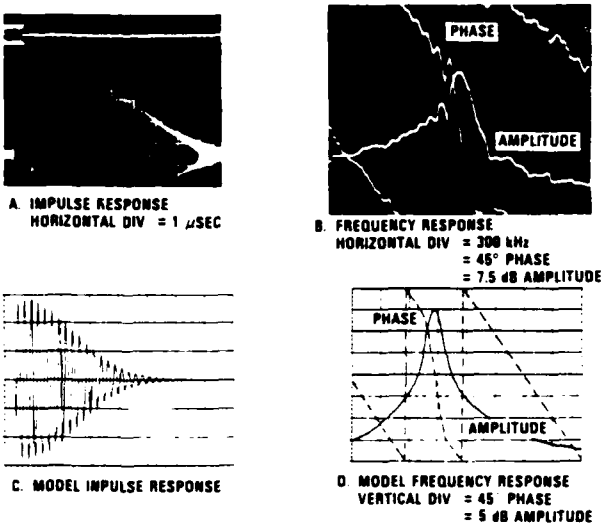

Fig. 9. System response for 5% time delay: (a) measured impulse response; (b) measured frequency response; (c) Gaussian impulse response model; (d) frequency response of Gaussian model.

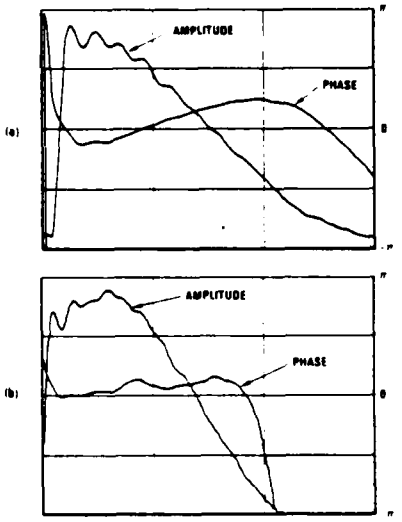

Fig. 10. Inverse transform of measured frequency response: (a) initial performances; (b) improved cell response.

We used the measured experimental results from Fig. 9(a) in our model and calculated the frequency response shown in Fig. 9(d); we predict a stable gain of ~20 dB. We note that the response is symmetric in amplitude because we assumed that the impulse response is real. The measured asymmetric frequency response shows that the time domain response must have some phase errors which cannot be deduced from the measured data shown in Fig. 9(a). To illustrate this phenomenon, Fig. 10(a) shows the results obtained by inverse transforming the measured frequency response seen in Fig. 9(b); this result reveals the location of phase response problems in the time do-

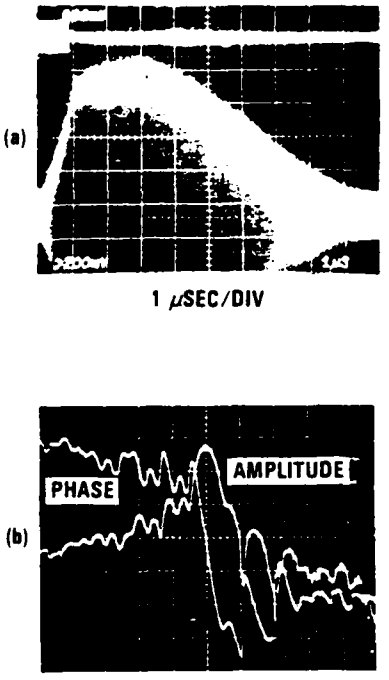

Fig. 11. Improved system response with reduced time delay: (a) measured impulse response; (b) measured frequency response.

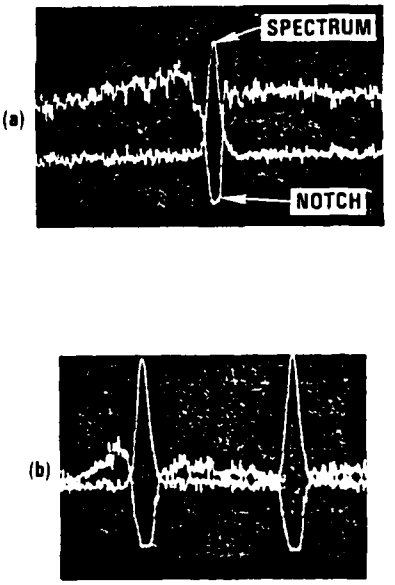

Fig. 12. Experimental results: (a) input spectrum and adaptive system response with a 32-dB notch; (b) two-jammer input spectrum and system response.

main. The leading edge of the impulse response has the most prominent phase errors. When we examined the Bragg cell in an optical interferometer, we found a

two wavelength roll-off in the optical figure caused by rounding of the cell at the tranducer edge. When the cell was repolished, the phase errors were significantly reduced, as shown in Fig. 10(b).

To significantly increase the stable gain we must decrease the relative time delay between the two branches of the interferometer. The time delay observed in the impulse response of Fig. 9(a), ~500 ns, is an accumulation of electrical and acoustical delays in obtaining an optical response from an electrical input. We found that the total electrical delay due to cables and amplifiers was <50 ns; most of the delay is therefore attributed to the Bragg cell driven by the residual signal.

Isotropic Bragg cells redirect diffracted light by twice the Bragg angle; in such a cell we can illuminate the transducer at the positive Bragg angle using the upshifted diffraction mode to minimize the acoustic delay. However, the cells used in our experiments are birefringent, and the geometry is such that the diffracted light is parallel to the transducer for the center frequency. An examination of the Bragg cell driven by $z(t)$ showed that beveled transducer edges were responsible for a large portion of the time delay. Our standard procedure in fabricating Bragg cells is to bevel the edges to minimize chipping during the reduction of the piezoelectric platelet to the final transducer thickness. For the acoustic velocity of these cells, a 0.3-mm bevel results in 485-ns acoustic transit from the transducer to the unshadowed edge of the light. When this cell was repolished to reduce the phase roll-off at the transducer end, we made a special effort to also remove the bevel. The resultant impulse response is shown in Fig. 11(a); the time delay was decreased from 485 to <150ns. By examining the π crossings located at the vertical extremes of the phase response in Fig. 11(b), we conclude that the system can now operate with more than 30-dB stable gain.

An example of stable performance is shown in Fig. 12(a). The lower trace shows the spectrum of the received signal which consisted of a 50-MHz wideband signal and a narrowband jammer at 90 MHz. The horizontal scale is 1 MHz/div, whereas the vertical scale is 10 dB/div. The upper trace shows the notch formed adaptively by the system; this trace was obtained by subtracting the logarithm of the output signal from that of the input signal. It is, then, a measure of the frequency response of the system at steady state and shows a notch depth of ~32 dB. We also tested the system using multiple jammers over various parts of the frequency band. Figure 12(b) shows the results for the case of two equal jammers, each 20 dB above the signal; the jammers are ~4 MHz apart and both are approximately at midband. We see that the notch depths are of the order of 20–25 dB.

VI. Summary and Conclusions

We have constructed and tested an optical breadboard system for adaptive filtering applications. We developed several diagnostic and analytical tools for relating the open loop response to the closed loop performance levels. The key diagnostic tool is a network analyzer that allows us to measure accurately both the amplitude and phase of the frequency response of the system. By using this tool we could rapidly align the system in an open loop mode and estimate the performance in the closed loop mode.

The key analytic tool is an improved method for modeling system performance. In this model, the entire optical system is represented by an linear transfer function that includes all known features of the system. This model provides a methodology for analyzing the impact of hardware imperfections, such as finite optical apertures and wave-front aberrations, on the transient and steady-state system response for any generalized signal inputs.

To analyze system stability, we focused on the pure jammer case where the transfer function can be reduced to an impulse response placed in the feedback loop, allowing control theory concepts to be applied. After overcoming some anomalies that tend to plague digital simulations of analog systems, we found that the most important criterion for stable performance is to reduce the relative time delays to a minimum and to weight properly the impulse response. We have developed a strong stability criterion in which we can calculate the expected level of performance for a given degree of phase or gain margin.

The experimental results confirmed in an iterative and interactive way the usefulness of these tools. We demonstrated more than 30-dB notch depths for a system having a 50-MHz bandwidth and a time–bandwidth product of 2000. We also demonstrated that notches are adaptively established for two jammers of unknown amplitudes, frequencies, and phases.

We are pleased to acknowledge the contributions of G. S. Moore, C. D. Rosier, and E. H. Tegge to the design and fabrication of the electronic hardware and those of M. D. Koontz to the design and fabrication of the optical system. This work was supported in part by the U.S. Army Research Office.

References

1. A. VanderLugt, "Adaptive Optical Processor," Appl. Opt. 21, 4005 (1982).
2. A. VanderLugt, "Optical Transversal Processor for Notch Filtering," Opt. Eng. 23, 312 (1984).
3. J. F. Rhodes and D. E. Brown, "Adaptive Filtering with Correlation Cancellation Loop," Proc. Soc. Photo-Opt. Instrum. Eng. 341, 140 (1983).
4. J. F. Rhodes, "Adaptive Filter with a Time-Domain Implementation using Correlation Cancellation Loops," Appl. Opt. 22, 282 (1983).
5. D. Psaltis and J. Hong, "Adaptive Acoustooptic Filter," Appl Opt. 23, 3475 (1984).
6. A. VanderLugt, "Crossed Bragg Cell Processors," Appl Opt 23, 2275 (1984).
7. M. A. Krainak and D. E. Brown, "Interferometric Triple Product Processor (Almost Common Path)," Appl. Opt. 24, 1385 (1985)

APPENDIX C

OPTICAL ADAPTIVE FILTER; ANALYTICAL MODEL

PRESENTED AT OPTICAL INFORMATION PROCESSING II

SPIE SYMPOSIUM ON OPTICS AND OPTOELECTRONIC SYSTEMS

ORLANDO, FLORIDA, 31 MARCH 1986

TO BE PUBLISHED IN PROCEEDINGS SPIE

VOLUME 639, OPTICAL INFORMATION PROCESSING II

Optical Adaptive Filter; Analytical Model

A. M. Bardos

Harris Corporation, Government Information Systems Division
Mail Stop 13-7741, P.O. Box 98000, Melbourne, Florida 32902

Abstract

A general analytical model is developed for an adaptive optical filter. This model is used to explain system performance limitations and relate them to specific imperfections of the hardware implementation. Optimization of the system transfer function shows that 30-35 dB of stable gain can be achieved with reasonable hardware and system tolerances.

Introduction

In earlier analyses of adaptive filtering, VanderLugt[1,2] described the basic operation of a frequency domain processor in terms of an analogy to a discrete transversal filter. The transversal filter is implemented as an optically tapped Bragg cell delay line that contains time samples of the received signal. The output of each tap is weighted, as determined by the processing operation, and summed to provide an estimate of a signal. The estimated signal $\hat{s}(t)$ is subtracted from the received signal s(t) to provide a residual signal z(t) which controls the tap weights to form an adaptive linear predictive system.

Experimental result by Beaudet[3] and coworkers, reported in a companion paper in these proceedings, however indicated a need for a more explicit model able to describe the effects of hardware limitations on system performance.

System description

Figure 1 shows only the key elements of the interferometric optical system and suggests how we plan to model its system response in a feedback loop. We represent all three Bragg cells with idealized transducer heights that render the region of interaction between light and acoustic waves into a square format. The idealization shown generates the same results as obtained by using Bragg cells with suitable anamorphic optical systems described in Reference 3. The Bragg cells, with respect to an observation plane external to the interferometer, appear to overlap as shown in Figure 2a. We refer to this plane as the tap weight plane. The transducer of the Bragg cell that is disposed at 45° to the first two must lie on the bisector established by the other two transducers.

The two orthogonal cells of the S-branch receive the signal s(t), and produce a light amplitude profile on the diagonal that is proportional to the instantaneous power spectrum of s(t). Upon interference with the properly scaled instantaneous spectrum of the residual signal z(t), the strong spectral terms are enhanced, and thus can be subtracted by the feedback loop.

Figure 2b shows the spectral plane of the Bragg cells. Suppose that s(t) consists of two CW signals which appear at both positive and negative frequencies along the two spatial frequency axes; we assume Raman-Nath operation for sake of this illustration. The signals interact to also provide a set of four spectral components in each frequency quadrant; these components are shown as filled circles. The upper right quadrant is marked (++), to indicate that both cell No. 1 and cell No. 2 produce a frequency upshift. In our model the upper left quadrant is used; in this quadrant the frequencies have a downshift/upshift structure. The region in the upper left quadrant occupied by the photodetector covers the domain of overlapping frequencies.

Suppose that the third cell is driven by z(t) which also consists of two frequencies shown as open circles; these signals are shown with a slightly lower frequency so that we can visualize some important relationships. It is easy to see that these frequency components overlap on the diagonal, provided that the frequencies of z(t) equal those of s(t) and that the optical system magnifies the spectrum of cell No. 3 by $\sqrt{2}$.

Model development

We developed a linear model that describes the optical system in terms of a real-valued transfer function G, referred to as the grand system kernel. The electrical system model represents the optical system as a time dependent (adaptive) frequency response in a feedback system which subtracts the signal estimate $\hat{s}(t)$ from the signal input s(t), generating the error function z(t) as shown in Figure 3a. To make a linear model possible, we treat

the inputs to the three Bragg cells as independent functions even though the same signal might be driving two of those cells. The signal estimate $\hat{s}(t)$, the output of the detection subsystem (detector, filter, amplifier, etc.), can be expressed as a function of the signal input s(t) which drives the two orthogonal cells, the residual function z(t) which drives the third cell, and the transfer function G:

$$\hat{s}(t) = \int\int\int_{-\infty}^{\infty} s(t')s(t'')\, z(t''')\, G(t',t'',t''',t)dt'\, dt''\, dt''' \tag{1}$$

The system kernel function G describes all the physical properties of the optical system; that is, all the phase and amplitude effects as well as the convolution and correlation nature of the architecture. Even causality is embedded in the kernel; instead of using finite limits of integration, we require that G vanish for non-causal combinations of the four arguments to prevent the future from influencing the present. The kernel function G is the transfer function of the optical subsystem shown enclosed by dashed lines in Figure 1.

Let us first consider a Bragg cell whose inputs are the amplitude a(x,y,t) of the illuminating beam and the RF drive signal s(t); its output $a_1(x,y,t)$ is the amplitude of the diffracted light. We use a simplified model, in which the Bragg cell is treated as a planar time-varying phase mask, so that the illumination wavefront and the output light amplitude interact only at a single space-time point. Therefore we seek a Bragg cell transfer function P of the following form:

$$a_1(x,y,t) = \int_{-\infty}^{\infty} a(x,y,t)s(t')P(t',t,x,y)\, dt' \tag{2}$$

This formalism has sufficient power to express the relevant performance characteristics of a Bragg cell which performs five key functions: (1) it band-limits the electrical signal, (2) it generates a propagating acoustic wave, (3) it performs a spatial aperture weighting operation due to acoustic attenuation and the finite length of the cell, (4) it converts acoustic pressure waves into multiplicative perturbations of the input optical wave, thus generating the diffracted output light, and (5) it selects either the negative or the positive spatial frequencies depending on the illumination geometry.

We shall combine the effects of temporal band limitation and Bragg selectivity into a single composite transfer function that converts the input RF drive function into an effective complex drive signal containing only positive temporal frequencies for an upshift configuration, or negative ones for a downshift geometry. This band limitation can be expressed as a multiplication by the frequency response B(f) in the frequency domain, or as a convolution with the impulse response b(t) in the time domain. For an upshift Bragg cell geometry with bandwidth δf, centered at f_c, and uniform frequency response, we have

$$B^+(f) = \mathrm{rect}[(f-f_c)/\delta f]$$

$$b^+(t) = F^{-1}\{B(f)\} = \delta f \exp(j2\pi f_c t)\, \mathrm{sinc}(\delta f t) \tag{3}$$

For a downshift configuration we need only to use a negative carrier frequency in these equations to obtain $B^-(f)$ or $b^-(t)$.

The propagation of the signal in the x direction with acoustic velocity v and a temporal offset t_o can be described by replacing the time variable t with $t-x/v-t_o$. However, in keeping with the cascaded linear model, we perform this operation using the sifting property of the delta function. We shall model the conversion of the traveling acoustic pressure waves into light amplitude by assuming that the input light is retarded by the index waves as expressed by an exponential multiplier $\exp[j\epsilon\sigma(x,t)]$, where $\sigma(x,t)$ is the effective signal traveling in the Bragg cell, and ϵ is an efficiency term. If the argument is small, this multiplier is approximated by $1+j\epsilon\sigma(x,t)$. We drop the unity term which represents the undiffracted light normally blocked in the optical system. We define the amplitude weighting aperture function as w(x,y); the output light amplitude is therefore given by equation (2) with

$$P(t',t,x,y) = jcw(x,y)b(t-x/v-t_0-t') \tag{4}$$

By cascading the transfer functions of two crossed Bragg cells we obtain the light output of the S-branch as

$$a_{12}(x,y,t) = \iint_{-\infty}^{\infty} k_{12}(x,y,t,t',t'')\ s(t')\, s(t'')dt'dt'' \tag{5a}$$

where

$$k_{12}(x,y,t,t',t'') = -\varepsilon^2 w_1(x,y)w_2(x,y)b^-(t-x/v-t_1-t')\, b^+(t-y/v-t_2-t'')a(x,y,t) \tag{5b}$$

In the 2-branch of the interferometer we have a single Bragg cell that is rotated 45° with respect to those in the S-branch, and is scaled optically so that its spectrum matches the scale of the cross-spectral terms of the S-branch. The propagation is along the diagonal of the second quadrant with an effective acoustic velocity of $v/\sqrt{2}$ to properly stretch the spectrum; the distance from the transducer of an arbitrary point with coordinates x,y is $(y-x)/\sqrt{2}$. The acoustic propagation time, the ratio of distance and effective velocity, is therefore $(y-x)/v$ for this Bragg cell. The optical output of cell No. 3, referenced to the tap weight plane, can be written as

$$a_3(x,y,t) = \int_{-\infty}^{\infty} k_3(x,y,t,t''')\, z(t''')dt''' \tag{6a}$$

where

$$k_3(x,y,t,t''') = jcw_3(x,y)b^+(t-y/v+x/v-t_3-t''')a'(x,y,t) \tag{6b}$$

The light amplitudes a_{12} and a_3 of the respective tap weight planes are Fourier transformed in the variables x and y to obtain the spectral plane amplitudes A_{12} and A_3 as functions of the spatial radian frequencies α and β. The two branches are combined by a beamsplitter so that the light intensity at the spectral plane is

$$I(\alpha,\beta,t) = |A_{12}|^2 + |A_3|^2 + 2\mathrm{Re}[A_{12}A^*_3]. \tag{7}$$

The first two terms are baseband signals whose possible effects in generating spurious in-band frequency terms we ignore in this analysis. The crossterm provides the in-band signal term that is integrated by the detector whose aperture function is $D(\alpha,\beta)$. The signal estimate generated by the detector is

$$\hat{s}(t) = \iint_{-\infty}^{\infty} D(\alpha,\beta)2\mathrm{Re}[A_{12}(\alpha,\beta,t)A^*_3(\alpha,\beta,t)]d\alpha d\beta. \tag{8}$$

From which we obtain the grand system kernel formulation of equation (1) with

$$G(t',t'',t''',t) = \iint_{-\infty}^{\infty} D(\alpha,\beta)2\mathrm{Re}[K_{12}(\alpha,\beta,t,t',t'')K^*_3(\alpha,\beta,t,t''')]d\alpha d\beta \tag{9}$$

where

$$K_{1,2}(\alpha,\beta,t,t',t'') = \iint_{-\infty}^{\infty} k_{1,2}(x,y,t,t',t'')e^{j(\alpha x+\beta y)}dxdy$$

and

$$K_3(\alpha,\beta,t,t''') = \iint_{-\infty}^{\infty} k_3(x,y,t,t''')e^{j(\alpha x+\beta y)}dxdy \tag{10}$$

The detector collection aperture needs to be small enough to reject spurious spectral terms yet large enough to gather the desired signal located around the diagonal of the second quadrant. While the illustration in Figure 2b shows all the spectral terms that acoustic cells operating in the Raman-Nath regime would generate, our model of the Bragg selective devices has already rejected most of the undesirable terms. Only the off-diagonal cross-spectral terms of the S-branch survive. It is important to observe that these terms do not contribute to the signal estimate if they are sufficiently far off axis, since the spectrum due to the Z-branch, and hence the product terms in (8), are zero at those locations. We conclude therefore, that an open detector aperture; i.e. integration over the complete spectral plane leads to a good representation for most cases. As one would expect, the kernel is time stationary in the sense that it depends on time only through the differences t-t', t-t'', and t-t'''. We shall now examine a very important special case where the time dependence can be reduced to a single variable $\tau = t-t'''$, simplifying the system kernel model to a convolution with an impulse response.

Impulse response model

Let us examine the case of a pure jammer input to the system without a wideband signal term present. For a sinusoidal input of frequency f_o in the two orthogonal cells, using planewave illumination in both branches with a phase difference of ϕ, we obtain an impulse response formulation for the signal estimate

$$\hat{s}(t) = \int_{-\infty}^{\infty} z(t')h(t-t')dt' \tag{11a}$$

$$h(\tau) = \iint_{-\infty}^{\infty} 2\mathrm{Re}\left[w(x,y)e^{j2\pi(y-x)f_o/v+j\theta}\, b^*(\tau-y/v+x/v-t_3)\right]dxdy \tag{11b}$$

where w(x,y) is the joint window function for all three cells, and θ collects all phase terms.

$$w(x,y) = \varepsilon^3 w_1(x,y)w_2(x,y)w_3^*(x,y)$$
$$\theta = \phi + 2\pi f_o(t_1-t_2)-\pi/2. \tag{11c}$$

The complete optical system and the input signals to the S-branch are combined into this real-valued impulse response $h(\tau)$. This unique case, in spite of its simplicity, yields powerful analytical and experimental results that helped to control instabilities.

Stability criteria

Let us consider a negative feedback system having a filter in the return path with impulse response $h(\tau)$, as shown in Figure 3c. We determine stability in terms of the complex frequency response of the feedback path: the transform $H(\omega)$ must not circle -1, the critical stability point in the complex plane. A sufficient condition of stability may be stated as requiring that the Fourier transform of the impulse response must not have any negative real values left of the -1 point on the real axis, i.e., the system should have less than unity gain at any frequency with a 180° phase shift. Since the negative crossings cannot go past the -1 point, the maximum achievable gain can be determined from the ratio of the maximum and minimum values on the real axis.

Optimization criteria

While exercising the model, we generally sought conditions for which we can obtain the deepest jammer suppression notch. To determine the closed-loop stability of the single-jammer situation using the Fourier transform criterion, we write the open-loop impulse response h(t) in the following form:

$$h(t) = \begin{cases} w(t)\cos(\omega_0 \tau), & \beta T \le \tau \le T \\ 0, & \text{elsewhere} \end{cases} \tag{12}$$

Here ω_0 represents the jammer frequency we desire to suppress, βT is a delay generated by hardware limitations, T is the Bragg cell fill time, and w(t) is a window function describing the amplitude profile of the impulse response produced by the geometry and illumination of the optical system. The closed-loop frequency response $F(\omega)$ can be expressed as

$$F(\omega) = 1/[1 + H(\omega)]. \tag{13}$$

The stability criterion, expressed in terms of $F(\omega)$, is that the closed-loop frequency response phase never reaches 180°, regardless of gain.

We generated computer optimized window functions for various blocking ratio values β, which expresses the inaccessible fraction of the aperture time T. Figures 4a and 4b show the results of this optimization for a delay equal to 1.5% of the length of the impulse response (β=0.015). From Figure 4b, we note that a stable gain of 45 dB is theoretically predicted for the window function shown in Figure 4a. However, even the slightest phase error in the system will suddenly create instabilities at the point where the phase nearly reaches 180° inside the central lobe, limiting its stable performance to only 28 dB of suppression. This kind of optimization therefore leads to systems that are intolerant to small phase errors. To develop more rugged system performance, we defined a more stringent stability criterion that requires that the phase of the closed-loop frequency response remain between -90° and 90°. Stated in terms of the open loop frequency response, we require that the real part of $H(\omega)$ be greater than -1 at all values of ω, not only on the real axis. We refer to this condition as the strong stability criterion; it ensures a softer, more nearly monotonic frequency response which, in turn, guarantees a more gradual performance degradation as phase errors are introduced.

For a blocking ratio of β=0.015, we can achieve a strongly stable suppression of 32 dB with the optimum impulse function as shown in Figure 4c. From Figure 4d we see that the phase response approaches 180° much more gently than in Figure 4b. This concept of strong stability and the demonstrated experimental results can be used to design a rugged realizable system that has maximal tolerance to phase errors induced by environmental conditions such as vibration and temperature changes.

Computer optimizations based on the strong stability criterion yield an interesting result: the optimum window function is a linear taper from the initial maximum to zero at $t=T+\beta T$. Let us analyze the stability of a linearly tapered impulse response at baseband. We introduce the parameter B to define the impulse response and note the relationship that $\beta=(1-B)/(1+B)$. We then have that

$$h(\tau) = \begin{cases} (2-\tau)/2B, & (1-B) < \tau < (1+B) \\ 0, & \text{elsewhere.} \end{cases} \tag{14}$$

The real part of the frequency response is

$$G(p) = \mathrm{Re}[H(p)] = \mathrm{Re}\left[\int_{-\infty}^{\infty} h(\tau) e^{jp\tau}\, d\tau\right]$$

Evaluating the integral, we obtain

$$G(p) = \frac{\sin p}{p} \cdot \frac{\sin Bp}{Bp} + \cos p \frac{\sin Bp}{Bp} - \frac{\sin p}{p} \cos Bp \tag{15}$$

The greatest strongly stable amplitude gain, the negative of the ratio of the maximum and minimum values of G(p) is 1/sincB. We can express the gain in decibels as

$$\text{Gain} = -20 \log(\text{sinc}B) = -20 \log \left[\frac{\sin[\pi(1-B)/(1+B)]}{\pi(1-B)/(1+B)} \right] \tag{16}$$

In Table 1 we show the amount of stable gain available, indicative of the achievable notch depth, for various blocking ratios at the transducer end of the Bragg cell. The blockage must be carefully controlled to achieve a large stable gain. For example, to achieve a 60 dB notch depth, the blocking ratio must be less than 0.0005; if the Bragg cell has a time bandwidth product of 1000, the blockage cannot exceed one-half of a resolution element. While this table is only valid for the linearly tapered, baseband impulse response, it provides a strong indication of performance trends for the general case.

Table 1: Stable gain as a function of the blocking ratio at the transducer end of the Bragg cell.

Blocking Ratio	Stable Gain (dB)
0.0001	73.9
0.0002	67.9
0.0005	60.0
0.001	54.0
0.002	47.9
0.005	40.0
0.01	33.9
0.02	27.8
0.05	19.7
0.10	13.5

Summary

We have developed an improved method for modeling the system performance. In this model, the entire optical system is represented by an linear transfer function that includes all known features of the system. This model provides a methodology for analyzing the impact of hardware imperfections, such as finite optical apertures and wavefront aberrations, on the transient and steady state system response for any generalized signal inputs.

To analyze system stability, we focused on the pure jammer case where the transfer function can be reduced to an impulse response placed in the feedback loop, allowing control theory concepts to be applied. We found that the most important criterion for stable performance is to reduce the relative time delays to a minimum and to properly weight the impulse response. We have developed a strong stability criterion in which we can calculate the expected level of performance for a given degree of phase or gain margin.

Acknowledgements

I am pleased to acknowledge the contributions of Dr. A. VanderLugt and W. R. Beaudet to the understanding of adaptive optical systems. This work was supported, in part, by the U. S. Army Research Office.

References

1. A. VanderLugt, "Adaptive Optical Processor", Appl. Opt., Vol. 21, p. 4005 (1982).
2. A. VanderLugt, "Optical Transversal Processor for Notch Filtering," Optical Engr., Vol. 23, p. 312 (1984).
3. W. R. Beaudet, "Optical Adaptive Filter; Experimental Results", SPIE Conference 639 paper 27, April 86.

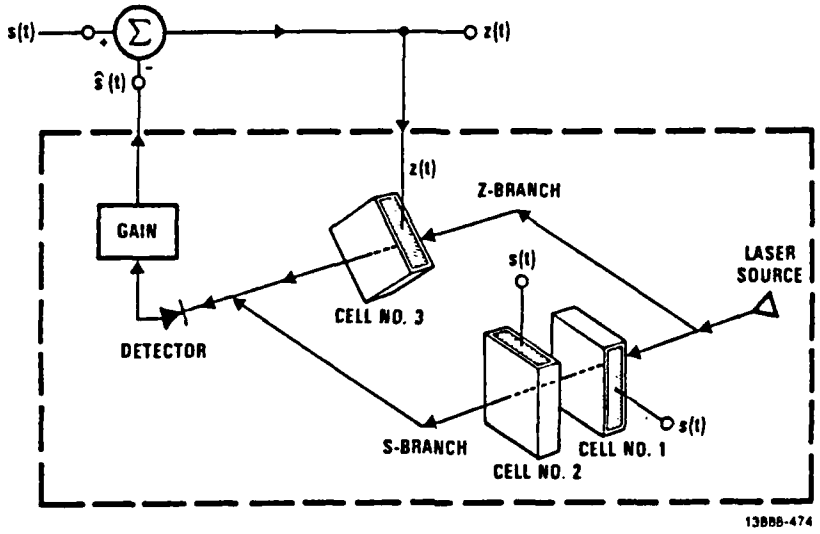

Figure 1. Simplified System Schematic

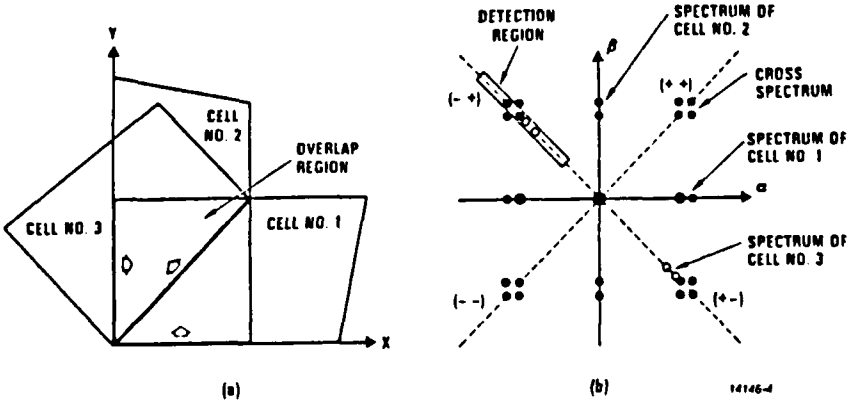

Figure 2. Signal Geometry:
(a) Tap Weight Plane;
(b) Spectral Plane

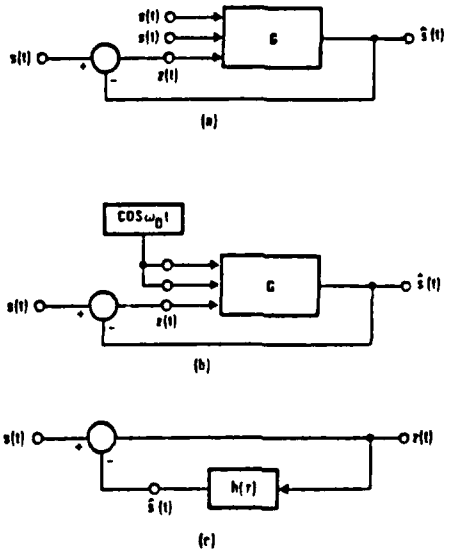

Figure 3. System Response Models:
(a) Full model;
(b) Pure jammer model;
(c) Impulse response model

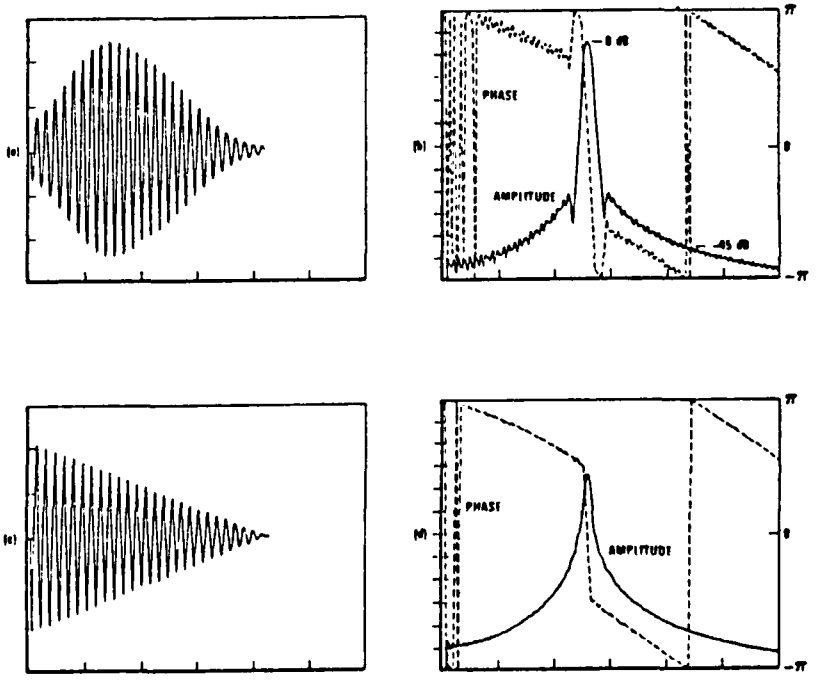

Figure 4. Optimized System Responses:

(a) Gaussian impulse response;
(b) Frequency response for Gaussian model (5dB/div.);
(c) Linearly apodized impulse response;
(d) Frequency response of linear model (5dB/div.)

APPENDIX D

OPTICAL ADAPTIVE FILTER; EXPERIMENTAL RESULTS

PRESENTED AT OPTICAL INFORMATION PROCESSING II

SPIE SYMPOSIUM ON OPTICS AND OPTOELECTRONIC SYSTEMS

ORLANDO, FLORIDA, 31 MARCH 1986

TO BE PUBLISHED IN PROCEEDINGS SPIE

VOLUME 639, OPTICAL INFORMATION PROCESSING II

Optical Adaptive Filter; Experimental Results

W. R. Beaudet, A. M. Bardos, and A. VanderLugt

Harris Corporation, Government Information Systems Division
Mail Stop 13-7747, P.O. Box 98000, Melbourne, Florida 32902

Abstract

An interferometric optical system is configured with an active feedback loop as an optical adaptive filter. The closed loop characteristics of the system are found to be sensitive to alignment and aberrations. An open loop diagnostic procedure is applied to the system to develop stability to a level supporting 30 db adaptively formed frequency rejection notches. The time delay in the closed loop signal path is found to be the limiting factor in system performance.

Introduction

In this paper we discuss the experimental results associated with the development of an interferometric system which allows for adaptive processing of wide band signals. This system can be viewed as a transversal filter with feedback[1,2] for applications such as channel equalization for wideband communication or adaptive temporal filtering. Similar architectures can be configured for the processing of phased array radar signals for null steering or beam forming[3]. Here we concentrate on this architecture as it applies to the removal of an agile jammer in a wideband spread spectrum system. The frequency, amplitude and phase of an interferor are unknown, for which a notch filter is constructed to eliminate the unwanted signal and therefore improve the signal to noise ratio. We have found the stability of the feedback system to be of paramount importance in achieving greater than 30 db notch depths such as those shown in Figure 1. One trace shows the spectrum of a received signal which consisted of a 50 MHz wideband signal and a narrowband jammer at 90 MHz. The horizontal scale is 1 MHz per division while the vertical scale is 10 db per division. The second trace shows the notch formed adaptively by the system. This trace was obtained by subtracting the logarithm of the output signal from that of the input signal. It is, then, a measure of the frequency response of the system at steady state, and shows a notch depth of about 32 db.

System description

Figure 2a is a simplified schematic of the Mach-Zehnder interferometer chosen for our experimental system. A received signal s(t) is input to both Bragg cells of the S Branch leg. S(t) is also applied to a summing junction where z(t) is formed. This signal represents the difference between s(t) and the signal estimate. Z(t) is the output signal with slowly varying components, jammers, removed. Two states of this input to cell 3 will be considered for discussion. In the closed loop state, the detector output will be fed back through the summing junction to the input to cell 3. The gain will be referenced for our discussion to 0 db when the magnitude of s(t) is equal to the signal estimate at the summing junction. The amount of excess gain that can be tolerated while maintaining system stability will be a measure of the system effectiveness in creating notch depths. That is, the notch depth attainable increases as more gain is available to the feedback loop. The open loop state refers to the condition where the detector output is prevented from reentering the system by breaking the gain path to the summing junction.

Figure 2b is a schematic of the optical system implemented. This configuration allows us access to intermediate processing planes useful for alignment and diagnostic purposes, although at the expense of a more nearly common path implementation which would be less sensitive to vibration, thermal gradients, air currents and acoustic coupling. The light source is a 15 mw Helium-Neon laser whose output beam is expanded by lenses L1 and L2, and divided into two beams by beamsplitter BS1. Cylindrical lenses surround the Bragg cells to focus the light into a horizontal line for efficient illumination. The Bragg cells are constructed from TeO_2 material which is oriented to operate in the slow shear mode. The bandwidth of each cell is 50 MHz, centered at 90 MHz, and the cell fill time is 40 usec. Quarter-wave plates, not shown in Figure 2b, produce circularly polarized light at the entrance to Bragg cells 1 and 3 to improve diffraction efficiency and spectral band uniformity. Cylindrical lenses C2 through C6 serve to mutually image the two Bragg cells into a square format at the tap weight plane. Lenses C8 and L8 create the Fourier transform just beyond the beam combiner at the spectral plane where the two Fourier transforms are joined to make heterodyne detection possible. Lens L9 serves to demagnify the transform onto the photodetector.

The feedback cancellation can be considered in the frequency plane as cells 1 and 2 forming a reference region containing the spectrum of signals present in the system. Cell 3 is then used to form the instantaneous power spectrum of s(t) which is used as a template to separate slowly varying signals, such as a jammer, from the signal so that it can be used in the feedback loop. As cell 3 forms the signal minus the signal estimate, a varying signal that contains information does not allow the feedback signal to null s(t).

As in any interferometer, the interfering beams must overlap to produce an output at the photodetector. Since the interference is coherent, the light beams must also be colinear or phase differences across the overlap will decrease the output. Preliminary alignments obtained by visual observation of the light beams produced a detector output over the frequency band. The two legs were properly oriented and scaled such that any frequencies in the Z branch leg would track the corresponding diagonal spot produced in the reference leg. However, closed loop operation produced oscillations when the system gain was increased beyond 0 db or that required to produce a photodetector output equivalent to the input signal in the open loop mode. Here frequencies that were stable produced 3 to 6 db of cancellation. The visual alignment done to this point was not phase competent to predict the phase relation of feedback signals across a band of interest.

Initial phase alignment

Analog electrical signal processing techniques are readily available to provide this information but our optical system must provide electrical responses to utilize them. One such way to accomplish this is to use the photodetector output and the drive signal input. A network analyzer was used in this manner to produce the responses measured in Figure 3. The phase and amplitude of the detector output were measured relative to the Bragg cell input drives in the open loop response mode. The reference channel was driven with the same signal as the three Bragg cells, and the channel under test received the photodetector output. A necessary condition for closed loop stability is that the open loop system phase response must not pass through 180 degrees at any point where the system gain is greater than one. Figure 3a shows the amplitude and phase from the network analyzer at the initial state of alignment. The phase is shown by the sawtooth waveform, where one division represents 90 degrees of phase and the horizontal scale is 100 KHz per divisison. As we see, the phase changes by 360 degrees at approximately 100 KHz intervals for this early stage of alignment. By adjusting the relative positions of the Bragg cells, we removed the linear component of the phase change to the degree shown in Figure 3b. Here we see that the phase is nearly flat over approximately 10 MHz of the passband. The residual phase change is slightly curved; this is indicative of a difference in the wavefront curvatures from the two branches of the system. The upper trace in Figure 3b shows that the amplitude response has a 2.5 db variation over a 10 MHz frequency band centered at 90 MHz.

The curvature is a second order effect that is generally not noticed until the linear phase has been fully compensated; it represents a few wavelengths of departure from telecentric operation and normally cannot be detected by visual alignment alone. The phase curvature is more readily observed in Figure 3c where we display the response in the passband from 70 to 110 MHz. We note that the phase varies slowly near 90 MHz and then with increasing rapidity, as is characteristic of a quadratic function, near the band edges. Figure 3d shows the next stage of correction; there is still a 90 degree phase shift over the bandpass and a significant change in the amplitude response. The amplitude response is a strong function of the Bragg cell alignment. We could have adjusted the Bragg angle for more uniform response but decided to optimize the response at midband to obtain the highest possible signal to noise ratio (SNR). At this stage of system alignment we obtained about 12 db of jammer suppression; to obtain more suppression we needed to further analyze the basic causes of system instability and find ways to further modify the hardware based on the analytical results.

Impulse response considerations

To simplify examination of the system dynamics and to understand the criteria of stability, the system is reduced to a treatment of the Z branch leg as the feedback element and the reference leg as an established reference pattern. This is valid for the case of a CW jammer[4,5]. This impulse response model allows us to relate the closed loop system performance to the open loop response. Attempts to observe or measure light amplitudes at various planes in the system operating in the closed loop mode influence the system performance. However, we can measure the open loop impulse response directly without perturbing the system, and compare it with the model description to estimate the closed loop system performance. We measured the open loop response in a manner similar to that in connection with Figure 3, with a pure CW tone driving the two orthogonal Bragg cells.

A time domain representation of the impulse response can be obtained by using a short RF burst in the Z branch as the probe signal. The detector output is displayed on an oscilloscope as shown in Figure 4a; the horizontal axis is 1 us per division and the

vertical axis is a linear scale. The upper trace shows the 1 us envelope of the RF burst signal that drives the third Bragg cell. The spectral characteristics of the impulse response can be measured as the frequency of the input signal to the Z branch is swept past the CW reference tone. The use of a network analyzer allows us to measure both the amplitude and phase response as shown in Figure 4b. For this measurement the reference channel is the probe frequency input to the Bragg cell in the Z branch of the interferometer and the test channel is the detector output.

The vertical scaling in Figure 4b is 90 degrees per division for the phase response; 180 degree crossings therefore occur at the upper and lower extremes of the display. The measured stability is evaluated by subtracting the log amplitude response at the 180 degree phase crossings from the response where the phase is zero. Due to the asymmetry, the higher of the two amplitude readings at the 180 degree crossings occurs below the central frequency and limits the stable gain to 18 db which will adapt to produce approximately 18 db notches.

We used the measured experimental results from Figure 4a in our model and calculated the frequency response shown in Figure 4d; we predict a stable gain of about 20 db. We note that the response is symmetric in amplitude because we assumed that the impulse response is real. The measured asymmetric frequency response shows that the time domain response must have some phase errors which cannot be deduced from the measured data shown in Figure 4a. To illustrate this phenomenon, Figure 5a shows the results obtained by inverse transforming the measured frequency response seen in Figure 4b; this result reveals the location of phase response problems in the time domain. The leading edge of the impulse response has the most prominent phase errors. When we examined the Bragg cell in an optical interferometer, we found a two wavelength roll-off in the optical figure caused by rounding of the cell at the transducer edge. When the cell was repolished, the phase errors were significantly reduced, as shown in Figure 5b.

To significantly increase the stable gain we must decrease the relative time delay between the two branches of the interferometer. The time delay observed in the impulse response of Figure 4a, approximately 500 ns, is an accumulation of electrical and acoustical delays in obtaining an optical response from an electrical input. We found that the total electrical delay due to cables and amplifiers was less than 50 ns; most of the delay is therefore attributed to the Bragg cell driven by the residual signal.

Isotropic Bragg cells redirect diffracted light by twice the Bragg angle; in such a cell we can illuminate the transducer at the positive Bragg angle, using the upshifted diffraction mode to minimize the acoustic delay. However, the cells used in our experiments are birefringent and the geometry is such that the diffracted light is parallel to the transducer for the center frequency. An examination of the Bragg cell driven by z(t) showed that beveled transducer edges were responsible for a large portion of the time delay. Our standard procedure in fabricating Bragg cells is to bevel the edges to minimize chipping during the reduction of the piezoelectric platelet to the final transducer thickness. For the acoustic velocity of these cells, a 0.3 mm bevel results in 485 ns acoustic transit from the transducer to the unshadowed edge of the light. When this cell was repolished to reduce the phase roll-off at the transducer end we made a special effort to also remove the bevel. The resultant impulse response is shown in Figure 6a; the time delay was decreased from 485 ns to less than 150 ns. By examining the 180 degree crossings located at the vertical extremes of the phase response in Figure 6b, we conclude that the system can now operate with more than 30 db stable gain.

Summary

We have constructed and tested an optical breadboard system for adaptive filtering applications. We developed several diagnostic and analytical tools for relating the open loop response to the closed loop performance levels. The key diagnostic tool is a network analyzer that allows us to accurately measure both the amplitude and phase of the frequency response of the system. By using this tool we could rapidly align the system in an open loop mode and estimate the performance in the closed loop mode. The importance of time delays became quantifiable. This approach was instrumental in achieving system stability which supported 30 db adaptively formed notch depths.

We are pleased to acknowledge the contributions of G. S. Moore, C. D. Rosier, and E. H. Tegge to the design and fabrication of the electronic hardware, and those of M. D. Koontz to the design and fabrication of the optical system. This work as supported, in part, by the U. S. Army Research Office.

References

1. A. VanderLugt, "Adaptive Optical Processor", Appl. Opt., Vol. 21, p. 4005 (1982).
2. A. VanderLugt, "Optical Transversal Processor for Notch Filtering", Opt. Eng., Vol. 23, p. 312 (1984).
3. D. Psaltis and J. Hong, "Adaptive Acoustooptic Filter", Appl. Opt., Vol. 23, p. 3475 (1984).
4. A. M. Bardos, W. R. Beaudet, and A. VanderLugt, "Stability Considerations for Adaptive Optical Filtering", submitted to Applied Optics.
5. A. M. Bardos, "Optical adaptive filter; analytical model", SPIE Conference 639 paper 26, April 86.

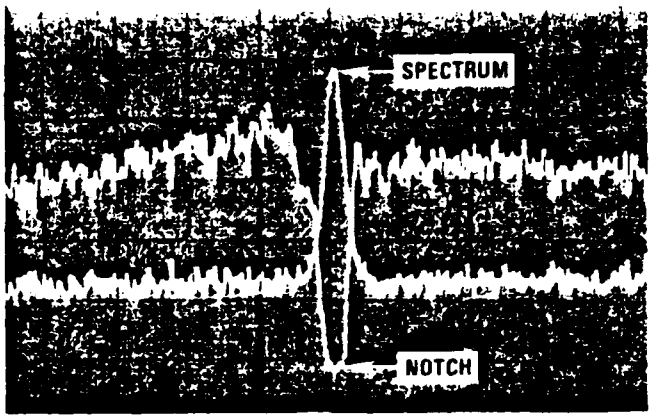

Figure 1. Input spectrum and adaptive system response with a 32 dB notch

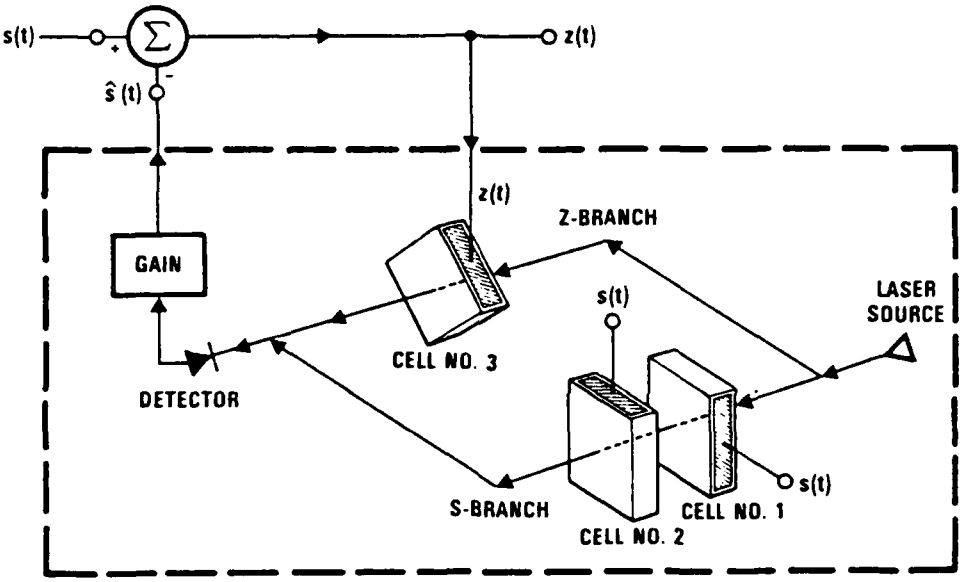

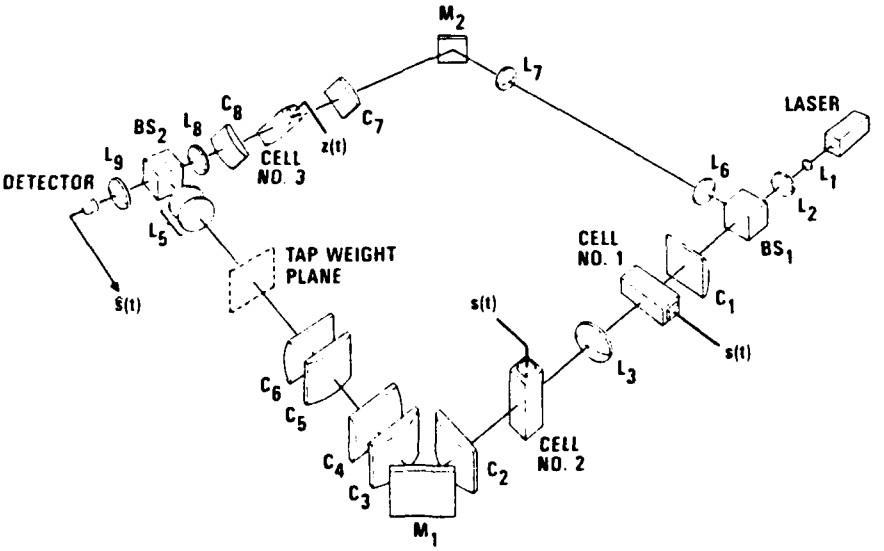

Figure 2. System schematics

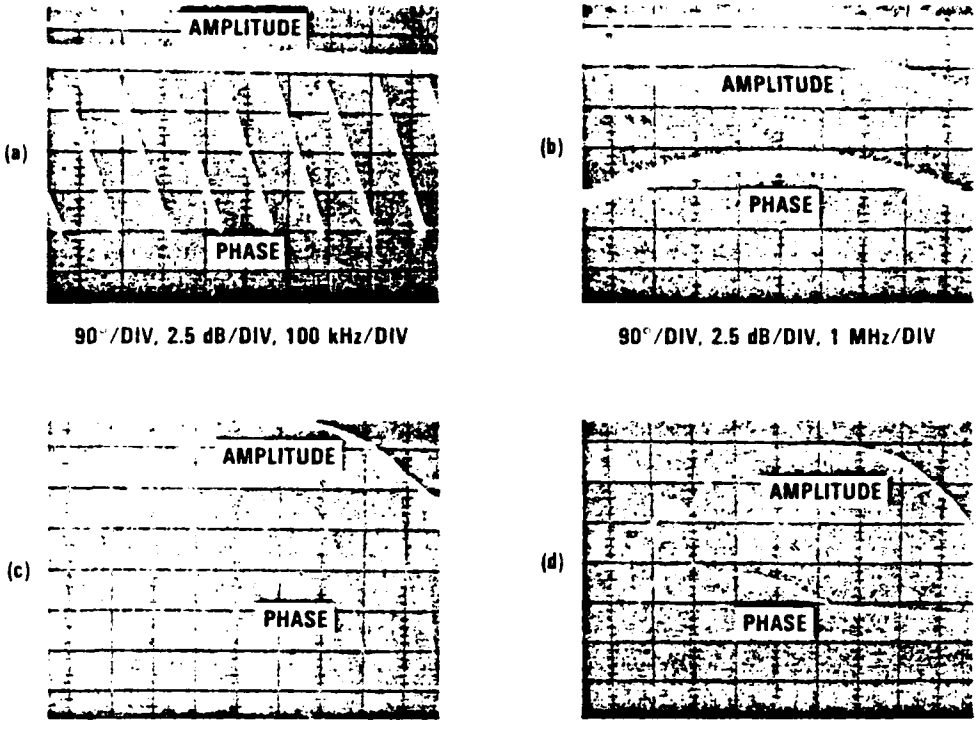

Figure 3. Network analyzer traces for system alignment

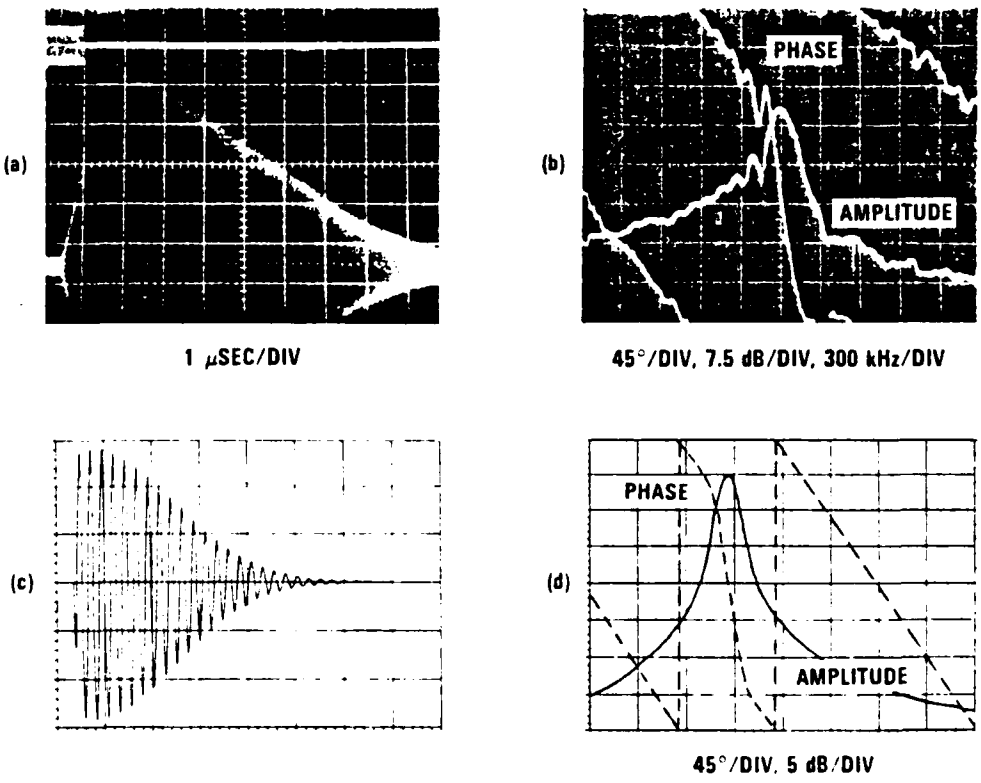

Figure 4. System response for a 5 percent time delay

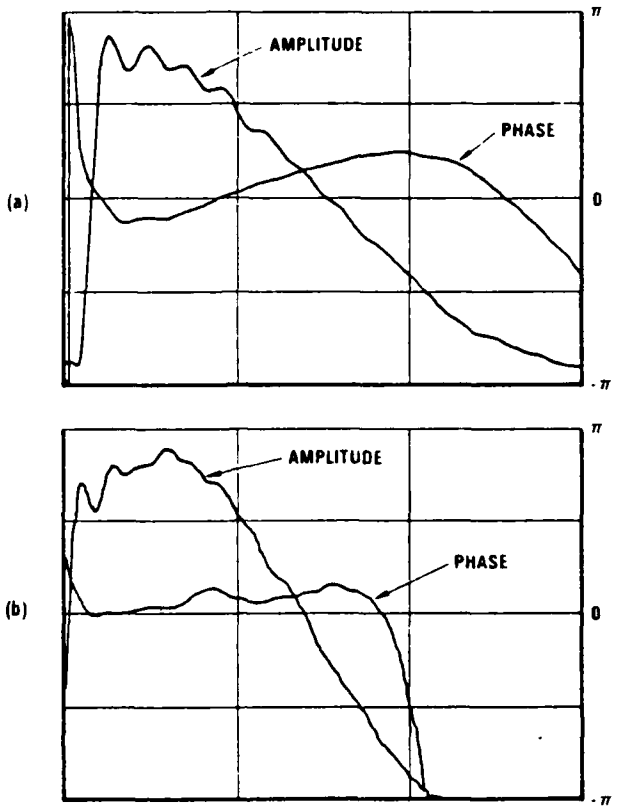

Figure 5. Inverse transform of the measured frequency response

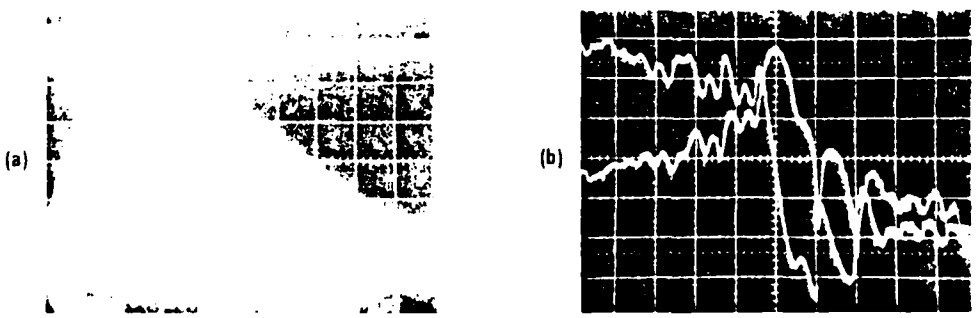

1 μSEC/DIV

45°/DIV, 10 dB/DIV, 300 kHz/DIV

Figure 6. Improved system response with reduced time delay

APPENDIX E

SPATIAL AND TEMPORAL SPECTRA OF PERIODIC FUNCTIONS FOR SPECTRUM ANALYSIS

REPRINTED FROM APPLIED OPTICS

VOLUME 23, PAGE 4269, DECEMBER 1, 1984

Reprinted from Applied Optics, Vol. 23, page 4269, December 1, 1984

Spatial and temporal spectra of periodic functions for spectrum analysis

A. VanderLugt and A. M. Bardos

Both the spatial and the temporal spectra of reference signals used in interferometric spectrum analyzers affect the system performance. We define a class of bandlimited reference signals that have N discrete frequency components of equal magnitude. We show that the system performance is primarily determined by the aperture weighting function and is much less dependent on the specific signal waveform. The aperture weighting function can be used to match the spectral shape to the photodetector size, which then optimizes the dynamic range. Further, since the spatial aperture weighting is converted to an equivalent temporal weighting, this function can also be used to control spurious temporal modulation products. The analysis is extended to include results for periodic chirp signals such as those produced by VCO or SAW devices and shows that the results are not affected by using a reduced duty cycle. We also find that the effect of using finite as opposed to point photodetectors is to introduce an additional factor to the aperture weighting function. Control of both the spatial and temporal modulation products introduced by the periodic reference is necessary to achieve the expected dynamic range.

I. Introduction

In a previous paper we described an approach to interferometric spectrum analysis that provides a significant increase in the dynamic range.[1] The system uses two Bragg cells in an interferometric arrangement. The signal to be analyzed is fed to one Bragg cell to provide the instantaneous spectrum, while a reference signal is fed to the second Bragg cell to provide a distributed local oscillator at the Fourier transform plane. As a result, a fixed temporal offset frequency is generated at each photodetector position. This fixed frequency offset permits a narrowband postdetection filter to separate the signal term from the bias terms at the output. Since this signal term contains the amplitude components of the spectrum, the dynamic range expressed in decibels is nearly doubled compared with that of a power spectrum analyzer. Other advantages of the interferometric approach are improved short pulse detectability and immunity to scattered light.

Analytical and experimental investigations show that the reference waveform has a significant impact on the system dynamic range by being the prime source of spurious modulation. In this paper we give a brief review of the operation of the interferometric spectrum analyzer. We analyze the spatial and temporal characteristics of a generalized reference waveform which can represent signals such as an impulse train, chirp waveforms, pseudorandom sequences, and white Gaussian noise. We then show that, by selecting the appropriate apodization and aperture conditions for the reference beam, spurious modulation can be made vanishingly small. Experimental results that confirm these analyses are given in Ref. 2.

The authors are with Harris Government Systems Sector, P.O. Box 37, Melbourne, Florida 32902.

Received 7 July 1984.
0003-6935/84/234269-11$02.00/0.

II. Background

The basic operation of the interferometric spectrum analyzer can be explained with the aid of Fig. 1. The signal $f(t)$ drives a Bragg cell in the lower leg of the Mach-Zehnder interferometer. The instantaneous spectrum is

$$F_T(p,t) = \int_0^L f(t - x/v) \exp(jpx)\,dx, \tag{1}$$

where L is the length of the Bragg cell, v is the acoustic velocity, p is the radian spatial frequency, and $T = L/v$. A reference signal $r(t)$ drives a Bragg cell located in the upper leg of the interferometer. Its instantaneous Fourier transform $R_T(p,t)$ also occurs at plane P_2, where it is combined with $F_T(p,t)$. Before being combined, however, one of the two spectra are geometrically shifted in the p direction to generate the fixed offset frequency f_d.

The intensity at the Fourier plane is the square of the sum of the amplitudes produced by the signal and reference functions:

$$\begin{aligned} I(p,t) &= |F(p,t)|^2 + |R(p,t)|^2 \\ &\quad + 2|F(p,t)||R(p,t)|\cos[2\pi f_d t + \phi(p)], \\ &= I_1(p,t) + I_2(p,t) + I_3(p,t), \end{aligned} \tag{2}$$

where we have dropped the subscript T; we shall assume that all time signals are truncated by the finite lengths

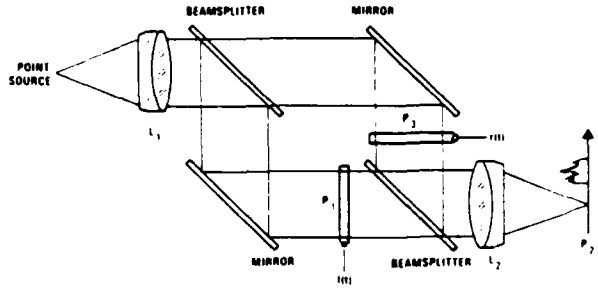

Fig. 1. Interferometric spectrum analyzer.

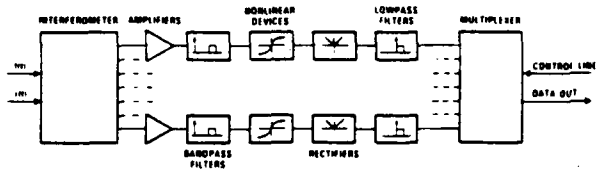

Fig. 2. Block diagram of the postdetection electronics.

of the Bragg cells. This result shows that the intensity function contains two bias terms, which we denote by $I_1(p,t)$ and $I_2(p,t)$, that have temporal frequency components centered at baseband. The third term $I_3(p,t)$, is the spectral cross product of the signal and reference waveforms that, by virtue of the geometric shift, has been offset to frequency f_d. This term can be separated from the bias terms if, for each photodetector output, we use a narrowband filter that passes only those temporal frequency components close to f_d. The phase $\phi(p)$ is the difference between of the phases of $F(p,t)$ and $R(p,t)$.

To model and test the performance of the system we need to consider several other elements of the system. Figure 2 shows the interferometer with its input signals $f(t)$ and $r(t)$. The output of the optical system consists of individual temporal signals produced by discrete photodetectors. These signals are amplified and passed through a narrowband filter centered at f_d. A nonlinear device compresses the range of amplitudes to facilitate rectification and to display the wide dynamic range of the signal. The outputs from the rectifiers are then low-pass filtered and fed to a multiplexer so that the frequency components can be polled to satisfy operational needs.

III. Mixed Transform Concept

The operation of any spectrum analyzer is basically determined by the spatial Fourier transform of the time signal that flows through the Bragg cell. In a power spectrum analyzer, the spatial transform of the signal is sufficient to fully describe the behavior of the system. To obtain better dynamic range, however, the interferometric spectrum analyzer produces a temporal signal that is subjected to further processing to extract the information. Test equipments such as an electronic spectrum analyzer are useful tools to assess the performance of the system at various test points. It is important, therefore, to examine the temporal spectrum of the signals as well as the spatial spectrum to accurately interpret the results and to indicate how we can improve the performance of the system. We call the spatial/temporal Fourier transform the mixed transform because, when displayed as a 2-D function, the independent variables represent spatial and temporal frequencies.

From Eq. (2) it is clear that the reference waveform $R(p,t)$ plays an important role in the performance of the system. The desired characteristics are that (1) the magnitude should be nearly equal at all photodetector sites, (2) the spatial and temporal frequencies should be coupled so that, with a relative geometric displacement between the reference waveform and the signal spectrum, equal temporal offset frequencies are produced at all photodetector locations, (3) the amplitude should not be a function of time, and (4) the duty cycle of the drive signal must be high so that the light is efficiently used.

In Ref. 1 we showed that, for a given bandpass filter shape, the number of photodetectors N is 2.5 times the desired number of resolvable frequencies in the received signal. The reference signal must, therefore, contain at least N frequency components. Let $r(t)$ denote a signal generated by summing N frequencies produced by equal amplitude, sinusoidal oscillators of phases ϕ_n. The resulting reference signal can then be represented by

$$r(t) = \sum_{n=N_1}^{N_2} \cos(2\pi n f_0 t - \phi_n), \tag{3}$$

where $f_1 = N_1 f_0$ and $f_2 = N_2 f_0$ are the lowest and highest frequencies in the signal; this representation is used because Bragg cells are bandpass devices. The value of f_0, the frequency difference between adjacent oscillators, is chosen so that there is one photodetector for each oscillator in the Fourier plane of the spectrum analyzer.

Since $r(t)$ contains N discrete frequencies, each a harmonic of the basic frequency f_0, it must also be a repetitive signal with repetition period $T_r = 1/f_0$. We can generate a surprising variety of waveforms by specifying the phases appropriately. For example, if we choose the ϕ_n to be equal to zero, $r(t)$ is an impulse train[3]:

$$r(t) = \cos[(N_1 + N_2)\pi f_0 t] \left[\frac{\sin(N\pi f_0 t)}{\sin(\pi f_0 t)}\right].$$

If we choose the ϕ_n to be a linear function of n (e.g., $\phi_n = n\phi_0$), the impulse train is advanced or delayed according to the sign and magnitude of ϕ_0. If the phases are quadratic in n so that

$$\phi_n = -\frac{d\pi n^2}{Nf_0}, \tag{4}$$

$r(t)$ is a repetitive chirp function whose period is T_r, whose duty cycle is d, and whose frequency range is from f_1 to f_2.

An interesting example of the behavior of $r(t)$, which

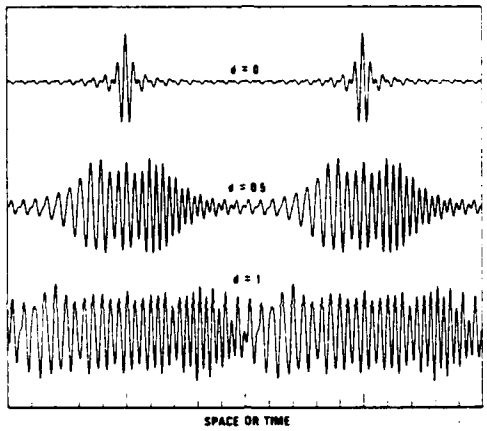

Fig. 3. Chirp function with duty cycles of zero, one-half, and one.

shows the transition from an impulse train to a chirp train, is given in Fig. 3. The upper trace shows two periods of $r(t)$ when the phase is zero for all n. The middle trace is that for a quadratic phase function according to Eq. (4), but with $d = \frac{1}{2}$; we note that the repetitive chirp function now has a duty cycle of 50%. The lower trace shows the chirp function when $d = 1$; the chirp now has a 100% duty cycle. Thus we find a smooth progression from an impulse train to a full duty cycle chirp as d is changed from 0 to 1. In all three cases we translated $r(t)$ to a center frequency which shows how the reference signal will look when it drives the Bragg cell. The center frequency in this case is three times the highest frequency of the baseband signal. We also normalized each waveform to reflect the fact that the Bragg cell diffraction efficiency is constrained to a value less than one. Each of these signals is a suitable reference signal; the choice tends to be with a high duty cycle chirp so that the light power is efficiently used.

Other useful reference waveforms can be generated by a proper choice of the phases. A repetitive pseudorandom sequence of length $N = 2^r - 1$, where r is an integer, can be produced if the phases for the various frequencies are suitably chosen.[4] If the ϕ_n are random, the resulting signal simulates a bandlimited noise source that, nevertheless, retains a repetitive feature.

The Bragg cell presents the drive signal $r(t)$ to the illuminating reference beam and to the subsequent optics for Fourier transformation in the form of index of refraction waves propagating at the acoustic velocity. The amplitude profile of the illuminating beam, the acoustic attenuation, the size limitations of the cell, and any other weighting factors combine to form a multiplicative aperture weighting function $a(x)$. These features of the interaction can be expressed in the form $a(x)r(t - x/v)$. Bragg selectivity and the finite apertures of the optical configuration will allow only the positive or negative spatial frequency terms to propagate. Thus we shall replace each cosine by the downshifted temporal and spatial frequency terms and omit the complex conjugate terms; the optical reference input function is then defined as

$$r(x,t) = a(x) \sum_{n=N_1}^{N_2} \exp[-j2\pi n f_0(t - x/v) + j\phi_n] \tag{5}$$

We now calculate the mixed transform of $r(x,t)$, which is defined as

$$\mathbf{R}(\alpha,\beta) = \int_{-\infty}^{\infty} \int_{-\infty}^{\infty} r(x,t) \exp[j2\pi(\alpha x - \beta t)]\,dx\,dt, \tag{6}$$

where we now use α to denote a spatial frequency and β to denote a temporal frequency. Throughout the analyses that follow, we drop all scaling factors and unimportant phase factors. It is advantageous to calculate the spatial transform first; we do so by using Eq. (5) in Eq. (6) to get

$$R(\alpha,t) = \int_{-\infty}^{\infty} a(x) \sum_{n=N_1}^{N_2} \exp[-j2\pi n f_0(t - x/v) + j\phi_n] \times \exp(j2\pi\alpha x)\,dx. \tag{7}$$

By separating the time and space dependent terms and by performing the integration over space, we find that

$$R(\alpha,t) = \sum_n A(\alpha + nf_0/v) \exp(-j2\pi n f_0 t + j\phi_n), \tag{8}$$

where $A(\alpha)$ is the Fourier transform of the aperture weighting function $a(x)$. To illustrate more clearly some of the features of $R(\alpha,t)$, we let $a(x) = \mathrm{rect}(x/L)$ so that Eq. (8) becomes

$$R(\alpha,t) = \sum_n \mathrm{sinc}[L(\alpha + nf_0/v)] \exp(-j2\pi n f_0 t + j\phi_n). \tag{9}$$

We see that the reference signal in the Fourier plane consists of a set of sinc functions, sometimes referred to as beads, that are centered at each of the N photodetector positions. Each bead has an associated pure frequency that is a harmonic of f_0. We now examine the relationship of the length L of the Bragg cell to that of the repetition period $L_r = vT_r$. If $L \gg L_r$, the Bragg cell contains many periods of the reference signal. The beads then become very narrow relative to their spacings; these beads are centered at $\alpha = -nf_0/v = -n/vT_r = -n/L_r$. This condition is useful when the photodetector spatial duty cycle is small because the available light is then concentrated onto the detectors. However, the reference beam Bragg cell, whose bandwidth is equal to the signal analysis bandwidth, must then have a very large time-bandwidth product to handle several periods of the reference signal.

Although it may be impractical to use several periods of the reference signal, it is worthwhile to consider the use of a smaller number as a means to shape the spatial frequency amplitudes to better match the size of the photodetectors. As noted before, the photodetectors spacing must be equal to $1/L_r$, and we let h denote the spatial duty cycle. It is easy to show that the SNR and dynamic range are maximized when the duty cycle is equal to one. It can also be shown that, if $h \leq 1$, the dynamic range is maximized when $hL = 1.37L_r$ under the assumption that the Bragg cell is uniformly illuminated. In general, the aperture weighting function $a(x)$ will cause further spreading in the Fourier plane, so that L will need to be increased somewhat to achieve opti-

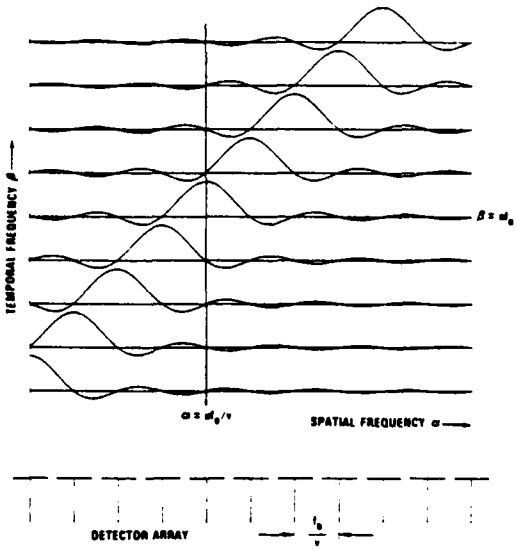

Fig. 4. Magnitude of the mixed transform for an arbitrary signal and uniform illumination.

mum performance. We return to the subject of aperture weighting in a later section.

We now complete the mixed transform by calculating the temporal frequency content. We have that

$$\mathbf{R}(\alpha,\beta) = \int_{-\infty}^{\infty} R(\alpha,t)\exp(-j2\pi\beta t)dt. \tag{10}$$

We substitute Eq. (8) into Eq. (10) to find that

$$\mathbf{R}(\alpha,\beta) = \sum_n \exp(j\phi_n)A(\alpha + nf_0/v)\delta(\beta + nf_0). \tag{11}$$

This relationship can also be written in an equivalent form as

$$\mathbf{R}(\alpha,\beta) = A(\alpha - \beta/v)\sum_n \exp(j\phi_n)\delta(\beta + nf_0). \tag{12}$$

We see that $\mathbf{R}(\alpha,\beta)$ consists of a two-dimensionally coupled skew function that is sampled by a set of phase weighted delta functions creating N discrete terms, or beads. There is one bead at each photodetector position, shifted by the desired frequency nf_0 and distance nf_0/v, with a shape described by $A(\alpha)$. Due to the nature of the sampled skew function, we find that the magnitude of the mixed transform is independent of the specific repetitive reference signal $r(t)$.

To more clearly visualize this conclusion, we note from Eq. (12) that a set of delta functions sample the function $A(\alpha - \beta/v)$ in the temporal frequency domain. Figure 4 shows the magnitude of $\mathbf{R}(\alpha,\beta)$ when $a(x) = \text{rect}(x/L)$. For any value n, the spatial frequency response is a sinc function centered at $\alpha = -nf_0/v$. In this mixed transform concept, however, the sinc function is displayed at $\beta = nf_0$ so that, as n increases from N_1 to N_2, we find that the sinc functions occur along a skew line in the α,β plane. This is the 2-D display that we would expect if we were to use the y-axis of a conventional Fourier transforming system to display the time-shifted versions of the reference signal as it passes through the Bragg cell.

We illustrate this concept by showing in Fig. 5 a reference signal that is shifted progressively in time in the vertical direction. For any given spatial position x_0 we find the temporal function by reading the values along a vertical line positioned at x_0. At any given time t_0 we find the spatial function resident within the Bragg cell by reading the values along a horizontal line through t_0. From the 2-D space/time representation shown in Fig. 5, we can also obtain the mixed transform shown in Fig. 4 if the optical aperture of a Fourier transform system is limited to $\pm L/2$ in the space dimension and is infinite in the time dimension.

So far we have examined the characteristics of the reference waveform as it affects the cross-product term in Eq. (2). We now consider the bias term that is due solely to the reference beam. From Eq. (8) we find that the intensity $I_2(\alpha,t)$ is

$$I_2(\alpha,t) = |R(\alpha,t)|^2 = \sum_{n=N_1}^{N_2}\sum_{m=N_1}^{N_2} \exp[-j2\pi(n-m)f_0t] \times \exp[j(\phi_n - \phi_m)]\,A(\alpha + nf_0/v)A^*(\alpha + mf_0/v). \tag{13}$$

The mixed transform for the bias term can be readily obtained by finding the temporal transform of Eq. (13):

$$\mathbf{I}_2(\alpha,\beta) = \sum_n\sum_m \exp[j(\phi_n - \phi_m)]A(\alpha + nf_0/v) \times A^*(\alpha + mf_0/v)\delta[\beta + (n-m)f_0]. \tag{14}$$

The conclusion that we reach from Eq. (14) is that the bias term, in general, contributes energy at all integer multiples of f_0. There is a special set of conditions, however, for which $\mathbf{I}_2(\alpha,\beta)$ has energy only at $\beta = 0$. This set of conditions is that $a(x) = \text{rect}(x/L)$, that L is equal to some integer multiple of L_r, and that point photodetectors are placed at integer multiples of f_0/v. In this special case we find that the sums in Eqs. (13) and (14) can be performed for $n = m$, and the result is that the power spectrum of $r(x,t)$ is constant in time and at all photodetector positions.

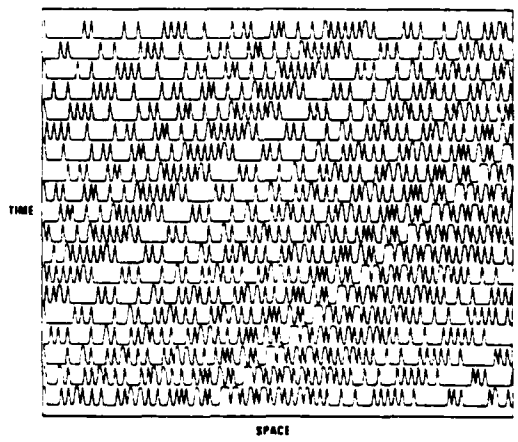

Fig. 5. Reference signal envelope expressed as a function of space and time.

The mixed transform concept and the generalized repetitive signal function as given by Eq. (3) have illustrated the importance of the reference beam aperture weighting $a(x)$ and the truncation positions. We have also shown that the mixed transform of such a repetitive signal is independent of the specific signal waveform. We now use these concepts to study in some detail how they apply to a specific hardware implementation that uses a chirp signal generated by a voltage-controlled oscillator. We develop additional analytic tools for handling some special chirp functions and their transforms. We further explore how the aperture weighting function and finite photodetectors affect the basic results.

IV. Cross-Product Term for a Chirp Reference Beam

Repetitive chirp signals can be obtained from voltage-controlled oscillators (VCO) or from surface acoustic wave (SAW) devices. We generally require that the device produce a waveform that linearly sweeps the frequency over a range of several hundred megahertz centered at the midband of the frequency response of the Bragg cell. The sweep period is generally in the microsecond range for wideband spectrum analysis.

Although the mathematics in this section are somewhat cumbersome, much can be learned from a detailed analysis of the process. We derive an approximate solution which can be used as a powerful intuitive and analytical tool for understanding the nature of the interferometric architecture using chirped reference functions. These detailed results can then be related to the experimental results and are useful in other studies as well. We define a chirp signal as

$$p(t) = \cos(gt^2/2), \tag{15}$$

where we will not, for the moment, bound the chirp signal in time; as a result, we see that all temporal frequencies are generated. We define the sweep rate as $g = 2\pi W/T_p$, where $W = f_2 - f_1$ is the useful bandwidth of the Bragg cell, and T_p is the time required to sweep from f_1 to f_2. We can now define the repetitive reference signal $r(t)$ as

$$r(t) = p(t) * \sum_{n=-\infty}^{\infty} \delta(t - nT_r) = \sum_n p(t - nT_r),$$

where $*$ denotes convolution, and we retain the notation that T_r is the repetition period. Following the procedure used in Sec. III, we can represent the signal resident in the Bragg cell by $a(x)r(t - x/v)$ and retain only the negative spatial frequencies:

$$r(x,t) = \sum_n a(x) \exp[-jg(t - nT_r - x/v)^2/2]. \tag{16}$$

We can now relate $r(x,t)$ to the repetitive chirp signal produced by a physical device such as a VCO that is driven by a repetitive ramp waveform. Since the Bragg cell and the photodetector array process only those frequencies from f_1 to f_2, the results will be equivalent to those that would be obtained if we were to view $r(x,t)$ as a bandlimited function consisting of a train of chirp pulses with duration T_p and a repetition period T_r. In the physical implementation, it is important to realize

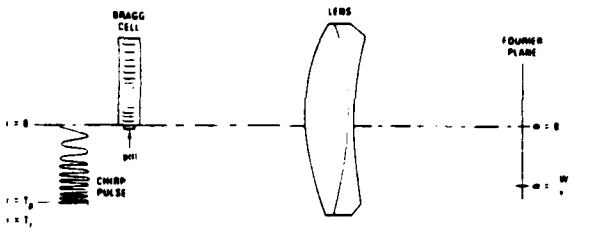

Fig. 6. Fourier transform arrangement for an isolated chirp pulse.

that the starting phase of each successive pulse may not be the same. Suppose that the phase has advanced by ϕ_c at the end of the repetition period. Since this phase carries over to the start of the next pulse, we find that Eq. (16) must be modified by a multiplicative factor $\exp(jn\phi_c)$ to accurately represent the chirp train:

$$r(x,t) = \sum_n a(x) \exp -j[g(t - nT_r - x/v)^2/2 - n\phi_c]. \tag{17}$$

The reference signal is therefore not, strickly speaking, a repetitive signal in the sense that it contains only harmonics of f_0. We shall show later how this phase term influences our results.

We can find the mixed transform of $r(x,t)$ in one of several ways. A particularly simple way is to first obtain the transform for $p(t)$ and arrive at the final result through a multiplication by the Fourier transform of the sampling function. Consider the reference leg of the interferometer as shown unfolded in Fig. 6. The representation of the chirp pulse will be described in two different ways to connect the mathematical formalism with a physically realizable situation. As a mathematical function represented by Eq. (15), we can think of $p(t)$ as extending over all time (i.e., not bounded in the vertical direction). The condition shown, then, is one in which the useful frequency range from f_1 to f_2 is just about to enter the Bragg cell. At a time T_p seconds later, the last useful frequency enters the Bragg cell, and all others can be ignored. As a physically realizable function, the pulse representation satisfies the description given before, wherein the VCO has just been activated by the voltage ramp. At time T_p the blanking circuit is turned on, and at time T_r a new pulse is initiated.

We now calculate the spatial Fourier transform of $r(x,t)$ as given by Eq. (17) with $n = 0$; we then account for the summation over all n. We have for the central pulse that

$$P(\alpha,t) = \int_0^L \exp[-j(g/2)(t - x/v)^2] \exp(j2\pi\alpha x)dx. \tag{18}$$

To simplify the analysis, we have ignored the carrier frequency that translates $p(t)$ into the passband of the Bragg cell as well as the aperture weighting function $a(x)$. We complete the square in x to find that

$$P(\alpha,t) = \exp[jg(vt + 2\pi\alpha v^2/g)^2/2v^2] \exp[-j(g/2)t^2]$$
$$\times \int_0^L \exp[-jg[x - (vt + 2\pi\alpha v^2/g)]^2/2v^2]dx \tag{19}$$

We can put this integral into the standard form of a Fresnel integral to obtain

$$P(\alpha,t) = \exp[j(2\pi\alpha vt] \int_b^c \exp[-j(\pi/2)z^2]dz,$$

where

$$b = \sqrt{g/\pi v^2}[-vt - 2\pi\alpha v^2/g],$$
$$c = \sqrt{g/\pi v^2}[L - vt - 2\pi\alpha v^2/g]. \quad (20)$$

We now examine the important properties of the Fresnel integral for our application. One way to represent the integral is by using the Cornu spiral.[5] The arc length along the spiral is given by the difference between the upper and lower limits:

$$c - b = \sqrt{g/\pi}L/v. \quad (21)$$

By recognizing that $L/v = T$ is the time duration of the Bragg cell, and by using the relationship that $g = 2\pi W/T_p$, we find that the arc length is equal to $\sqrt{2WT^2/T_p}$. Since the arc length is greater than the square root of the time-bandwidth product of the Bragg cell, which is typically of the order of several hundred, the arc length is of the order of 10–20. As a result, the Fresnel integral has a nearly constant value, except when the upper and lower limits are equal to zero. At these points, the Fresnel integral makes a rapid transition through its half-amplitude values so that the limits tell us when the shadow regions for each edge occur as a function of the spatial frequency.

From the limits in Eq. (20), we note that each spatial frequency α receives light starting at $t = -\alpha v T_p/W$ and ending T seconds later (recall that α is always negative). Although there are ripples associated with the leading and trailing edges of the Fresnel integral function, we can approximate the value of the integral by $\text{rect}(t/T - \frac{1}{2} - \alpha v T_p/WT)$ to obtain some useful results. The spatial transform then becomes

$$P(\alpha,t) = \text{rect}(t/T - \tfrac{1}{2} + \alpha v T_p/WT)\exp(j2\pi\alpha vt). \quad (22)$$

From Eq. (22) we see that, at a particular value of α, the first factor indicates the time duration when the light is on, and the second factor gives the associated temporal frequency. We now take care of the summation; by using Eqs. (22) and (17), we find that the spatial transform of the repetitive chirp signal is

$$R(\alpha,t) = \exp(j2\pi\alpha vt)\sum_n \text{rect}(t/T - nT_r/T - \tfrac{1}{2} + \alpha v T_p/WT)$$
$$\times \exp(-j2\pi\alpha v n T_r)\exp(jn\phi_c). \quad (23)$$

The mixed transform $\mathbf{R}(\alpha,\beta)$ of the reference waveform can now be obtained by substituting Eq. (23) into Eq. (10):

$$\mathbf{R}(\alpha,\beta) = \text{sinc}|T(\alpha v - \beta)|\sum_n \delta(\beta + nf_0 - \phi_c f_0/2\pi). \quad (24)$$

When we compare Eq. (24) with Eq. (12), we see that, if $\phi_c = 0$, the results are similar even though they were obtained by quite different methods. Here we have a skewed sinc function in α and β which is sampled by a set of delta functions in β. This result shows that a phase-incremented repetitive chirp function generated by an analog circuit such as a VCO device contains N discrete frequencies both spatially and temporally. The phase increment ϕ_c, however, will shift the frequency sampling delta functions from integer harmonics nf_0 to a fractional offset position $(n + \phi_c/2\pi)f_0$. In the spatial frequency domain this means that, while their spacings remain the same, the bead center locations will shift.

The method of analysis given here is equivalent to our having used a more general model for the periodic signal, in which

$$r(t) = \sum_{n=-\infty}^{\infty} \cos[2\pi(n + \phi_c/2\pi)f_0 - \phi_n],$$

which accounts for ϕ_c as well as for allowing all frequencies to be present in the drive signal.

We now calculate the Fourier transform from the signal beam leg of the interferometer. Consider a cw signal $s(t)$ that has a single frequency f_s and a Fourier transform arrangement as shown in Fig. 6. Let $b(x)$ represent the signal beam aperture function combining all apodization and truncation effects, and let a linear phase ramp express the geometric offset of the signal spectrum. The optical signal input function is then given as

$$s(x,t) = b(x)\exp[-j2\pi f_s(t - x/v)]\exp(j2\pi\alpha_d x).$$

At the detector plane the signal is represented by

$$S(\alpha,t) = \int_{-\infty}^{\infty} s(x,t)\exp(j2\pi\alpha x)dx$$
$$= B(\alpha + \alpha_d + f_s/v)\exp(-j2\pi f_s t),$$

where $B(\alpha)$ is the spatial Fourier transform of $b(x)$. For a rectangular aperture function we find that

$$S(\alpha,t) = \text{sinc}|(\alpha + \alpha_d + \alpha_s)L_s|\exp(-j2\pi f_s t), \quad (25)$$

where $\alpha_s = f_s/v$, and α_d is the geometric offset in spatial frequency needed to produce the temporal carrier frequency in Eq. (2).

The product of the signal and reference term is $I_3(\alpha,t) = 2\,\text{Re}[R(\alpha,t)S^*(\alpha,t)]$; this term produces the signal that we observe at a test point located just after the bandpass filter. For a high dynamic range system such as this interferometric spectrum analyzer, it is often useful to display a signal that is proportional to $I_3(\alpha,t)$ on a conventional time spectrum analyzer. We therefore want to find the mixed transform $\mathbf{I}_3(\alpha,\beta)$ through the temporal transform

$$\mathbf{I}_3(\alpha,\beta) = \int_{-\infty}^{\infty} I_3(\alpha,t)\exp(-j2\pi\beta t)dt \quad (26)$$

By using Eqs. (23) and (25) in Eq. (26), we find that

$$\mathbf{I}_3(\alpha,\beta) = \text{sinc}|(\alpha + \alpha_d + \alpha_s)L_s|$$
$$\times \text{sinc}|(\alpha v - \beta_s + f_s)T|\sum_n \delta(\beta + f_s - \phi_c f_0/2\pi + nf_0). \quad (27)$$

This result reveals that $\mathbf{I}_3(\alpha,\beta)$ has its maximum value when a photodetector is positioned so that $\alpha = -(\alpha_d + \alpha_s)$ because the spatial sinc function then has its max-

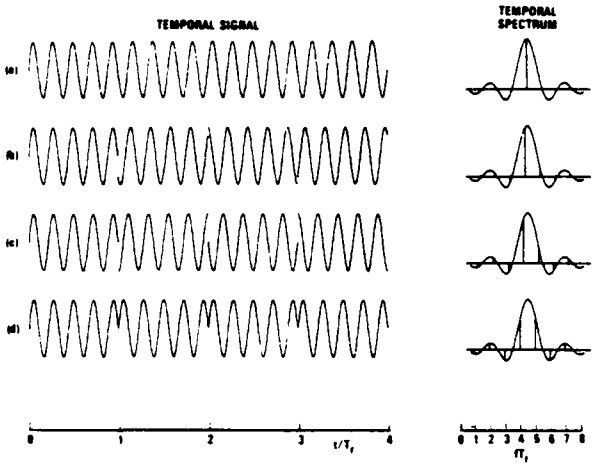

Fig. 7. Temporal and temporal frequency signal representations as a function of the phase increment.

imum value. Although the signal frequency α_s is unknown and must be estimated, the photodetector spacing was chosen to be f_0/v so that at least one photodetector in the array will be near the peak of the spatial sinc function.[1] We find that the time-domain spectrum at the optimum detector location is

$$\mathbf{I}_3(\beta) = \operatorname{sinc}[(\beta + f_d)T] \sum_n \delta(\beta + f_s - \phi_c f_0/2\pi + nf_0). \quad (28)$$

We now illustrate the results of our analysis for the cross-product term which, after bandpass filtering, is the desired output. We shall consider both the form of $I_3(t)$, which is the temporal signal displayed on an oscilloscope, and the form of $\mathbf{I}_3(\beta)$, which is the signal displayed on a temporal spectrum analyzer for a given photodetector element. In both cases, the phase increment for each pulse given by $\exp(jn\phi_c)$ will affect the results.

In Fig. 7(a), we show the form of $I_3(t)$ for four periods of the repetitive chirp waveform when $\phi_c = 0$. The output, as expected, consists of a pure cosine whose amplitude is proportional to that of the CW signal at f_s. The cosine is continuous, without any change in phase over all time, independently of the duty cycle of the chirp. We also show in Fig. 7(a) the value of $\mathbf{I}_3(\beta)$, which is a sinc function centered at $\beta = -f_d$ with the first nulls at $\pm 1/T$ from the center as given by Eq. (28). The sampling function has value when

$$\beta = f_s - \phi_c f_0/2\pi + nf_0, \quad (29)$$

so that the sampling function is a set of delta functions spaced at intervals in frequency of f_0. Suppose that Eq. (29) is satisfied so that one of the samples falls at $\beta = -f_d$. Then, if $T = T_r$, we find that all the other samples fall at the nulls of $\operatorname{sinc}[(\beta + f_d)T_r]$.

In Figs. 7(b)–7(d) we show the corresponding results when the phase increment between pulses is $\pi/4$, $\pi/2$, and π. We now note that there is a discontinuity in $I_3(t)$ at the beginning and end of each repetition period T_r. The corresponding sketches of $\mathbf{I}_3(\beta)$ show that the sampling function as given by Eq. (28) has shifted underneath the fixed $\operatorname{sinc}[(\beta + f_d)T]$ envelope in such a way that, when the phase increment is equal to π, the sinc function is sampled symmetrically; the corresponding time function shows a phase reversal at the ends of the repetition period.

At this point we can draw an interesting analogy between the behavior of an echelon and the result produced by a repetitive chirp as given by Eq. (28). We recall from Eq. (17) that each pulse in the chirp train is modified by a phase factor that is fixed for the duration of the pulse. These phase increments can be related to those of an echelon wherein the phases between successive steps change by a fixed amount.[6] The situation shown in Fig. 7(a) is equivalent to the single-order position for an echelon. We note from Eq. (28) that there is room for only two samples in the central lobe of the envelope of $\mathbf{I}_3(\beta)$. If the phase increment is adjusted so that $\phi_c = \pi$, the samples are shifted as shown in Fig. 7(d); this situation is called the symmetric position which produces two equal amplitude outputs. In a transmission echelon one can change from the single-order to the symmetrical position by rotating the echelon. In our interferometric spectrum analyzer, one can change positions by changing ϕ_c. In both cases, the sampling delta functions move, but the envelope does not.

From the relationship of the sampling function to the envelope as shown in Fig. 7, we conclude that the temporal output may contain frequency components other than f_d if the phase increment induced by the VCO is not a multiple of 2π. The worst-case condition is that shown in Fig. 7(d); the two components within the main lobe of the sinc function are then just at the band edges of the bandpass filter. It is therefore desirable to control the phase of the chirp generator so that the detectors can be located at the reference bead centers to obtain the condition shown in Fig. 7(a).

V. Bias Terms for a Chirp Reference Beam

It is possible for the reference beam bias term to contribute energy at frequencies within the bandpass filter. We now consider the origin of this unwanted energy and methods for eliminating it. The suppression of these spurious modulation terms is a key design objective in any hardware implementation of this architecture.

The bias term for the chirp reference beam is, from Eq. (2), given by $I_2(\alpha,t) = |R(\alpha,t)|^2$. From Eq. (23) we find that the mixed transform, using the same approximation for the Fresnel integral, is

$$\mathbf{I}_2(\alpha,\beta) = \sum_n \sum_m \exp[j2\pi\alpha v(n-m)T_r] \exp[j(n-m)\phi_c] \times \int_{-\infty}^{\infty} \operatorname{rect}(u_n) \operatorname{rect}(u_m) \exp(-j2\pi\beta t)\,dt, \quad (30)$$

where u_n and u_m, the arguments of the rect functions, are taken from Eq. (23) with the corresponding indices n and m. The integral can be evaluated by a change of variables wherein we let

$$u = u_n = t/T - nT_r/T - \tfrac{1}{2} + \alpha v T_p/WT$$

so that the integral becomes

$$\exp(-j2\pi\beta nT_r) \int_{-\infty}^{\infty} \text{rect}(u)\, \text{rect}[u + (n-m)T_r/T] \times \exp(-j2\pi\beta Tu)\, du \quad (31)$$

The first rect function has value only for $|u| \le \frac{1}{2}$. The second rect function determines how many terms for the summation on m are important. We see that if the time duration of the Bragg cell T is equal to the repetition period T_r, the only terms of interest are those for $n = m$ because otherwise the two rect functions do not overlap, and the integral is zero. In this special case the integral reduces to $\text{sinc}(\beta T_r)$, and we find that

$$I_2(\alpha,\beta) = \text{sinc}(\beta T_r) \sum_n \delta(\beta - \alpha v - \phi_c f_0/2\pi + nf_0). \quad (32)$$

The magnitude of $I_2(\alpha,\beta)$ is clearly a function of ϕ_c. A physical interpretation of the effect of the phase increment is that the spectrum from the reference beam has shifted by a fraction $\phi_c/2\pi$ of the photodetector spacing. If the photodetector array is moved to restore the condition that each element is centered under a bead, the delta function in Eq. (32) reduces to $\delta(\beta - nf_0)$, and we find that all the sampling functions are at the nulls of the sinc function. It is only under these special conditions that $I_2(\alpha,\beta)$ has no content at any temporal frequency other than at $\beta = 0$.

The results obtained in this section are based on the approximation that the Fresnel integral can be approximated by a rect function. In addition, we have ignored the aperture function $a(x)$ which plays an important role in determining the form of $I_2(\beta)$. In effect, the spatial aperture weighting is converted to a temporal weighting; this can be seen by noting that each frequency component of the chirp travels underneath the aperture function $a(x)$. In the appendix we derive the exact results that remove the approximation and include the effects of the aperture function. In particular, we find that the temporal frequency content of the reference beam bias term can be represented by a function $G(\beta)$ that is sampled at the frequencies $\beta = nf_0$. In general, $G(\beta)$ will have a set of nulls, but they may not fall at integer multiples of f_0.

If we do not take action to keep $I_2(\beta)$ small in the bandpass of the filter, we find that the SNR and, therefore, the dynamic range are less than expected. Even if f_d is fairly large so that the energy in the bandpass filter arises from distant sidelobes of $G(\beta)$, the energy in this bias term may be significant relative to that of the cross-product term for low signal levels. We now examine ways to control the in-band magnitude of the reference bias term, which we call spurious modulation, through appropriate aperture weighting. We note, in passing, that the signal beam bias term as given by $|S(\alpha,t)|^2$ leads to a pure frequency at $\beta = 0$ and, therefore, need not concern us further.

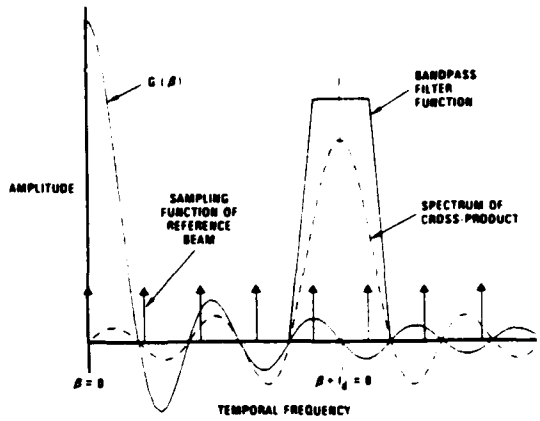

Fig. 8. Temporal frequency content of cross-product and reference beam bias terms.

VI. Aperture Weighting Function

As a preliminary to a study of the aperture function, we show the magnitudes of $I_2(\beta)$ and $I_3(\beta)$ in Fig. 8, along with the photodetector bandpass filter response. In this illustration, $G(\beta)$ is the transform of a truncated Gaussian illumination function. The bandpass filter shape is approximated by a trapezoid which is constant for $\beta = -f_d \pm f_0/2$ and falls to zero at $\beta = -f_d \pm f_0$; this shape is required to keep the photodetector response to nearly signal frequencies under control.[1]

The most critical sampling function is that associated with the bias term. These samples start at $\beta = 0$ and are placed at integer multiples of f_0. In this example, we see that the samples at $n = 4$ and $n = 5$ are at local maxima of $G(\beta)$, so that a significant amount of spurious modulation is within the passband of the filter. The relative magnitude of the spurious modulation can be seen by applying the output signal from the bandpass filter to a conventional spectrum analyzer, with the signal set at zero amplitude. As the chirp period T_r is varied, the sample functions move within the envelope of the bandpass filter, and the relative magnitudes of the sampled frequencies will vary according to the shape of $G(\beta)$ provided the Bragg cell aperture is not changed. Alternatively, we can see the spurious modulation change if the aperture L is changed while the repetition rate T_r is fixed.

For the case of $a(x) = \text{rect}(x/L)$, it is possible to eliminate the bias term by adjusting the spatial truncation and the repetition rate so that the sampling functions fall exactly at the nulls of $G(\beta)$. In practice this is difficult to do for several reasons. The acoustic wave within the Bragg cell is attenuated as it propagates through the cell, and it experiences acoustic spreading as well. The effects of other apertures in the illumination beam may introduce small ripples in the illumination. Although the asymmetry induced by acoustic attenuation can be compensated by a spatial shift in the Gaussian illumination, the combination of these factors may still produce an asymmetric and, in general, an inaccurately known weighting function.

Another source of aperture weighting is introduced by the finite sizes of the photodetectors. One way to determine the effects of finite photodetectors is to integrate $I_3(\alpha,\beta)$ as given by Eq. (27) over the appropriate range on α. An interesting alternative, and one that leads to a somewhat more general result, is to recognize that the results for a finite detector can be derived from those obtained from point detectors through a convolution operation. The convolution involves only the size of the detector if its sensitivity is uniform over its surface. We can then replace the convolution operation in the detector plane by a multiplication operation in the input plane, where the multiplication function $d(x)$ is the Fourier transform of the detector aperture. For example, if the photodetector aperture has an extent of h/L_r, where h is the duty cycle, we have that $d(x) = \text{sinc}(hx/L_r)$. If we invoke the relationship that $hL = 1.37L_r$ to maximize the dynamic range, we find that $d(x)$ has its maximum value at $x = 0$ and drops to sinc(0.685) at the edges of the aperture. Since $d(x)$ applies to both the signal and the reference beam Bragg cells, and since $L_s < L_r$, we find that the contribution of $d(x)$ to the signal beam weighting function $b(x)$ is less than that to the reference beam weighting function $a(x)$.

An illustration of how the total aperture weighting function influences the shape of $G(\beta)$ is shown in Fig. 9. For comparison purposes we show $G(\beta)$ for $a(x) = \text{rect}(x/L)$ as curve A. When we use a symmetric Gaussian illumination for which the intensity is $1/e^2$ at the truncation points, we have the response shown in curve B. We note that the Gaussian illumination broadens the central lobe and that the maximum sidelobe levels are significantly lower. We also note that the first few nulls are irregularly spaced and that, even for the higher orders, the nulls do not occur at the same positions as those of the sinc function. Curve C shows the shape of $G(\beta)$ for the same Gaussian illumination but with its center displaced by 6% of the aperture width. We now note that the nulls are not as deep, although the amount of induced asymmetry is small. Finally, curve D shows the Gaussian illumination displaced by 12% of the aperture width. The overall sidelobe level is higher than with curves B and C, and the nulls are even less well formed. We note here that symmetric functions produce real-valued transforms so that perfect nulls are generated between positive and negative sidelobes. Asymmetric functions produce complex-valued transforms and, in general, less well-formed nulls between local maxima.

This example shows that attempts to place the sample functions at the nulls of $G(\beta)$ will be difficult to control, and for the case of asymmetric illumination, the resulting spurious modulation may be higher than desired. A second way to reduce the effects of the bias term is to increase the offset frequency f_d so that we encounter the higher-order sidelobes of $G(\beta)$. But since the illumination is generally sharply truncated, the sidelobe level does not roll off rapidly as a function of frequency. Furthermore, a high value for f_d has an adverse effect on the photodetector performance since

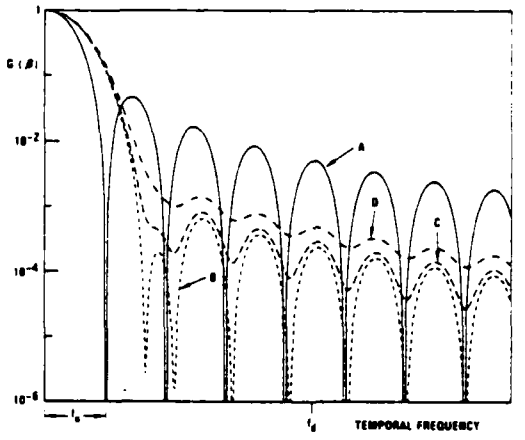

Fig. 9. The temporal spectral envelope of the reference beam bias term for various aperture weighting functions.

it must now respond to much higher temporal frequencies. Another possibility is to use a weighting function so that $G(\beta)$ rolls off more rapidly than those functions shown in Fig. 9. For example, if $a(x)$ is a sinc function, $G(\beta)$ falls to zero within the bandpass. However, the sinc function must also be truncated at some point; if it is truncated at the fifth sidelobe, $G(\beta)$ is no more than 50 dB down in the passband. Furthermore, the Bragg cell must be five times its nominal length for us to use this type of illumination.

The best overall solution is to require that f_d be a harmonic of f_0, which would place just one sample exactly at the midband of the bandpass filter. We would then be faced with a much simpler task of requiring that only one null of $G(\beta)$, suitably deep, coincide with f_d. A truncated Gaussian illumination such as the one that produced curve B from Fig. 9 would be acceptable. Even though the exact form of $G(\beta)$ may not be known due to implementation uncertainties, a slight change in the truncation points at the Bragg cell should be sufficient to bring one of the nulls of $G(\beta)$ to the offset frequency position. Some care is needed to ensure that the combined aperture effects are not too asymmetric so that sufficiently deep nulls are achieved. The required depth of the null is quite large because we want the bias term to be well below the magnitude of the cross-product term. If the system has a design goal of a 60-dB dynamic range, the null must be of the order of 65–70 dB since the bias term is generally somewhat stronger than the cross-product term.

We note that the signal beam aperture weighting function $b(x)$ plays no role in our efforts to control the bias term. It can, in principle, be chosen independently of $a(x)$ to satisfy other system requirements such as controlling cross-talk levels.

VII. Summary and Conclusions

We have analyzed the role that a repetitive reference beam has on the performance of an interferometric spectrum analyzer. We defined a class of bandlimited

signals that have N discrete frequency components of equal amplitude but arbitrary phases. We have shown that the mixed transform is a useful concept for obtaining a joint spatial and temporal transform of the output of the system. Based on this mixed transform, we showed that the performance of the system is not dependent on the specific repetitive waveform since the distributed local oscillator function in the Fourier plane is identical for all such functions.

We also showed that the reference beam aperture function plays a critical role in the performance of the system. Since the spatial aperture weighting function is converted to an equivalent temporal weighting, this function can be used to control spurious modulation arising from the reference beam bias term. When the spurious modulation is controlled, the expected dynamic range is achieved.

We showed that all the results predicted by the generalized analysis also hold for implementation schemes wherein a VCO device is used to generate a repetitive chirp waveform. We found that the duty cycle of the chirp has no influence on the results, but that a phase increment from pulse to pulse may influence the output if the bandwidth of the postdetection filter is not set properly and the detectors are not located at the bead centers. We also determined that the use of finite-sized photodetectors do not seriously affect the results other than to impart some additional weighting to the aperture function. Experimental results confirm the analysis given here.

This work was supported in part by the U.S. Army Research Office.

Appendix

We derive an exact solution for the mixed transforms $\mathbf{I}_2(\alpha,\beta)$ and $\mathbf{I}_3(\alpha,\beta)$ for the chirp waveform produced by a VCO. In the text we produced the intermediate results as given by $I_2(\alpha,t)$ and $I_3(\alpha,t)$ so that the spatial Fourier transform could be characterized explicitly as a function of time. We did so by first performing the spatial transform, followed by a temporal transform.

Here we will reverse the order of integration and obtain the temporal transform first. We use Eq. (17) as our point of departure, but write it in the time convolutional form

$$r(x,t) = a(x)\exp[-jg(t - x/v)^2/2] * \sum_{n=-\infty}^{\infty} \exp(jn\phi_c)\delta(t - nT_r). \tag{33}$$

We first treat the mixed transform of the cross-product term $\mathbf{I}_3(\alpha,\beta)$:

$$\mathbf{I}_3(\alpha,\beta) = \int_{-\infty}^{\infty}\left\{\left[\int_{-\infty}^{\infty} r(x,t)\exp(j2\pi\alpha x)dx\right]S^*(\alpha,t)\right\} \times \exp(-j2\beta t)dt \tag{34}$$

We recognize the term within the braces as $I_3(\alpha,t)$. We use the result for $S^*(\alpha,t)$ as given by Eq. (25) and rearrange the terms to get

$$\mathbf{I}_3(\alpha,\beta) = \int_{-\infty}^{\infty} a(x)\,\mathrm{sinc}[(\alpha + \alpha_d + \alpha_s)L_s] \times \int_{-\infty}^{\infty}\left\{\exp[-jg(t - x/v)^2/2] * \sum_n \exp(jn\phi_c)\delta(t - nTr)\right\} \times \exp[-j2\pi(\beta - f_s)t]\exp(j2\pi\alpha x)dtdx. \tag{35}$$

We recognize that the integral over time is the Fourier transform of the convolution of two functions, so that the result is the product of the transform of the two functions. The first transform is

$$\int_{-\infty}^{\infty}\exp[-jg(t - x/v)^2/2]\exp[-j2\pi(\beta - f_s)t]dt.$$

This integral is similar to that given by Eq. (18), except that we now integrate over infinite limits. The result of the integration is[7]

$$\sqrt{\pi/g}\exp(-j\pi/4)\exp[-j2\pi(\beta - f_s)x/v + j2\pi^2(\beta - f_s)^2/g]. \tag{36}$$

The second transform is

$$\int_{-\infty}^{\infty}\sum_n \exp(jn\phi_c)\delta(t - nTr)\exp[-j2\pi(\beta - f_s)t]dt = \sum_n \delta(\beta - f_s - \phi_c f_0/2\pi + nf_0). \tag{37}$$

We now substitute the results given in Eqs. (36) and (37) into Eq. (35) to obtain, after dropping the scaling terms,

$$\mathbf{I}_3(\alpha,\beta) = \mathrm{sinc}[(\alpha + \alpha_d + \alpha_s)L_s]\sum_n \delta(\beta - f_s - \phi_c f_0/2\pi + nf_0) \times \int_{-\infty}^{\infty} a(x)\exp[j2\pi\alpha x - j2\pi(\beta - f_s)x/v]dx. \tag{38}$$

The remaining integral is easily evaluated to get the result that

$$\mathbf{I}_3(\alpha,\beta) = \mathrm{sinc}[(\alpha + \alpha_d + \alpha_s)L_s] + A(\alpha - \beta/v + f_s/v)\sum_n \delta(\beta - f_s - \phi_c f_0/2\pi + nf_0). \tag{39}$$

When we compare this result with Eq. (27), we see that it is indeed appropriate to replace the sinc function by the Fourier transform of the aperture weighting function as we did in the text. This result, which is an exact solution, substantiates the validity of the approximation.

The mixed transform of the reference bias term is given by

$$\mathbf{I}_2(\alpha,\beta) = \int_{-\infty}^{\infty}|R(\alpha,t)|^2\exp(-j2\pi\beta t)dt,$$

which can also be expressed as a convolution in β:

$$\mathbf{I}_2(\alpha,\beta) = \mathbf{R}(\alpha,\beta) * \mathbf{R}^*(\alpha,-\beta). \tag{40}$$

By a line of analysis similar to that used above, we find that

$$\mathbf{R}(\alpha,\beta) = \exp(j2\pi^2\beta^2/g)A(\alpha - \beta/v)\sum_n \delta(\beta - \phi_c f_0/2\pi + nf_0). \tag{41}$$

and we obtain $\mathbf{I}_2(\alpha,\beta)$ by using Eq. (41) in Eq. (40).

References

1. A. VanderLugt, "Interferometric Spectrum Analyzer," Appl. Opt. **20**, 2770 (1981).
2. L. M. Ralston and A. M. Bardos, "Wideband Interferometric Spectrum Analyzer Improvement," Final Report AFWAL-TR-84-1029, AFWAL/AADO, WPAFB, Ohio 45433.
3. I. S. Ghadshteyn and I. M. Ryzhik, *Tables of Integrals, Series and Products* (Academic, New York, 1965), p. 30.
4. S. W. Golomb, *Shift Register Sequences* (Holden-Day, San Francisco, 1967), p. 86.
5. D. H. Towne, *Wave Phenomena* (Addison-Wesley, Reading, Mass., 1967), p. 295.
6. R. S. Longhurst, *Geometrical and Physical Optics* (Longmans, Green and Co., London, 1967), pp. 253–258.
7. Ref. 3, p. 304.

APPENDIX F

FRESNEL TRANSFORMS AND BRAGG CELL PROCESSORS

REPRINTED FROM APPLIED OPTICS

VOLUME 24, PAGE 3846, NOVEMBER 15, 1985

Fresnel transforms and Bragg cell processors

A. VanderLugt

In the analysis of coherently illuminated optical systems we distinguish between space planes and spatial frequency or Fourier planes. Between these two planes exists a continuum of Fresnel transform planes; the Fresnel domain therefore shares, more or less equally according to its position, the properties of the space and frequency domains. Since Fresnel transforms are space-variant operations, generalized results are difficult to obtain. When implemented by Bragg cell processors, however, Fresnel transforms have some interesting and useful spatial/temporal properties. We examine the application of Fresnel transforms to analog signal scrambling techniques. We derive the optimum geometry for obtaining the maximum time spreading for a given signal bandwidth. We derive the system response to impulse, short pulse, and cw signals. We show how a permutation of time samples can be achieved and illustrate some of the key features through simulations.

I. Introduction

Fresnel transforms arise naturally in optics for relating the complex-valued light distribution between two planes separated by free space. They are used to illustrate the basic nature of holography[1,2] in which the Fresnel transform of an object is recorded for subsequent reconstruction. In these cases we generally do not evaluate the Fresnel transform explicitly; rather, we use their properties to understand, at an intuitive level, the structure of light patterns produced by the object. Fresnel transforms are also used in synthetic aperture radar processing[3,4]; in this case, the explicit form of scattering by point objects is used to determine the appropriate range and azimuth processing operations.

Fresnel transforms are not used extensively in real-time signal processing applications because the response in the Fresnel plane is dependent on the input signal position and frequency. As a result, operations such as matched filtering can be implemented only by scanning methods. In this paper, however, we exploit the time-variant and frequency-variant properties of Fresnel transforms to scramble wideband signals, in real time, to obtain privacy in a communication system.

Until 1979, when Wyner described a scrambling technique for analog signals,[5] relatively little work had been reported on analog privacy techniques. Scrambling is most often implemented in the time domain by sampling, digitizing, and encoding the analog signal; this process generally requires that the transmission channel have a wider bandwidth than the signal itself. Scrambling can also be implemented in the frequency domain by splitting the signal spectrum into several frequency bands and rearranging them before transmission. Two or more techniques are sometimes combined to provide higher levels of privacy, as suggested in a review of the early work on scrambling.[6] In a more recent collection of papers,[7] scrambling schemes are described that use an intermediate storage device so that discrete samples can be transmitted using time permutation schemes.

A communication system consists of a transmitter, a channel, and a receiver. The transmitter accepts the signal to be sent, scrambles it to provide privacy, and prepares it for transmission over the channel. We want to conserve channel bandwidth, in general, consistent with the degree of privacy required. The purpose of the receiver is to unscramble the transmitted waveform and to recover the original message. Increased privacy can be achieved at the cost of bandwidth expansion; even more sophisticated techniques are required to achieve encryption of analog signals.[7]

For wideband signals such as TV, the application of classical techniques becomes more difficult because high speed A–D converters with high precision are needed, and the resulting bandwidth expansion may be considerable. A direct method of scrambling wideband analog signals with little or no bandwidth expansion is therefore desirable. In this paper we examine the possibility for scrambling analog signals both with and without bandwidth expansion, using certain prop-

The author is with Harris Corporation, Government Systems Sector, Advanced Technology Department, P.O. Box 37, Melbourne, Florida 32901.

Received 20 May 1985.
0003-6935/85/223846-11$02.00/0.

erties of Fresnel transforms. The Fresnel transform analysis developed here provides considerable insight into the basic scrambling scheme and suggests other optical processing applications. For background information, we cite the pioneering work of Whitman *et al.*[8] involving Bragg diffraction and optical heterodyning techniques. Other interesting techniques, using Fourier analyses, are those given by Korpel *et al.*,[9] by Rhodes and Florence,[10] and by Florence.[11] In Sec. II we present the basic system concepts in terms of geometric and heuristic arguments; the more rigorous diffraction analysis given in Sec. IV, after we give a brief review of the properties of Fresnel transforms and integrals in Sec. III. In Sec. V we give the results of some simulations that illustrate the concepts and provide some additional results.

II. System Description and Geometric Representation

The system shown in Fig. 1 contains a Bragg cell in plane P_1, driven by a signal $s(t)$. For generality, we let $s(t)$ be a real-valued bandpass signal with bandwidth W centered at frequency f_c. The illumination is collimated light at the Bragg angle Θ_B, where $\Theta_B = \arcsin(\lambda/2\Lambda_c)$, λ is the wavelength of light, and Λ_c is the acoustic wavelength associated with f_c. Since $\Lambda_c = v/f_c$, where v is the acoustic velocity, we have that $\theta_B \approx \lambda f_c/2v$. The chief ray of the undiffracted beam therefore intercepts plane P_2 at $\eta_c = \Theta_B D = \lambda D f_c/2v$, where D is the distance between planes P_1 and P_2; the spatial coordinates in planes P_1 and P_2 are x and η. In a similar fashion, the chief ray of the diffracted light intercepts plane P_2 at $-\eta_c$. An aperture weighting function $a(x)$ accounts for the amplitude variations in the illuminating beam, attenuation effects induced by the Bragg cell, and limiting apertures caused by the Bragg cell or other optical elements. Since we are operating in the downshifted Bragg mode, we retain only the negative frequencies associated with the signal. The signal produced by the Bragg cell can then be represented by

$$f(t,x) = a(x)\exp(-j2\pi x\Theta_B/\lambda)s(t - T/2 - x/v), \qquad (1)$$

where the exponential function represents the Bragg angle illumination and $T/2$ is the time delay associated with one-half of the Bragg cell length. This diffracted signal now propagates through free space a distance D to plane P_2. The free space operator produces a Fresnel transform as given by

$$g(t,\eta) = \int_{-\infty}^{\infty} f(t,x)\exp[-j(\pi/\lambda D)(x-\eta)^2]dx, \qquad (2)$$

where the exponential function represents the free space response to an impulse. This definition of the Fresnel transform varies slightly from others in the literature (see, for example, Ref. 12). The difference is primarily in the point of emphasis; I prefer the form given here because it (1) explicitly displays the impulse response of free space, (2) shows the convolutional process between the free space operator and the input signal, (3) produces a continuous transition from the Fresnel to the Fraunhofer transform as a function of the distance D between the input and output planes, and (4) retains the necessary phase factors to facilitate the analysis of optical systems that use additional lenses and free space intervals to achieve other processing operations.[13] Throughout this analysis we ignore scaling factors and nonessential phase terms. We retain, however, phase terms that are functions of time or space because they indicate the temporal or spatial frequency variations of the light distributions.

We can detect the complex-valued function $g(t,\eta)$ if we provide a coherent reference function $R(\eta)$ for purposes of heterodyne detection. We use a lens to image a point source from plane P_0 to the point $-\eta_c$ in plane P_2. The reference beam is aperture weighted by $r(x)$ in plane P_1 to shape $R(\eta)$ as desired. A photodetector integrates the intensity produced by the sum of $R(\eta)$ and $g(t,\eta)$ over all η; the size of the photodetector is not important, provided that it captures nearly all the light in $R(\eta)$. Since the reference beam is not frequency shifted, the output signal from the photodetector also has bandwidth W centered at f_c; this signal is sent over some communication channel to a receiver. The receiver is a conjugate form of the transmitter; that is, the receiver layout is essentially the same as that shown in Fig. 1, except that the Bragg cell is driven from the opposite end. The output of the receiver, as we shall show later, is a delayed version of the desired signal $s(t)$.

Before continuing with the diffraction analysis, we present some of the basic scrambling concepts by using geometric and heuristic arguments. These results are useful for interpreting those obtained from the diffraction theory analysis in Sec. IV. To simplify this analysis, we would like to characterize the Fresnel diffraction as though it propagates along the optical axis, instead of at the angle θ_B as shown in Fig. 1. We also wish to retain the notion that $s(t)$ contains single sideband frequencies from $f_c - W/2$ to $f_c + W/2$. We can achieve both objectives by translating the origin of plane P_2 a distance η_c; the jusification for the use of this temporary construct will become clear as the description unfolds.

In Fig. 2, then, we show the Bragg cell of length L and transit time $T = L/v$. Although the Bragg cell should be shown tilted with respect to the optical axis, the

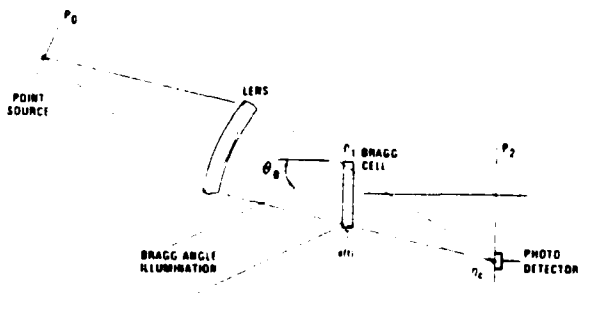

Fig. 1. Basic system geometry: transmitter.

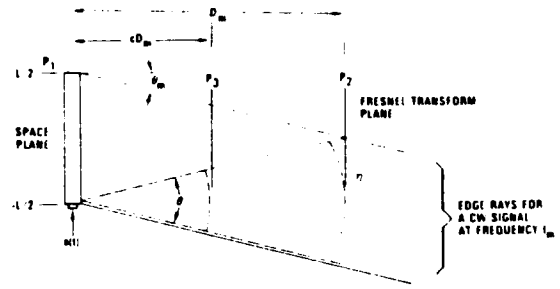

Fig. 2. Geometrical representation of the Fresnel transforms of a cw signal and a bandlimited impulse function.

geometric results are not affected by its position as shown. When $s(t)$ is a cw frequency at f_c, the light travels from plane P_1 to plane P_2 as a plane wave parallel to the optical axis; the chief ray therefore intercepts plane P_2 at $\eta = 0$. A cw frequency at the maximum frequency $f_m = f_c + W/2$ will propagate as a plane wave at the angle $\theta_m = \arcsin(W\lambda/2v) \approx W\lambda/2v$. The edge ray of this bundle intercepts the optical axis at a distance D_m:

$$D_m = Lv/\lambda W. \tag{3}$$

In a similar fashion, the opposite edge ray from a frequency $f_c - W/2$ will also intercept the optical axis a distance D_m from plane P_1. If the distance between planes P_1 and P_2 is greater than D_m, the higher frequencies in the band W cannot be detected at the point $\eta = 0$. On the other hand, a decrease in this distance is acceptable because light from all cw frequency components in $s(t)$ will then reach the photodetector. Since $L = vT$, we can derive an important relationship connecting the physical parameters of the optical system with the key parameters of the signal:

$$\frac{v^2}{\lambda D_m} = \frac{W}{T}. \tag{4}$$

An alternative form of Eq. (4) is that $L^2/\lambda D_m = WT$; this relationship is also valid for stationary spatial signals and connects the dimensions of the Fresnel transform system to the time–bandwidth product of the signal. Both forms of Eq. (4) state that the system is just capable of processing the information when $D = D_m$; if the distance between planes P_1 and P_2 is less than D_m, the system has excess capacity, whereas if the distance is greater than D_m, the system has insufficient capacity.

Next, consider the system response to an impulse function. A true impulse function will produce a cylindrical wave propagating into free space at all angles. But since the input signal is bandlimited, the shortest pulse that the system can support will generate rays confined to the range of angles $|\theta| \leq \theta_m$. The marginal rays for such an impulse function that has just entered the Bragg cell are shown by dotted lines in Fig. 2. Since the instantaneous frequency at plane P_2 is proportional to the slope of the cylindrical wave, the transmitter produces a chirp function, spanning the frequency range W, as the impulse moves through the cell. If $D = D_m$, the photodetector receives light as soon as the impulse enters the Bragg cell and continues to receive light until the impulse leaves the Bragg cell; we conclude that the impulse is spread or dispersed into a chirp signal of duration T. If the distance between planes P_1 and P_2 exceeds D_m, there is no increase in the time spreading of the impulse. The maximum distance between planes P_1 and P_2 is therefore the value that satisfies Eq. (4); this ensures that no frequencies are missed and provides for maximum time spreading.

Other scrambling techniques become available if we place the photodetector in a plane for which $D < D_m$. Figure 2 also shows plane P_3, which is a distance cD_m from plane P_1, where $0 \leq c \leq 1$. Although the response to a cw signal is not a function of the value of c, the response to an impulse is such that a photodetector placed at $\eta = 0$ does not receive light at $t = 0$ when $c < 1$. From straightforward geometrical considerations, we find that the chirp now arrives at $t_1 = (1 - c)T/2$ and that the chirp duration is $T_p = cT$. Therefore, as c ranges from zero to one, the delay in the onset of the chirp response ranges from $T/2$ to zero. The instantaneous frequency always spans the range W so that the channel bandwidth is not affected by which Fresnel plane is selected. What does change is the chirp rate; it now becomes $W/T_p = W/cT$. As we shall see later, this increase in chirp rate is exactly that required to make the receiver operate properly.

Suppose that the point of observation is now changed to some position $\eta \neq 0$ in plane P_3. The time-of-arrival t_d of the chirp response to an impulse occurring at $t = 0$ is now given by

$$t_d = t_1 + \eta/v = (1 - c)T/2 + \eta/v, \tag{5}$$

so that it is possible to obtain additional time delays through a choice of η. If η is too large, however, the photodetector will miss some of the light from cw signals. The constraint on η is that

$$|\eta| \leq (1 - c)L/2, \tag{6}$$

so that the range of available time delays is $0 \leq t_d \leq (1 - c)T$. Equation (6) defines a cone that intercepts plane P_1 at $x = \pm L/2$ and whose apex is at $\eta = 0$ in plane P_2; the photodetector must be placed within this cone to satisfy all the constraints.

A third type of envelope function that produces some interesting results is a short pulse of duration T_0. Such a pulse will behave as an impulse function when $T_0 \ll T$ and as a cw signal whenever T_0 approaches or exceeds T. Consider a pulse whose duration is of the order of $T/8$ as shown in Fig. 3 and let the observation point be at $\eta = 0$ in plane P_2. Further, suppose that this pulse contains frequency components at f_1, f_2, and f_3 such that $f_1 < f_2 < f_3$. The photodetector receives energy at time intervals related to the frequency content of the pulse. If we think of the pulse as a musical chord, we find that the time difference t_n between the first two notes is given by $t_n = (\eta_1 - \eta_2)v$, where $\eta_1 - \eta_2$ is the distance between the leading edges of the pulses

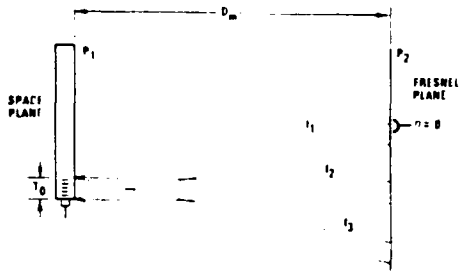

Fig. 3. Geometrical representation of the Fresnel transform of a multitone short pulse.

in plane F_2. By using the basic rules of diffraction theory, we find that

$$t_n = (\eta_1 - \eta_2)/v = (f_1 - f_2)\lambda D_m/v^2, \tag{7}$$

which, through the use of Eq. (4), can be reduced to

$$t_n = (f_1 - f_2)T/W. \tag{8}$$

Thus, we see that a chord is encoded as a succession of pure tones, each of duration T_0. In the sense of this analogy, the transmitter arpeggiates the chord. At any other Fresnel plane for which $D < D_m$, we have that $t_n = (f_1 - f_2)cT/W$. Therefore, as c tends toward zero, the time difference between successive tones also tends toward zero and the chord appears simultaneously at the photodetector. Different time delays prior to the onset of the first tone can be obtained, as discussed before, if $c < 1$ or if the photodetector is displaced from the optical axes, subject to the constraints of Eqs. (5) and (6).

A signal $s(t)$ may contain impulses, pulses of various frequencies and durations, and cw compounds. It is clear from these arguments that the response from a pulse at frequency f_1 may occur before that of a previous pulse of frequency f_2, if $f_1 < f_2$. Similarly, an impulse that trails a short pulse may produce an output before the photodetector receives light from the short pulse. As a result, the transmitted signal is scrambled according to both the time structure and the temporal frequency structure of $s(t)$.

For some signals the parameters W and T may be such that D_m is an inconveniently large distance. In this case, we can place a lens of focal length F at plane P_1 to bring the chosen Fresnel transform plane to a convenient distance. The developments given above, as well as those to follow, are still valid, provided that we replace D by $DF/(F - D)$, where D is the distance from the lens to the Fresnel plane. If the focal length is chosen so that the Fourier plane has the same spatial extent as the space plane, the capacity of the optical system is maximized.[14] The maximum distance that the Fresnel plane can be from the lens and still satisfy the constraints given is $D_m = F/2$. Thus, the Fresnel transform shares, more or less equally, the characteristics of a space function and its Fourier transform. Since there is a continuum of Fresnel transform planes between the space plane and the Fourier plane, we can choose the one that best suits our purposes.

These discussions, based on ray traces, show how the basic scrambling phenomena occur. We return to them in Sec. IV, using a more rigorous diffraction theory analysis. First, we provide a brief review of some basic properties of the Fresnel integral used to evaluate certain Fresnel transforms.

III. Fresnel Transform

The Fresnel transform that we need to evaluate is given by Eq. (2). Through a change of variables, we obtain the standard form of the transform which can be expressed as

$$g(t,\eta) = \int_{-\infty}^{\infty} f(t,\eta,z)\exp[-j(\pi/2)z^2]dz, \tag{9}$$

where t, η, and z are real-valued parameters. Here t and η represent the temporal and spatial variables of the transformation, and z is a normalized variable of integration. Based on the discussions in Sec. II, we want to evaluate $g(t,\eta)$ for signals such as impulse functions, short pulses, or cw waveforms. The spatial limitations imposed by the Bragg cell or by the signal itself will often allow us to express $f(t,\eta,z)$ in the form of a rectangular function so that the Fresnel transform reduces to the generalized complex form of the Fresnel integral:

$$g(t,\eta) = \int_{z_1}^{z_2} \exp[-j(\pi/2)z^2]dz, \tag{10}$$

where $z_1 = a(t,\eta)$ and $z_2 = b(t,\eta)$ define the end points of the rect function. Although the Fresnel integral cannot be expressed in closed form in terms of elementary functions, we can summarize some of its features. We see that the integrand is oscillatory, so that we expect $g(t,\eta)$ to be oscillatory for some values of t and η. The integrand oscillates most slowly at $z = 0$ so that the integral then has its largest value, provided that $z = 0$ lies within the range of integration.

One way to understand the Fresnel integral in a qualitative sense is through the use of the Cornu spiral.[15] The parameters z_1 and z_2 represent points on the Cornu spiral, and $z_{12} = z_2 - z_1$ is a measure along the arc of the spiral. When $z_2 = \infty$ and $z_1 = -\infty$, the value of the integral is $\sqrt{2}$. If we keep z_2 fixed and allow z_1 to increase, $g(t,\eta)$ begins to oscillate with gradually increasing amplitudes about a mean of $\sqrt{2}$. As z_1 passes through zero, $g(t,\eta)$ decreases rapidly, reaches its half-amplitude value at $z_1 = 0$, and continues to decay toward zero as z_1 proceeds toward z_2.

This general behavior can be used to explain the response to the short pulse illustrated in Fig. 3. Consider the ray bundle for the pulse at frequency f_2; when the pulse has just entered the Bragg cell, both z_1 and z_2 have large negative values so that light reaching a photodetector at $\eta = 0$ has a small amplitude. As the pulse moves through the system, both z_1 and z_2 increase in value, with z_{12} remaining constant. The physical meaning of z_2 and z_1 is that they represent the normalized distance, in plane P_1, from the optical axis to the leading and trailing edges of the pulse. When z_2

= 0, the leading edge of the pulse causes the photodetector response to increase rapidly as the transition from the geometric shadow region to the fully illuminated region occurs. As the pulse continues to move through the Bragg cell, the amplitude oscillates as the internal fringes pass by the photodetector. When $z_1 = 0$, the amplitude decreases rapidly as the transition into the shadow region occurs.

The key information regarding the behavior of Fresnel integral, then, are the limits of integration since they characterize the transitions into and out of the shadow regions. When z_{12} is large, the contributions to the Fresnel integral from the pulse edges are nearly independent and the distance between the half-amplitude points is the same as the pulse width. But if z_{12} is small, so that the pulse is very narrow, the contributions from the two edges interfere; the Fresnel integral then produces a Fraunhofer pattern at the detector plane. For z_{12} smaller still, the Fraunhofer pattern spreads over larger distances in plane P_2; it is this pattern that produces the chirp response to an impulse function.

IV. Diffraction Representation

We now support, by diffraction theory analyses, the conclusions from Sec. II based on goemetrical considerations. A detailed picture of how the transmitter and receiver operate will emerge from this analysis and additional results will be obtained. We proceed by using the basic setup shown in Fig. 1; the signal produced by the Bragg cell $f(t,x)$ and its Fresnel transform $g(t,\eta)$ are given by Eqs. (1) and (2). As noted before, a reference function $R(\eta)$ is added to $g(t,\eta)$ to facilitate heterodyne detection. From Fig. 1 we see that the reference function is provided by a point source in plane P_0 that is imaged by a lens at the point $\eta = -\eta_c$ in plane P_2. We express $R(\eta)$ as the Fresnel integral of a wave front crossing plane P_1:

$$R(\eta) = \int_{-\infty}^{\infty} r(x) \exp[j(\pi/\lambda D)x^2] \times \exp(j2\pi x\eta_c/\lambda D) \exp[-j(\pi/\lambda D)(x-\eta)^2]dx, \quad (11)$$

where $r(x)$ is the aperture weighting function for the reference beam, the first exponential is the equivalent lens function at plane P_1, and the second exponential represents the tilt necessary to focus the light at $\eta = -\eta_c$ in plane P_2. We add $R(\eta)$ to $g(t,\eta)$ to obtain the intensity at plane P_2:

$$I(t,\eta) = |R(\eta) + g(t,\eta)|^2 = |R(\eta)|^2 + |g(t,\eta)|^2 + 2\mathrm{Re}|R^*(\eta)g(t,\eta)|. \quad (12)$$

The output voltage from the photodetector can be obtained by integrating $I(t,\eta)$ over the photodetector surface:

$$v(t) = \int_{-\infty}^{\infty} I(t,\eta)d\eta. \quad (13)$$

When we substitute Eq. (12) into Eq. (13), we obtain three signals which we denote by $v_1(t)$, $v_2(t)$, and $v_3(t)$. The first signal is a constant so that its temporal frequency is concentrated at $f = 0$. The second signal has temporal bandwidth W, centered at $f = 0$. The third signal has bandwidth W, is centered at f_c, and can be separated from the first two by a bandpass filter. The desired signal is then

$$v_3(t) = \int_{-\infty}^{\infty} R^*(\eta)g(t,\eta)d\eta + c.c \quad (14)$$

We evaluate one term of Eq. (14) and take the real part of the result at the end of the analysis. We substitute Eqs. (2) and (11) into Eq. (14) to find that

$$v_3(t) = \int_{-\infty}^{\infty}\int_{-\infty}^{\infty}\int_{-\infty}^{\infty} r^*(x)f(t,y) \exp(-j2\pi x\eta_c/\lambda D) \times \exp[-j(\pi/\lambda D)x^2] \times \exp[j(\pi/\lambda D)[(x-\eta)^2 - (y-\eta)^2]]dx\,dy\,d\eta. \quad (15)$$

We integrate first on η, noting that the factors in η^2 cancel; the η-dependent terms yield

$$\int_{-\infty}^{\infty} \exp[-j(2\pi/\lambda D)(x-y)\eta]d\eta = \delta(x-y). \quad (16)$$

We use the sifting property of the delta function to find that the output of the transmitter is

$$v_3(t) = \int_{-\infty}^{\infty} r^*(x)f(t,x) \exp(-j2\pi x\eta_c/\lambda D) \exp[-j(\pi/\lambda D)x^2]dx. \quad (17)$$

Let us now consider the structure of the receiver. The receiver must first convert the temporal signal $v_3(t)$ to a time–space representation through the use of a Bragg cell. The receiver must then produce an inverse Fresnel transform of the diffracted light so that $s(t)$ can be recovered from the output of a photodetector by heterodyne detection. We conclude that the receiver must be a conjugated form of the transmitter. For example, since the transmitter produces a cylindrically diverging wave front from an impulse, the receiver must produce a cylindrically converging wave front to reproduce the impulse. This concept is the temporal equivalent of the spatial concepts used in holography to create and reconstruct wave fronts from 2-D or 3-D objects.[1,2]

The receiver geometry is therefore the same as that shown in Fig. 1, except that the received signal enters from the opposite of the Bragg cell. The acoustic signal propagates with a negative velocity component relative to that of the illumination so that the diffracted beam is upshifted. We again apply the Fresnel transform relationship to find that the light distribution at plane P_2 is

$$h(t,\xi) = \int_{-\infty}^{\infty} b(y)v_3^*(t - T/2 + y/v) \exp(-j2\pi y\theta_B/\lambda) \times \exp[-j(\pi/\lambda D)(y-\xi)^2]dy, \quad (18)$$

where y and ξ are now the coordinates of planes P_1 and P_2, and $b(y)$ is the aperture weighting function for the receiver.

As in the transmitter, we add a reference beam $R(\xi)$ to $h(t,\xi)$ at $-\xi_c$, square-law detect the sum, filter out the baseband terms $v_4(t)$ and $v_5(t)$, and integrate the cross product term over the photodetector surface:

$$v_6(t) = \int_{-\infty}^{\infty} R^*(\xi)h(t,\xi)d\xi. \quad (19)$$

We now use Eqs. (1), (2), (14), and (18) to find that

$$v_6(t) = \int_{-\infty}^{\infty}\int_{-\infty}^{\infty}\int_{-\infty}^{\infty}\int_{-\infty}^{\infty} a^*(x)b(y)R(\eta)R^*(\xi)s(t - T - x/v + y/v) \times \exp[j2\pi\theta_B(x - y)/\lambda] \times \exp\{j(\pi/\lambda D)[(x - \eta)^2 - (y - \xi)^2]\}dx\,dy\,d\eta\,d\xi. \quad (20)$$

We first integrate on η and find that

$$\int_{-\infty}^{\infty} R(\eta)\exp[j(\pi/\lambda D)(x - \eta)^2]d\eta = r(x)\exp(j2\pi x\eta_c/\lambda D) \times \exp[j(\pi/\lambda D)x^2] \quad (21)$$

by virtue of the relationship given in Eq. (11). A similar result applies to the integration on ξ. We combine Eq. (21) with Eq. (20) to obtain

$$v_6(t) = \int_{-\infty}^{\infty}\int_{-\infty}^{\infty} a^*(x)b(y)r(x)r^*(y)s(t - T - x/v + y/v) \times \exp[j2\pi\theta_B(x - y)/\lambda]\exp[j(2\pi/\lambda D)(x\eta_c - y\xi_c)] \times \exp[j(\pi/\lambda D)(x^2 - y^2)]dx\,dy. \quad (22)$$

To match the structure of the transmitter and receiver, we set $\eta_c = \xi_c$ so that Eq. (22) reduces to

$$v_6(t) = \int_{-\infty}^{\infty}\int_{-\infty}^{\infty} a^*(x)b(y)r(x)r^*(y)s^*(t - T - x/v + y/v) \times \exp[j2\pi f_c(x - y)/v]\exp[j(\pi/\lambda D)(x^2 - y^2)]dx\,dy. \quad (23)$$

We change variables through a scaling operation and a rotation of the axes by 45° to arrive at the result that

$$v_6(t) = \int_{-\infty}^{\infty} s(t - T - q)\exp(j2\pi f_c q)m(q)dq, \quad (24)$$

where

$$m(q) = \int_{-\infty}^{\infty} a^*[(\tau + q)v/2]b[(\tau - q)v/2] \times r[(\tau + q)v/2]r^*[(\tau - q)v/2]\exp[-j(\pi v^2/\lambda D)\tau q]d\tau. \quad (25)$$

The aperture functions thus combine to play a dual role in determining the performance of the system. On the one hand, $a(x)$ and $b(y)$ are equivalent to time windows that determine the signal history resident within the Bragg cells; $r(x)$ and $r(y)$ may further restrict the time interval for which $v_3(t)$ and $v_6(t)$ are valid. On the other hand, Eq. (24) shows that the recovered signal is the convolution of the input signal and a system impulse response. The impulse response is proportional to the Fourier transform of the overlapping product of the aperture functions. As such, the aperture functions determine the frequency response of the system and they play the role of bandlimiting modulation transfer functions. This dual role will be further illustrated in subsequent paragraphs where we evaluate Eq. (25) in detail; for the moment, we assume that $m(q)$ is approximated by an impulse function. We can then perform the convolution indicated by Eq. (24) to find that

$$v_6(t) = s(t - T), \quad (26)$$

which is, apart from an unavoidable time delay, exactly the signal that was fed to the transmitter.

In this analysis we have not placed any constraints on the distance between planes P_1 and P_2 or the position of the photodetector in plane P_2, other than the constraints given by Eqs. (4) and (6). We have shown, therefore, that the signal $s(t)$ can be recovered from the output of the receiver for any system geometry, provided that the transmitter and receiver have conjugate structures. This important result shows that time delays induced by the transmitter geometry are compensated exactly in the receiver. This feature will become clearer as we examine the response to some specific signal waveforms.

A. Impulse Response

We now derive the response of the system to an impulse. We let $s(t)$ be an impulse function $\delta(t)$ in Eq. (1) and solve Eq. (17) for the output of the transmitter:

$$v_3(t) = r^*(vt - L/2)a(vt - L/2)\exp[-j2\pi f_c(t - T/2)] \times \exp[-j(\pi v^2/\lambda D)(t - T/2)^2], \quad (27)$$

where the aperture function $a(vt - L/2)$ determines the time interval for which the impulse is in the cell; if $a(x) = 0$ for $|x| > L/2$, the impulse is in the system for $0 < t < T$. We see that $v_3(t)$ is a chirp function on an offset frequency, with its amplitude modified by the aperture functions. If the aperture functions are real valued and slowly varying, the instantaneous frequency of $v_3(t)$ is given simply by the time derivative of the phase:

$$f = f_c + (v^2/\lambda D)(t - T/2), \quad (28)$$

which is valid for all $D \leqq D_m$. If the Fresnel plane is located so that $D = D_m$, we can use Eq. (4) in Eq. (28) to show that the frequency is $f_c - W/2$ at $t = 0$ and increases with time until $t = T$, when the frequency is $f_c + W/2$. Thus, the chirp function has bandwidth W, centered at f_c. Since the instantaneous frequency of the chirp is a linear function of time, we see that the aperture functions in Eq. (27) determine the frequency response of the system. That is, the envelope of the chirp function is a direct measure of the MTF of the transmitter.

In Sec. II we argued that the onset of the chirp response occurs at t_1 and that the chirp response ends at $t_2 = t_1 + T_p$. These arguments were predicated on the concept of a bandlimited impulse function, a function that has no meaning in geometrical representations of signals. We now show that those concepts are consistent with diffraction theory. We let $D = cD_m$, so that Eq. (28) becomes

$$f = f_c + (W/cT)(t - T/2). \quad (29)$$

Suppose that the chirp response starts at some arbitrary time t_1 to produce frequency f_1 and ends at t_2 to produce frequency f_2. We substitute these values into Eq. (29) to find that

$$f_2 - f_1 = (W/cT)T_p, \quad (30)$$

and, since $f_2 - f_1$ must equal to W, we find that T_p must be equal to cT. Conversely, if we set $(f_2 + f_1)/2 = f_c$, we find that $t_1 = (1 - c)T/2$. Thus, the output of the transmitter has bandwidth W and a center frequency

f_c for any system geometry. These results confirm those developed in Sec. II.

Additional time delays can be obtained if the reference beam is directed to other points in the Fresnel plane. In this case, Eq. (17) has a slightly altered form, but it is easy to show that the spectral content of $v_3(t)$ is not affected by the change in geometry. A key result, then, is that we can alter the impulse response in terms of time delays or chirp durations, without increasing the necessary channel bandwidth.

We now feed $v_3(t)$ to the receiver and show how the chirp function is converted to a bandlimited impulse. We can either substitute $v_3(t)$, as given by Eq. (27), into Eq. (19) by way of Eq. (18), or we can set $s(t)$ equal to a delta function in Eq. (23); in either case, we remove the baseband signals $v_4(t)$ and $v_5(t)$ with a filter to obtain

$$v_6(t) = \exp[j2\pi f_c(t-T)]\exp[j(\pi v^2/\lambda D)(t-T)^2] \times \int_{-\infty}^{\infty} b(y)r^*(y)a^*(vt+y-L)r(vt+y-L) \times \exp[j(2\pi yv/\lambda D)(t-T)]dy. \quad (31)$$

The integral is the Fourier transform of the product of four aperture functions, similar to that for $m(q)$ from Eq. (25). Suppose, for sake of convenience, that all aperture functions are rectangular functions. We combine the functions so that the integral becomes

$$\int_{L/2-vt}^{L/2} \exp[j(2\pi yv/\lambda D)(t-T)]dy = t\exp[-j(\pi v^2/\lambda D)(t-T)^2] \times \operatorname{sinc}[(v^2/\lambda D)t(t-T)]; \quad 0 \leqq t \leqq T. \quad (32)$$

If the aperture functions are not uniform, we conclude that the impulse response is broadened somewhat, but its basic nature is not significantly changed. We use Eq. (4) in Eq. (32) and combine Eq. (32) with the remaining terms of Eq. (31). The real part of the result is

$$v_6(t) = t\operatorname{sinc}[(W/T)t(t-T)]\cos[2\pi f_c(t-T)]; \quad 0 \leqq t \leqq T. \quad (33)$$

This result shows that $v_6(t)$ consists of a carrier frequency f_c, modulated by a curious form of a sinc function envelope. The argument of the sinc function is quadratic in time and its amplitude is linearly proportional to time. The time interval between successive nulls is small when $t = 0$, increases to a maximum value when $t = T/2$, and becomes small again when $t = T$. The first zeros of the sinc function occur at time intervals of $1/W$ before and after the central value; this satisfies our notion that a bandlimited impulse response must be reconstructed at the output of the receiver.

The interesting result given in Eq. (33) tends to disguise the spatial/temporal evolution of the receiver response. When $v_3(t)$ first enters the receiver, light is diffracted from only a small signal packet near $x = L/2$, which is the position of the transducer in the receiver. The resultant sinc function is spread over a large region in plane P_3, but since the instantaneous frequency of this packet is $f_c - W/2$, the centroid of the sinc function is directed toward less negative values of ξ. This light is therefore far away from the reference beam position and its amplitude is small because the packet length, proportional to vt, is small. As time increases, the packet size increases, and the scale of the sinc function contracts as its centroid moves at velocity v through plane P_2.

We see, then, that a well-formed spatial sinc function is always produced by $v_3(t)$. As time increases, the scale of the function decreases so that, when $v_3(t)$ fills the Bragg cell, the most compact spatial sinc function travels past the fixed reference spot $R(\xi)$. The time convolution of the moving diffraction pattern and the fixed reference beam produces Eq. (33). The reason for the quadratic argument of the sinc function now becomes clear: the factor $(t - T)$ provides information about the distance from the centroid to the reference beam, while the factor t provides information about the spread of the sinc function as well as its magnitude. As the chirp function leaves the Bragg cell, the sinc function vanishes in a fashion opposite to that in which it evolved.

In Fig. 4 we plot the envelope of $v_6(t)$, as given by Eq. (33), for the cases where $T = 10$ μsec and $W = 50$ MHz ($WT = 500$), and where $T = 10$ μsec and $W = 100$ MHz ($WT = 1000$). Note that the envelope has significant amplitude only near $t = T$ and its shape is essentially the same as that for a sinc function whose argument is linear in time. The result for $WT = 1000$ is shown as a solid line; we see that the first zero occurs a time $1/W$ before the central value. The result for $WT = 500$ is shown as a dashed line; the central lobe is broader by a factor of 2, as expected, because the frequency content for the lower time-bandwidth product signal is less. The sinc functions shown in Fig. 4 also specify the required reference beam spot sizes; the conversion from time to space is obtained by using the acoustic velocity.

The scale of the impulse response derived here gives the performance of the system for all geometries, a result that seems strange at first. Suppose that the distance from the imput plane to the Fresnel plane decreases in the transmitter. The chirp duration then decreases to cT and, since the bandwidth is constant,

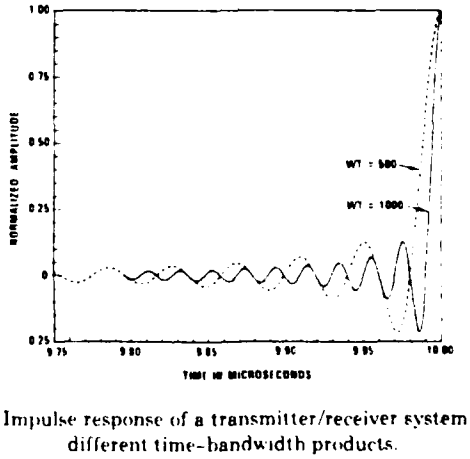

Fig. 4. Impulse response of a transmitter/receiver system for two different time-bandwidth products.

we find that the chirp rate must increase to W/cT. In the receiver, this function produces a traveling focused spot that has its maximum amplitude at a distance corresponding to a focal length of cD_m. Thus, the f/No. of the chirp is independent of the geometry, as is the size of the reconstructed impulse; these results are a direct consequence of the bandlimited nature of the system. A further conclusion is that the required reference beam spot size is determined solely by the bandwidth of the signal. As shown in Fig. 1, the reference beam can be focused at any plane P_3 for which $D < D_m$, provided that the imaging condition between planes P_0 and P_3 are satisfied. In the limit as $c \to 0$, the reference beam will be focused at plane P_1 and the transmitter output will be a time delayed version of $s(t)$, without any time spreading. Thus, even though the chirp rate may become very high as $c \to 0$, a fixed reference spot size will always resolve the information content of $s(t)$.

B. Short Pulse

We now examine the response of the transmitter to a short pulse of frequency f_s and duration T_0, where $1/W \ll T_0 < T$. It is convenient to denote the frequency associated with this tone burst by $f_j = f_s - f_c$ and to confine f_j so that $|f_j| \leqq W/2$. We represent the signal within the Bragg cell of the transmitter as

$$f(t,x) = a(x)\,\mathrm{rect}[(x - vt + L/2 + vT_0)/vT_0]\,\exp(-j2\pi\theta_B x/\lambda) \times \exp[-j2\pi(f_c + f_j)(t - T/2 - x/v)], \quad (34)$$

where the rect function controls the duration of the tone burst. We substitute Eq. (34) into Eq. (17) and perform the algebraic manipulations needed to obtain the standard form of the Fresnel integral:

$$v_3(t) = \exp[-j2\pi(f_c + f_j)(t - T)] \times \int_{-\infty}^{\infty} a(\sqrt{\lambda D/2}\,z + f_jL/W)r^*(\sqrt{\lambda D/2}\,z + f_jL/W) \times \mathrm{rect}[(\sqrt{\lambda D/2}\,z + f_jL/W - vt + L/2 + vT_0)/vT_0] \times \exp[-j(\pi/2)z^2]dz. \quad (35)$$

We shall numerically compute Eq. (35) later and quantify the constraint on T_0. For the moment we can say that the Fresnel transform has value only in the vicinity of $z = 0$, provided that T is not too small and that the aperture functions are slowly varying; Eq. (35) then becomes

$$v_3(t) = a(f_jL/W)r^*(f_jL/W)\exp[-j2\pi(f_c + f_j)(t - T)], \quad (36)$$

where the aperture functions are evaluated at the midpoint of the short pulse. The time interval for which $v_3(t)$ has value is derived from the argument of the rect function in Eq. (35):

$$f_jL/W - vt - L/2 + vT_0 = \pm vT_0/2. \quad (37)$$

The time at which the leading edge of the output arrives is determined by using the positive sign on the right-hand side of Eq. (37):

$$t_j = T/2 + f_jT/W, \quad (38)$$

which reveals the relationship between the time of arrival and the frequency content of a short pulse. When $f_j = W/2$, light is diffracted at maximum negative angle relative to θ_B and the leading edge arrives

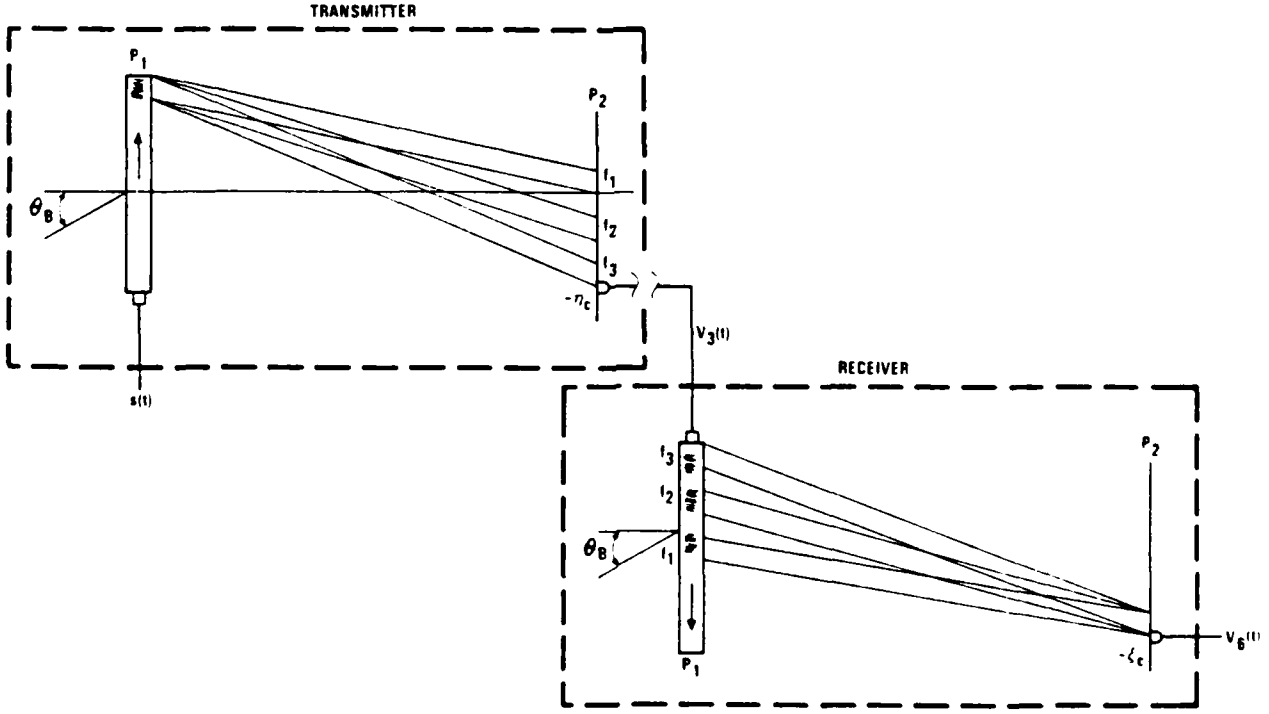

Fig. 5. Transmitter and receiver geometry for a multitone short pulse.

with the maximum possible delay. Similarly, the pulse arrives at $t = 0$ when $f_j = -W/2$. The trailing edge of the response always occurs an interval T_0 later than the arrival of the leading edge. As suggested by Eq. (36), the aperture functions behave as modulation transfer functions. For example, the values of the aperture functions are $a(L/2)$ and $r^*(L/2)$ when $f_j = W/2$. These values are consistent with the fact that the response to a short pulse with this frequency occurs when $t = T$.

It is apparent, then, that the transmitter response is a function of the duration and frequency of the short pulse. Further, if the pulse contains several frequencies, the output consists of a sequence of responses spaced in time according to the difference between adjacent frequencies. The time difference between f_j and f_i is, from Eq. (38), simply $(f_j - f_i)T/W$, which confirms Eq. (8). In Fig. 5 we illustrate how the multiple tones are generated and reconstructed with the appropriate transmitter and receiver configuration. In the transmitter section, a short pulse with frequencies f_1, f_2, and f_3 is just about to leave the Bragg cell. The photodetector in plane P_2 has, therefore, just finished forming $v_3(t)$ for this pulse. When the part of $v_3(t)$ due to f_1 enters the receiver, light is directed toward the positive values of ξ. As successive frequency components of $v_3(t)$ enter the receiver, their Fresnel transforms combine as they move toward the photodetector. As depicted in Fig. 5, the pulses in the receiver are positioned so that the original multitone signal is well formed, both spatially and temporally, at plane P_2. In this fashion, all the components of the arpeggiated chord join to reconstruct the chord as the output signal $v_6(t)$. We note in passing that the arpeggiating rate is the same as the chirp rate for any given geometry; this is consistent with the idea that an impulse function, which is the limiting form of a short pulse, contains all frequencies and the arpeggio becomes a glissando.

To more fully explore the system response to short pulses, we wrote a program to compute Eq.(35) for pulses having a normalized width $k = T_0/T = L_0/L$. For convenience, we removed the time dependence and normalized the coordinate in the Fresnel plane so that $\rho = 2\eta/L$. In Fig. 6 we show the magnitude of the response as a function of ρ for various values of k. If the pulse is fairly wide, the diffraction pattern resembles the pulse itself, except for some internal fringes. The width of the diffracted pulse, taken as the distance between the half-amplitude response points, is essentially unchanged. Thus, we can say that the Fresnel transform of a long pulse is, aside from the internal fringes, similar to the pulse itself. In all cases, the Fresnel pattern is symmetrical about $\rho = 0$.

When $k = 0.01$, we find that the Fresnel transform has a smaller central magnitude and begins to take on the form of a sinc function. In Fig. 7 we show the Fresnel transforms for shorter pulses, and we see that they more accurately represent the far-field patterns of pulses as the pulse duration decreases. The central lobe of the pattern just covers the region $|\rho| \leqq 1$ when k

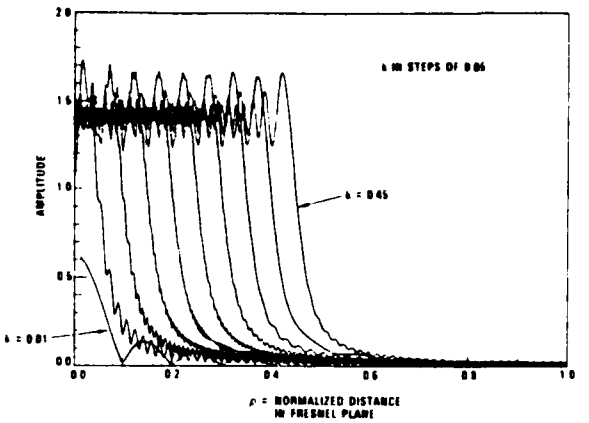

Fig. 6. Fresnel transforms of pulses with normalized widths ranging from $0.01 \leq k \leq 0.45$ in steps of 0.05.

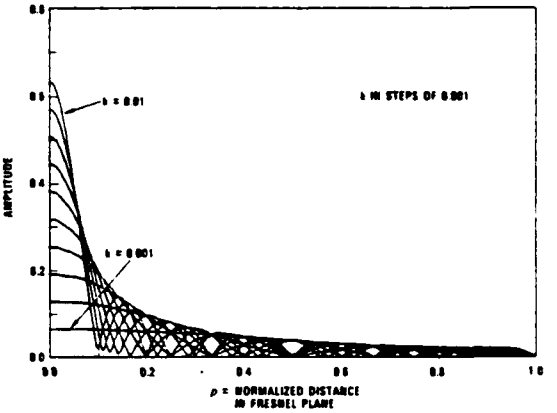

Fig. 7. Fresnel transforms of pulses with normalized widths ranging from $0.001 \leq k \leq 0.01$ in steps of 0.001.

$= 0.001$. Since these results were computed for a system having a time–bandwidth product of 2000, we find that a pulse containing just two resolution elements spreads light over a region $|\eta| \leqq L/2$ in the Fresnel plane.

In Fig. 8 we plot the value of ρ at which the response to a pulse has its half-amplitude value. As expected, $\rho \cong k$ for the longer pulses and, in the absence of diffraction, the nearly straight line relationship would extend to the origin. For small values of k, however, we find that $\rho \propto 1/k$. The transition between these two regions occurs at $k_0 \approx 0.025$ when $WT = 2000$ and represents the transition from Fresnel diffraction to Fraunhofer diffraction. From the computer solutions we obtain the general relationship that

$$k_0 = \frac{1.58}{\sqrt{2TW}} \tag{39}$$

at the transition point. We use Eq. (4) in Eq. (39) to find that the transition from Fresnel to Fraunhofer diffraction occurs when $L_0 \approx \sqrt{1.25\lambda D_m}$, which is close to the approximation usually stated in optics texts.

We claimed earlier that Eq. (36) is a valid approxi-

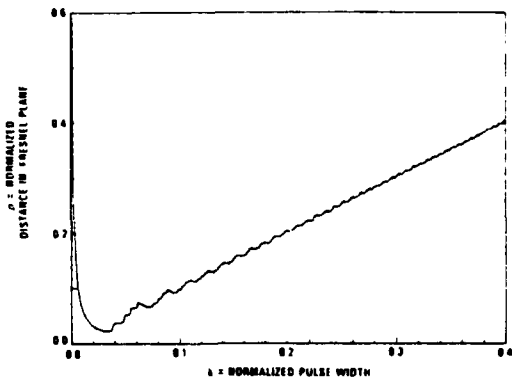

Fig. 8. Plot of half-amplitude response width in a Fresnel plane as a function of input pulse width.

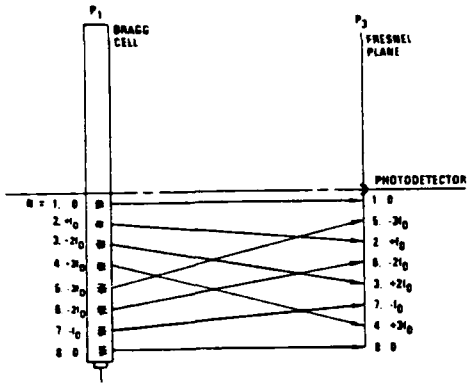

Fig. 9. Configuration for permutation of time samples.

mation to Eq. (35) provided that T_0 is not too small. We can use the results from Figs. 6–8 to gain further insight to this qualitative claim. When $T_0 > k_0 T$, the effect of diffraction from one edge of the pulse is nearly independent, at plane P_2, from that of the other edge. When $T_0 < k_0 T$, the diffraction from the edges combines to produce the far-field patterns. Stated another way, when $T_0 < k_0 T$, the argument of the Fresnel integral of Eq. (35) is not slowly varying with respect to the kernel so that the integral cannot be evaluated through the principle of stationary phase simply by setting $z = 0$.

We are now in a position to show how to implement, for certain signal formats, the time sample permutation method described by Wyner.[5] Suppose that an analog signal is sampled at time intervals of T' seconds by a gating function to produce a frame of N samples that are T_0 seconds in duration, where T_0 satisfies the criterion for a short pulse. Each of the N samples is multiplied by $\cos[2\pi(f_c + f_j)t]$ where f_j is a frequency drawn from a set of N frequencies in the band $\pm W/2$. We have thus converted the analog signal to a pulse amplitude modulated signal; the associated frequencies f_j will determine how the time permutation evolves.

Suppose that the Bragg cell contains N samples of the signal as shown in Fig. 9. Again, we appeal to the geometric representation used in Sec. II to illustrate the idea. We let $N = 8$ and show the situation at the point in time when the first frame of information has entered the Bragg cell. Each time sample has an associated frequency which we now denote as mf_0, $|m| \leqq N$. For example, the fifth sample ($n = 5$) has an associated frequency $-3f_0$ which is just sufficient to move this time sample to the second time slot in plane P_3. Sample $n = 3$ in plane P_1 has an associated frequency $+2f_0$ which moves it to the fifth time slot in plane P_3. Since the sample positions in plane P_3 are a permutation of the sample positions in plane P_1, there are $N!$ ways in which the frame of N samples can be transmitted.

As shown in Fig. 9, the photodetector placed at $\eta = 0$ is just ready to receive light from the frame of data. As the data flow through the Bragg cell in a continuous fashion, the samples are permuted in time. The samples from the next frame are frequency encoded, appropriate to the new permutation, while the previous frame is being transmitted. The Bragg cell must be $2N$ samples long to accommodate the maximum time delay required when the first sample in a frame must be moved to the end of the frame. As shown, the frequencies have been chosen to perform a particular permutation called a perfect shuffle.[16] When the conjugate receiver is used, we perform the inverse permutation or unshuffle automatically to reconstruct the proper sample sequence.

C. Continuous-Wave Signal

When the input signal is a cw signal represented by $f_j = f_s - f_c$, the rect function in Eq. (35) is valid for all time and can be removed from the integrand. We then have that

$$v_3(t) = \exp[-j2\pi(f_c + f_j)(t - T)] \int_{-\infty}^{\infty} a(\sqrt{\lambda D/2}\, z + f_j L/W) \times r^*(\sqrt{\lambda D/2}\, z + f_j L/W) \exp[-j(\pi/2)z^2]\, dz. \quad (40)$$

From Eq. (40) we conclude that the integral gives the modulation transfer function of the system. When the aperture functions are slowly varying, the integral has significant value only when $z = 0$, and the MTF can be approximated by $a(f_j L/W) r^*(f_j L/W)$.

This result suggests that frequency excision can be performed for a cw frequency by stopping a region of either the signal or reference aperture function. Since there is a one-to-one correspondence of spatial positions to spatial frequencies, a stop at $x = f_j L/W$ in the reference beam aperture will create a notch to excise the frequency f_j even though the system does not contain a frequency plane. Frequencies cannot be excised as cleanly, however, as when a stop is placed in a Fourier plane, because the Fresnel integral in Eq. (40) can be evaluated at $z = 0$ only if the integrands are slowly varying. As the stop becomes very narrow, this stationary phase approximation does not describe the physical situation accurately. If $L_0 > k_0 L$, the spectral notch is reasonably well formed. But as $L_0 \to 0$, the notch actually broadens and the performance of the

excisor degrades. A stop produces a result similar to that of a short pulse; we can represent a stop at frequency f_j as

$$r_j(x) = r(x) - r(f_jL/W)\,\mathrm{rect}[(x - f_jL/W)/L_0], \tag{41}$$

where L_0 is the width of the notch. As shown by numerical computation, the second term in Eq. (41) produces a response similar to that shown in Fig. 6. Since $k_0 = 0.025$ at the transition region for a system with a time-bandwidth product of 2000, this method for frequency excision can be used only if we wish to remove at least 2.5% of the total frequency band. Finer frequency excision can be made by placing $r_j(x)$ in the front focal plane of the lens that creates the reference beam (see Fig. 1). In this case, any one of WT frequencies can be cleanly excised, because the stop is placed in the equivalent Fourier transform plane of the system.

D. Alternative Methods for Time Delays

In Sec. II we showed that time delays can be achieved when the Fresnel plane is located at $D < cD_m$. Additional delays can be achieved by changing the point at which the Fresnel transform is detected. One possibility, then, for scrambling the data is to provide a broad reference beam at the Fresnel plane and to use a sequence of discrete photodetectors to provide the time delays. If these photodetector positions are a distance $\eta_1, \eta_2, \ldots, \eta_j$ away from the point $\eta = \eta_c$, the time delay is

$$t_j = (1 - c)T/2 + \eta_j/v. \tag{42}$$

The advantage of this approach is that the channel bandwidth remains fixed for any selected photodetector. The disadvantages are that the reference beam power is not used efficiently, a large number of photodetectors are required, and the minimum time delay increment is determined by the finite size and spacings of the photodetector elements.

As we showed in Sec. IV.A, the focused reference beam provides the required sampling of the Fresnel transform so that a large area photodetector can be used. We can take advantage of this fact by switching the reference beam to various positions η_j to obtain the time delays. Alternatively, we can keep the reference beam fixed and cause the Fresnel transform to switch to different positions. Any relative displacement of the Fresnel transform with respect to the reference beam position will do.

If the angular displacement of either the Fresnel transform or the reference beam is achieved by means of a Bragg cell, however, the required channel bandwidth will increase. Suppose, for example, that the input signal is of the form $m(t)\cos[2\pi(f_c + f_h)t]$, where $m(t)$ is a baseband signal and f_h is randomly selected from the frequency range $|f_h| \leqq W_h/2$. From Fig. 1 we see that the effect of introducing the frequency hop is to deflect the entire diffraction pattern of $m(t)$ by an angle $\pm\theta_h$ about the Bragg angle θ_B, according to whether f_h is greater than or less than zero. We do not give the detailed analysis of this alternative method to achieve time delays here, but it is apparent from Eq. (36) that, if no further steps are taken, the channel bandwidths must be equal to $W + W_h$, centered at f_c. However, if we also modulate the reference beam with $\cos(2\pi f_h t)$, we find that a channel bandwidth of W will accommodate the transmitted signal without losing the random delay feature. The reference beam can be modulated without changing its position in plane P_2 by using an acoustooptic modulator in plane P_0 of Fig. 1. At the receiver, the signal $v_5(t)$ is demodulated by the same frequency f_h to remove the effects of the time delays, and the reference beam is shifted by f_h so that the output of the receiver $v_6(t)$ always has bandwidth W centered at f_c.

Although the channel bandwidth is not expanded by using this technique, we have placed the burden on the Bragg cells which must be designed to operate over a bandwidth $W + W_h$. The time delay in the response to an impulse is now

$$t_h = (1 - c)T/2 + (cT/W)f_h, \tag{43}$$

with the side constraint that

$$|f_h| \leqq (1 - c)W/2c. \tag{44}$$

We note that f_h is not constrained by geometric considerations; rather, it is limited by the degree to which we are willing to expand the signal Bragg cell bandwidth. Suppose that $W_h = hW$ so that the bandwidth expansion is a factor $1 + h$. We then find that $c \leqq 1/(1 + 2h)$ so that the range of time delays is $0 \leqq t_h \leqq 2hT/(1 + 2h)$. Time delays play a significant role in preventing the fine detail from being reconstructed in the proper position unless the hopping code is known. A time delay range of $T/3$ would probably be adequate; this implies that $h = 1/4$ so that the Bragg cells would need 25% more bandwidth to handle the hop frequencies.

V. Simulations

We illustrate some of the scrambling techniques described so far by their effects on images. Since images are often transmitted in a raster scanned format, the random time delay features can be readily visualized and simulated. We wrote a program to compute the spatial version of Eq. (2) for each scanned line of the image; the results were then displayed on a video monitor. Since the transmitter output is real valued, we added a bias term to the output to avoid distortion due to rectification of the negative values.

In the first example, we illustrate the Fresnel transforms for rectangular pulses that vary in width from 128 pixels at the top of 2 pixels at the bottom [see Fig. 10(a)]. The ends of the pulses form a staircase pattern and the Fresnel transform for each scan line is computed in the horizontal direction only. Figure 10(b) shows the Fresnel transform; these patterns differ somewhat from those we normally observe because here we display the biased magnitude, not the more familiar intensity, of the Fresnel transform. The width of the Fresnel transform is equal to that of the pulse, when the pulse width is large, as seen near the top of Fig. 10(b); evidence of internal fringes is lacking

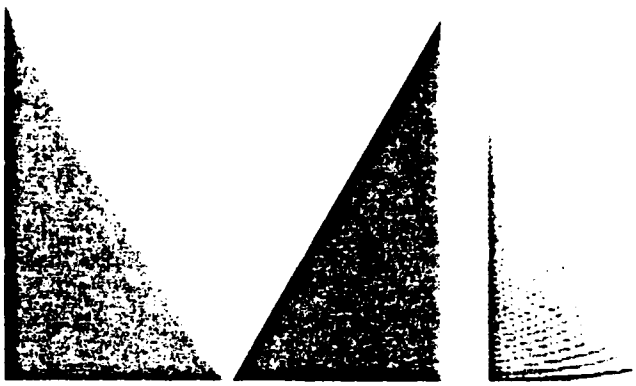

(a) (b)

Fig 10. Fresnel transforms: (a) rectangular pulses ranging in width from 128 pixels to 2 pixels; (b) computer-generated Fresnel transform of pulses.

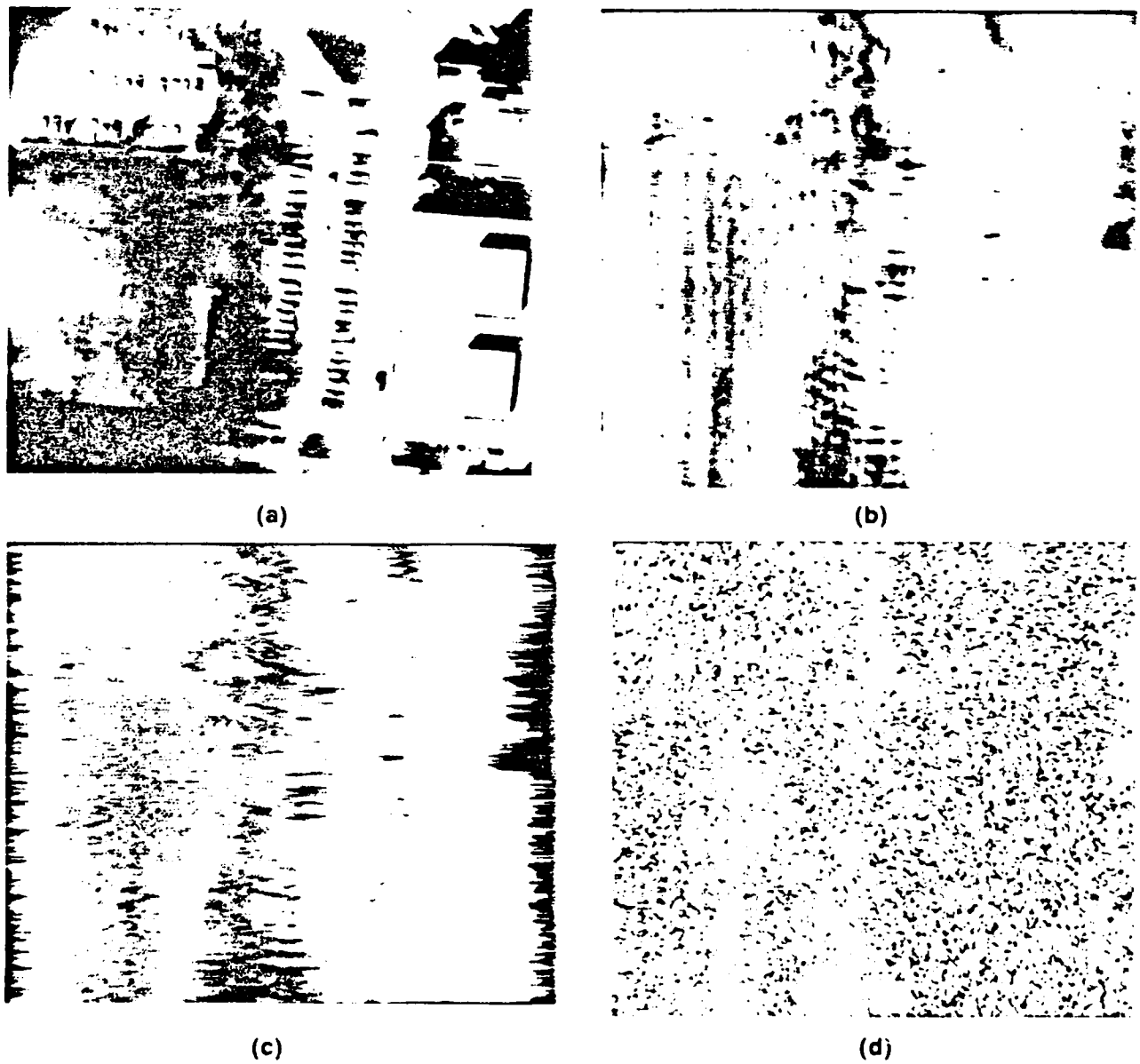

(a) (b) (c) (d)

Fig 11. Fresnel transforms: (a) input scene; (b) Fresnel transform of input scene; (c) same as (b) but with ±8 pixel random delay/advance; (d) same as part (b) but with random polarity reversals.

due to the exposure required to capture the response from the shorter pulses. When the pulse width becomes very small, as near the bottom of Fig. 10(a), the Fresnel transform broadens into the far-field pattern as shown in Fig. 10(b); the peak amplitude also decreases as the sinc function becomes broader. These results parallel those shown in Figs. 6–8.

Figure 11(a) shows a scene that has regions of high contrast, low contrast, fine detail, and coarse detail. The Fresnel transform of this scene is shown in Fig. 11(b). Note that the fine detail associated with vertical edges is spread over a large region in the horizontal direction. The clearest examples of this spreading are in the upper left-hand corner and in the left central part of the scene. Detail in the parking lots is scrambled; the two rows of vehicles in the central part of the scene are nearly blended together in the transformed output. Long horizontal lines are not, of course, altered appreciably in the vertical direction because the Fresnel transform is 1-D in this case.

Figure 11(c) shows the Fresnel transform for the same scene but with a random time delay imparted to each scan line which simulates a random frequency hop of the signal. The delays were selected from the uniformly distributed 16-pixel interval at the nominal start of scan. The contribution to the scrambling from the time delays is not a large as initially expected, because the random delays produce a result which, viewed macroscopically, is similar to a low pass filtering operation. Since the Fresnel transform is also a low pass operation (see Fig. 10), the time delays do not seem to add significantly to the scrambling. They do, however, play a significant role in reconstructing the original signal at the output of the receiver. From Sec. IV.D, we find that this range of delays requires 7% more bandwidth from the Bragg cells but no additional channel bandwidth.

The scene is now reasonably well scrambled except for the lowest possible frequencies. These can be further scrambled by randomly altering the polarity of the Fresnel transform on each scan line as shown in Fig. 11(d). In this example we simply multiplied the Fresnel transform for each scan line by ±1 before adding the bias level. As a result, the effects of polarity reversals are most evident in the bright regions of the scene. A more effective scheme would be to change the polarity about the mean value of the entire scene. The random polarity is relatively more useful than the random time delays in this example.

These examples do not illustrate all the phenomena or exhaust the possible variations on the scrambling techniques available. For example, because we have computed the Fresnel transform of spatial signals, the temporal frequency characteristics of the transmitted signal are not evident. Nor do they illustrate the interesting frequency-dependent time-of-arrival effects for tone bursts or multitone short pulses. We must also keep in mind that the results shown in Fig. 11 could be obtained from the transmitted signal because we did not introduce or scramble the sync pulses necessary to define the start of scan. These pulses would normally be scrambled so that the image would be more difficult to reconstruct.

So far we have described scrambling techniques in which we have generally preserved the channel bandwidth. If we wish to implement the random time delay technique, however, we must have sufficient time between raster scan lines to accommodate the desired range of delays. If this time interval is not available, the channel bandwidth must be increased. As noted before, a modest increase in channel bandwidth may be an acceptable trade-off relative to the large increase required when digitizing and encoding the wideband signal. We now briefly consider generalizations of the scrambling technique that do not preserve bandwidth.

As can be seen from Fig. 1, we have the option of (1) using a signal $r_1(t)$ to modulate the reference source at plane P_0 in time only, (2) using a signal $r_2(t,x)$ to modulate the reference beam at plane P_1 in space and time, or (3) using a signal $r_3(t)$ to phase or frequency modulate the input signal. We can also, of course, use combinations of these modulation schemes.

Consider, for example, a modulating signal $r_1(t)$ that has constant amplitude but a slowly varying frequency. Its effect on the output of the transmitter, when the input is an impulse function, is to produce a chirp function that is aberrated in the sense that its temporal frequency is not a linear function of time. Without compensation, this signal cannot be compressed in the receiver to provide good resolution. If, however, the signal $r_1^*(t)$ is applied to the received signal, the conjugate of the aberration is provided so that the original signal can be recovered. By combining the types of modulation cited, several interesting effecs can be produced. We shall defer a discussion of them to a subsequent paper.

VI. Summary and Conclusions

The Fresnel transform, not frequently used in signal processing, has some interesting and useful properties when applied to Bragg cell processors for purposes of signal scrambling. We have derived the optimum optical geometry, given the key parameters of a wideband time signal. We showed that a photodetector can be placed anywhere within a cone defined by the ends of the Bragg cell and a point on the optical axis located a distance D_m from the Bragg cell. A wide range of time spreading and time delays can be obtained thereby, depending on the position of the photodetector within the cone.

The time of arrival of the leading edge of a pulse is dependent on its frequency; multitone short pulses can be divided into separate pulses with most geometries. For some signals it may be useful to time permute a sequence of sample pulses by controlling the frequency of the pulse. As an example, a sequence of N pulses with different amplitudes can be rearranged in any order by using a Bragg cell whose length is equivalent to $2N$ pulses. A perfect shuffle of the N pulses can thus be performed, as can exchange and bypass functions. Thus, there may also be some useful applica-

tions of Fresnel transforms in optical numeric computing.

Simulations illustrate some of the basic concepts for scrambling analog signals in a raster format. If we allow for some bandwidth expansion of the transmission channel, a much broader range of scrambling operations becomes available by virtue of modulating the reference source in time or space or both.

I thank G. H. Thaker for assistance with computer programming for the Fresnel transforms, R. H. Cofer and J. H. Reece for help with the simulations, and A. M. Bardos for helpful comments and criticism.

This work was supported by the U.S. Army Research Office.

References

1. D. Gabor, "Microscopy by Reconstructed Wavefronts," Proc. R. Soc. London Ser. A **197**, 454 (1949).
2. E. N. Leith and J. Upatnieks, "Reconstructed Wavefronts and Communication Theory," J. Opt. Soc. Am. **52**, 1123 (1962).
3. L. J. Cutrona, E. N. Leith, L. J. Porcello, and W. E. Vivian, "On the Application of Coherent Optical Processing Techniques to Synthetic-Aperture Radar," Proc. IEEE **54**, 1026 (1966).
4. E. N. Leith and A. L. Ingalls, "Synthetic Antenna Data Processing by Wavefront Reconstruction," Appl. Opt. **7**, 539 (1968).
5. A. D. Wyner, "An Analog Scrambling Scheme Which Does Not Expand Bandwidth, Part I: Discrete Time", IEEE Trans. Inf. Theory **IT-25**, 261 (1979); "Part II: Continuous Time," IEEE Trans. Inf. Theory **IT-25**, 415 (1979).
6. "Speech and Facsimile Scrambling and Decoding," Summary Technical Report of Division 13, NDRC, Vol. 3, Washington, D.C. (1946). This report is available through DTIC, Cameron Station, Alexandria, Va. 22314.
7. IEEE Journal on Selected Areas in Communications, Vol. **SAC-2** (May 1984).
8. R. L. Whitman, A Korpel, and S. N. Lotsoff, "Application of Acoustic Bragg Diffraction to Optical Processing Techniques," in *Proceedings, Symposium on Modern Optics*, J. Fox, Ed. (Polytechnic Press, Brooklyn, 1967), p. 243.
9. A. Korpel, S. N. Lotsoff, and R. L. Whitman, "The Interchange of Time and Frequency in Television Displays," Proc. IEEE **57**, 160 (1969).
10. W. T. Rhodes and J. M. Florence, "Frequency Variant Optical Signal Analysis," Appl. Opt. **15**, 3073 (1976).
11. J. M. Florence, "Frequency Variant Optical Signal Processing," Ph.D. Thesis, Georgia Institute of Technology, Atlanta (1979).
12. A. Papoulis, *Systems and Transforms with Applications in Optics* (McGraw-Hill, New York, 1968), p. 322.
13. A. VanderLugt, "Operational Notation for the Analysis and Synthesis of Optical Data-Processing Systems," Proc. IEEE **54**, 1055 (1966).
14. A. VanderLugt, "Packing Density in Holographic Systems," Appl. Opt. **14**, 1081 (1975).
15. D. H. Towne, *Wave Phenomona* (Addison-Wesley, Reading, Mass., 1967).
16. H. S. Stone, "Parallel Processing with the Perfect Shuffle," IEEE Trans Comput. **C-20**, 153 (1971).

John F. Walkup of Texas Tech University at the 1984 OSA Annual Meeting. *Photo* F. S. Harris, Jr.

APPENDIX G

FRESNEL TRANSFORMS AND OPTICAL COMPUTING

PRESENTED AT SPIE ADVANCED INSTITUTE

ON HYBRID AND OPTICAL COMPUTING

LEESBURG, VIRGINIA, MARCH 1986

Fresnel Transforms and Optical Computing

A. VanderLugt
Advanced Technology Department
Harris Corporation
P. O. Box 37
Melbourne, FL 32901

Abstract

The Fresnel transform provides a means to implement circuit switching networks by using optical techniques. Since photons can cross paths without interaction, non-blocking configurations are easy to achieve. Furthermore, any arbitrary interconnections between two N-port systems can be configured; the network can be rapidly reconfigured as needed due to the dynamic nature of acousto-optic cells.

Introduction

Fresnel transforms have some useful spatial/temporal properties when used in conjunction with acousto-optic cells. A Fresnel transform having a low dispersion coefficient, as determined by the a propagation distance D, will closely resemble the signal. As the dispersion coefficient increases, the Fresnel transform begins to sort the information according to its spatial position, corresponding to the time coordinate, and according to its angular spread, corresponding to its frequency content. For a very large dispersion coefficient, the Fresnel transform is equivalent to the Fourier transform; it then most accurately represents the frequency content of the signal. Between the space and the Fourier domains, then, there exists a continuum of Fresnel transform planes that have a mixture of the dominant properties of the time and frequency planes.

These properties of Fresnel transforms have been applied to scrambling analog signals.[1] Analyses of the Fresnel transforms of CW, impulse, and short pulse signals were developed in terms of spatial/temporal content. Some scrambling schemes were then introduced, including one in which the time samples are permuted. It is the permulation idea that suggested the application of Fresnel transforms to optical computing.

In this paper we review the basic results from Reference 1. We then consider some ways that this scheme can be used for interconnection schemes in computers.[2] The Fresnel transform provides for both local and global interconnects on a dynamic basis, as we shall see.

The Fresnel Transform

Consider a Bragg cell located at plane P_1 in Figure 1. Suppose that the cell is constructed of a material that allows operation in the tangential mode.[3] As a result, when the applied signal is $s(t) = \cos(2\pi f_c t)$, where f_c is the center frequency of the cell, the diffracted light is normal to the exit face of the cell. As the frequency varies from $f_c - W/2$ to $f_c + W/2$, the light is deflected over the angular range $|\theta| \le \theta_m$. At any plane, located a distance D from the Bragg cell, we can represent the Fresnel transform of a signal s(t) as

$$g(t,\eta) = \int_{-\infty}^{\infty} s(t,x)\, \exp[-j(\pi/\lambda D)(x-\eta)^2]dx, \tag{1}$$

where the exponential function represents the free space response to an impulse; x is the spatial coordinate at plane P_1 and η is the spatial coordinate at the Fresnel transform plane P_2. The cell serves to convert the temporal signal s(t) into a space/time signal s(x,t) by the relationship that

$$s(x,t) = a(x)s(t-T/2-x/v), \tag{2}$$

where a(x) is an aperture weighting function that includes the truncation points at $x = \pm L/2$, v is the acoustic velocity, and $T = L/v$ is the fill time of the cell. A CW drive signal at the minimum frequency $f_m = f_c - W/2$ produces a light wave that propagates as a plane wave at the angle $\theta_m = \arcsin(W\lambda/2v)$. The edge ray of this bundle intercepts the optical axis at a distance D_m:

$$D_m = Lv/\lambda W. \tag{3}$$

In a similar fashion, the opposite edge ray from a frequency $f_c + W/2$ will also intercept the optical axis a distance D_m from plane P_1. If the distance between planes P_1 and P_2 is greater than D_m, the higher frequencies in the band W cannot be detected at the point $\eta = 0$. Since $L = vT$, we can derive an important relationship connecting the physical parameters of the optical system with the key parameters of the signal:

$$\frac{v^2}{\lambda D_m} = \frac{W}{T} . \tag{4}$$

Next, consider the system response to an impulse function. Since the input signal is bandlimited, the shortest pulse that the system can support will generate rays confined to the range of angles $\theta = 2\theta_m$. The marginal rays for such an impulse function that has just entered the Bragg cell are shown by dotted lines in Figure 1. If $D = D_m$, the photodetector receives light as soon as the impulse enters the Bragg cell and continues to receives light until the impulse leaves the Bragg cell; we conclude that the impulse is spread or dispersed into a chirp signal of duration T. The temporal frequency of the chirp varies linearly in time from $f_c - W/2$ to $f_c + W/2$. If the distance between planes P_1 and P_2 exceeds D_m, there is no increase in the time spreading of the impulse. The maximum distance between planes P_1 and P_2 is therefore the value that satisfies (4); this ensures that no frequencies are missed and provides for maximum time spreading.

A third type of signal envelope is a short pulse of duration T_o; such pulses are of greatest interest to us here. Consider a pulse whose duration is of the order of $T/8$ as shown in Figure 2, and let the observation point be at $\eta = 0$ in plane P_2. Further, suppose that this pulse contains frequency components at f_1, f_2, and f_3 such that $f_1 > f_2 > f_3$. The photodetector then receives energy at time intervals related to the frequency content of the pulse. If we think of the pulse as a musical chord, we find that the time difference t_n between the first two notes is given by $t_n = (\eta_1 - \eta_2)/v$, where $\eta_1 - \eta_2$ is the distance between the leading edges of the pulses in plane P_2. By using the basic rules of diffraction theory, we find that

$$t_n = (\eta_1 - \eta_2)/v = (f_1 - f_2)\lambda D_m/v^2, \tag{5}$$

which, through the use of (4), can be reduced to

$$t_n = (f_1 - f_2)T/W. \tag{6}$$

Thus, we see that a chord is encoded as a succession of pure tones, each of duration T_o. The behavior of these short pulses provide interesting possibilities for optical computing.

The discussions so far are based on geometrical optics; we need to consider diffraction effects to better understand the response in the Fresnel plane. To more fully explore the system response to short pulses, we wrote a program to compute the Fresnel transform for pulses having a normalized length $k = T_o/T = L_o/L$ (See Reference 1 for details). For convenience we removed the time dependence and normalized the coordinate in the Fresnel plane so that $\rho = 2\eta/L$. In Figure 3, we show the magnitude of the response as a function of ρ for various values of k. If the pulse is fairly wide, the diffraction pattern resembles the pulse itself, except for some internal fringes. The width of the diffracted pulse, taken as the distance between the half-amplitude response points, is essentially unchanged. Thus, we can say that the Fresnel transform of a long pulse is, aside from the internal fringes, similar to the pulse itself for all values of

$$k \geq \frac{1.58}{\sqrt{2TW}} . \tag{7}$$

The number of pulses that can be stored in the cell is, to a first order approximation, proportional to $1/k$ so that

$$N = \frac{1}{k} \leq \sqrt{0.8TW}. \tag{8}$$

We can therefore store up to 40 such pulses in the cell if the time-bandwidth product of the cell is $TW = 2000$, and still retain spatial resolution at the Fresnel plane. We may need to reduce this number somewhat, in some applications, to reduce cross-talk between adjacent pulses.

Application to Computing

We have illustrated the properties of the Fresnel transforms of CW, impulse, and short pulse signals. We now concentrate on how we might use these properties in optical computing. We first review a method for permuting time samples as an analog scrambling technique.[1,4] Suppose that an analog signal is sampled at time intervals of T' seconds by a gating function to produce a frame of N samples that are T_o seconds in duration, where T_o satisfies the criterion for a short pulse. Each of the N samples is multiplied by $\cos[2\pi f_j t]$, where f_j is a frequency drawn from a set of N frequencies in the band $f_c \pm W/2$. We have thus converted the analog signal to a pulse amplitude modulated signal. The associated frequencies f_j will determine how the time permutation evolves.

Suppose that the Bragg cell contains N samples of the signal as shown in Figure 4. We let $N = 8$ and show the situation at that point in time when the first frame of information has just entered the Bragg cell. Each time sample has an associated frequency which we now denote as mf_o, $|m| \leq N$; these frequencies are measured from f_c. For example, the fifth sample ($n = 5$) has an associated frequency $-3f_o$ which is just sufficient to move this time sample to the second time slot in the Fresnel plane. Sample $n = 3$ in the Bragg cell has an associated frequency $+2f_o$ which moves it to the fifth time slot in the Fresnel plane.

Since the sample positions in plane P, are a permutation of the sample positions in the input plane, there are N! ways in which the frame of N samples can be transmitted.

As shown in Figure 4, the photodetector placed at $\eta = 0$ is just ready to receive light from the frame of data. As the data flows through the Bragg cell in a continuous fashion, the samples are permuted in time. The samples from the next frame are frequency encoded, appropriate to the new permutation, while the previous frame is being transmitted. The data flow is continuous in time, provided that the cell has been fully loaded and matched in length to the frame length. The Bragg cell must be 2N samples long to accommodate the time delay required when the first sample in a frame must be moved to the end of the frame. As shown, the frequencies have been chosen to perform a particular permutation called a perfect shuffle.[5]

Shuffles and exchanges are used extensively in computer architectures for parallel processing,[5,6] such as the FFT, and circuit switching networks,[7,8,9] such as concentrators, expanders, partitioners, and sorters. We could also view the permutation scheme of Figure 4 as a means for interconnecting one set of N computers or processors with another set of size N, including some or all of its own members. In this fashion it is possible to implement operations requiring feedback. In the case shown, the first bits from each data word could be interleaved to produce a serial bit stream that modulates those frequencies synthesized under the control of the processor that determines the desired interconnection. The photodetector circuitry then deinterleaves the data and puts the bits onto the appropriate bus associated with each processor. The same permutation pattern is retained until all the bits in a word or a sequence of words have been transmitted.

The interconnection scheme can be changed at any time without interrupting the flow of data into the Bragg cell. There will be, however, variable gaps between the last bit of a word transmitted with the old setup to the first bit of a word with the new setup. Another disadvantage of this scheme is that the required electronics at the input/output are complicated. The bit rate in the Bragg cell, and therefore the bandwidth of the photodetector, is N times the bit rate of the individual processors. Finally, the light is not as efficiently used as we would like. Clearly, this scheme is more useful as a scrambler than as a crossbar switch.

We can relieve some of these problems by adding more sources and photodetectors to introduce more parallelism. Figure 5 shows a similar Bragg cell configuration, but one with a set of N light sources such as injection laser diodes which illuminate the Bragg cells via collimating lenslets; the cell is also only half as long as the one used for data permutation. We associate each source with one of the transmitting processors. These sources may be modulated with data or, in some applications, they may simply be operated in a pulsed mode upon command. We associate each photodetector with one of the receiving processors. If the subsequent processing is to be all optical in nature, the photodetectors can be replaced by optical fibers; this may be an attractive alternative anyway because the detection process can then be physically performed near the processor electronics.

The basic mode of operation is that the network controller selects the frequencies necessary to establish the desired interconnection scheme. Each of the N' interconnections can be set by an N-bit word from the controller. The binary data from the transmitting processors modulate the sources which produce a very short pulse with high peak power once per bit interval. We see that the frame rate for the Bragg cell must be equal to the bit rate from the processors.

The system shown in Figure 5 has several advantages relative to that shown in Figure 4: (1) the photodetectors bandwidth is the same as the bit rate for any particular processor instead of N times that rate (although the sources may be on for only a short period of time, the associated photodetector circuitry can be designed to be consistent with the bit time, thus reducing the noise bandwidth and improving the system performance), (2) the available light power can be used more efficiently because there are N sources and each can be operated at rated average power, (3) there is no need to interleave or deinterleave the information at the input or output, and (4) there are no gaps in the data flow when the interconnection scheme is changed.

An important feature of a switching network is the ability to implement expanders that fanout data from one processor to several processors. Such systems are more powerful because they can implement more than N! interconnections. A basic fanout is shown in Figure 6, where we see that transmitting processor T4 is connected to receiving processors R2, R4, and R6; when we fanout, we address two or more frequency synthesizers at the same time. The connection can be made without interference because optical switches are non-blocking. To avoid contention at the receiving processors, the number of transmitting processors must be less than the number of receiving processors and the controller must ensure that no receiving processor gets concurrent data. If a single transmitter is set to fanout to M receiving processors, the number of interconnect schemes is

$$\frac{N^2[(N-1)!]^2}{M[(M-1)!]^2(N-M)!} ; \qquad M>1. \tag{9}$$

Obviously, more than one transmitting processor can operate in the fanout mode, provided that contentions are resolved.

There are other possible uses for the Fresnel transform. To illustrate these, we must first distinguish between direct and heterodyne detection. In direct detection we measure the intensity of the light; the high frequency and phase information is lost in the process. In heterodyne detection we measure the amplitude of the light, with the phase information encoded on a high frequency temporal waveform. Thus, all three important parameters of the signal are retained.

The advantage of direct detection is system simplicity, and our discussions so far are based on using this detection scheme. If, for example, we were to use heterodyne detection, we could resolve contention in the fanout mode of operation. Suppose that data from T2 and T3 in Figure 6 are required concurrently at

R5. Since the required frequencies are f_2 and f_4, we can retain the identity of the transmitting processor by measuring the frequency content of the received signal. Such a feature also requires, of course, more complex detection circuitry. If we use direct detection, the magnitude at R8 is the sum of the intensities that are generated by T2 and T3 operating independently; we then lose the identity of the transmitting processor.

In some switching applications it may be useful to complete a connection only when several independent events occur concurrently. In this case we could use direct detection and comparators to set the criterion for interconnection based on magnitude only. Figure 7 shows a case where T3, T6, and T8 (which may represent one set of parts) activate R5 at some instant in time. If the port opening activity takes place during a special setup time, several ports may be opened by a combination of frequency selection and laser source selection as the signal travels through the cell.

One disadvantage of this scheme is that the bit rate, on a per channel basis, is the same as the frame rate for the Bragg cell. In Table 1 we give the relevant figure for two quite different, yet typical, Bragg cell configurations. The key parameter is the frame rate which, in both cases is much too low. The

Parameter	Case 1	Case 2
T	1μs	40μs
W	500MHz	50MHz
TW	500	2000
$N = \sqrt{0.8TW}$	20	40
Frame Rate	1MF/S	25KF/S

Table 1: Comparison of two Bragg Cells

frame rate improves as N decreases, but such concessions tend to defeat the purpose of the switch. We can increase the bit rate by introducing more channels as shown in Figure 8. Suppose that we let each channel represent one element of an M-bit word. We can now transmit one M-bit word in a frame period. To do so requires an N x M element photodetector array.

Another possible way to increase the bit rate is shown in Figure 9. A linear array of N sources (not shown) illuminate an N channel Bragg cell. The spherical/cylindrical lens creates a Fourier transform in the vertical direction while maintaining the Fresnel transform in the horizontal direction. The proper set of frequencies are applied to the Bragg cell to establish the desired interconnection. The bit rate is now determined by how fast the sources can be modulated.

Comparison to the Fourier Transform

Fresnel transforms, as applied to short temporal pulses, sort information according to the angular diffraction caused by the spatial frequency content of the data. The information can be spatially resolved if the propagation distance from the signal to the Fresnel plane is sufficiently large; this distance is dependent on the pulse length. A Fourier transform also has these properties and, since it is the far-field limiting version of a Fresnel transform, provides the maximum spatial separation of the angular components of the signal. How, then, do these two transforms compare?

The key difference between these transforms is that the Fresnel transform retains a direct space-to-time dependence; that is, the time at which data arrives at a detector is a function of both its frequency and position. It is therefore possible to reorder data in a sequence as we showed in Figure 4. Such an arbitrary permutation cannot be done using the Fourier transform and a single detector.

The interconnection schemes shown in Figure 5 and 6 can be achieved with the Fourier transform except that the frequency encoding scheme is different. The applied frequency is a function of only the destination in the Fourier transform mode whereas it is a function of both the source and the destination in the Fresnel transform mode. It is not, therefore, possible to identify the source processors when using either direct or heterodyne detection. There are, therefore, some similarities and differences between the Fresnel and Fourier transforms. Which is more useful requires more detailed analysis for a given application.

Summary

Fresnel transforms, coupled with the use of Bragg cells, can implement dynamic interconnection schemes that may be useful in computer architectures. The fact that they are one-dimensional devices may not pose a problem since optical fibers can be used to distribute information from the switch point to the destination. Two-dimensional extensions of these schemes are obvious, with a multi-channel configuration being most useful. All possible permutations can be implemented, avoiding some of the limitations associated with repeated use of algorithms such as the perfect shuffle.

This work was supported by the U. S. Army Research Office.

References

1. A. VanderLugt, "Fresnel Transforms and Bragg Cell Processors", Appl. Opt., Vol. 24, p. 3846 (1985).

2. J. W. Goodman, F. J. Leonberger, S-Y. Kung, and R. A. Athale, "Optical Interconnections for VLSI Systems," Proc. IEEE, vol. 72, p. 850 (1984).

3. I. C. Chang, "Acoustooptic Devices and Applications," IEEE Trans. Sonics and Ultrason.", Vol. SU-23, p. 2 (1976).

4. A. D. Wyner, "An Analog Scrambling Scheme Which Does Not Expand Bandwidth, Part I: Discrete Time", IEEE Trans. Inform. Theory, Vol. IT-25, p. 261 (1979); also Part II: Continuous Time, IEEE Trans. Inform. Theory, Vol. IT-25, p. 415 (1979).

5. H. S. Stone, "Parallel Processing with the Perfect Shuffle", IEEE Trans. Comp., Vol. C-20, p. 153 (1971).

6. R. J. Polge, B. K. Bhagavan, and J. M. Carswell, "Fast Computational Algorithms for Bit Reversal," IEEE Trans. Comp., Vol. C-23, p.1 (1974).

7. G. M. Masson, G. C. Gingher, and S. Nakamura, "A Sampler of Circuit Switching Networks," Computer Vol. 12, p. 32 (1979).

8. D. S. Parker, Jr., "Notes on Shuffle/Exchange-Type Switching Networks," IEEE Trans. Comp., Vol. C-29, p. 213 (1980).

9. T. Feng, "A Survey of Interconnection Networks," Computer, Vol. 14, p. 12 (1981).

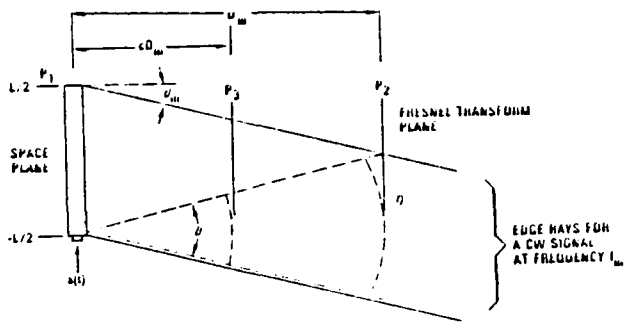

Fig. 1 Fresnel Transform

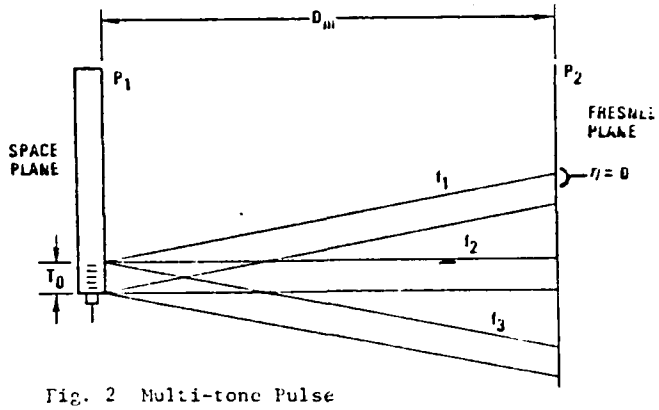

Fig. 2 Multi-tone Pulse

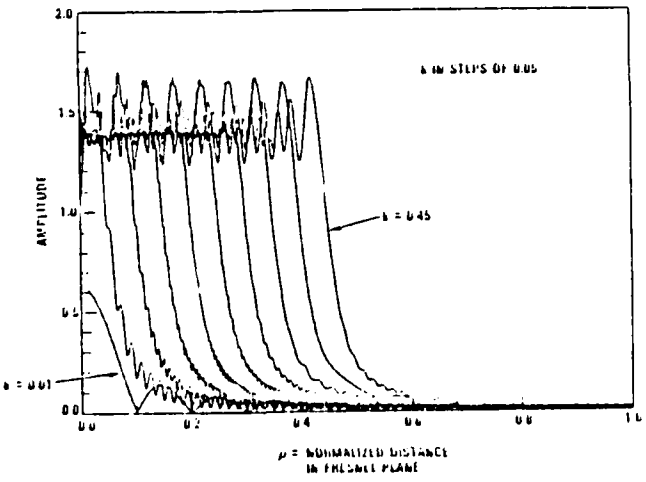

Fig. 3 Transforms of Pulses

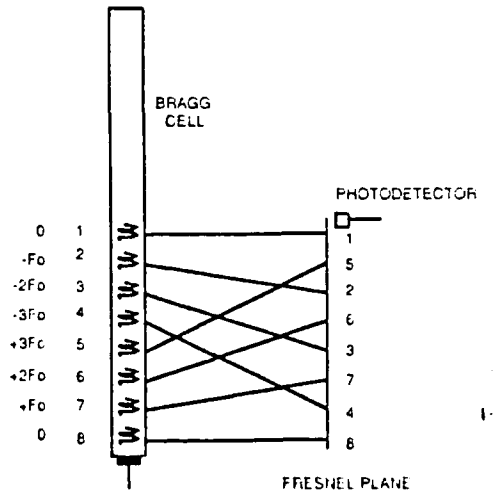

Fig. 4 Basic Permutation Scheme

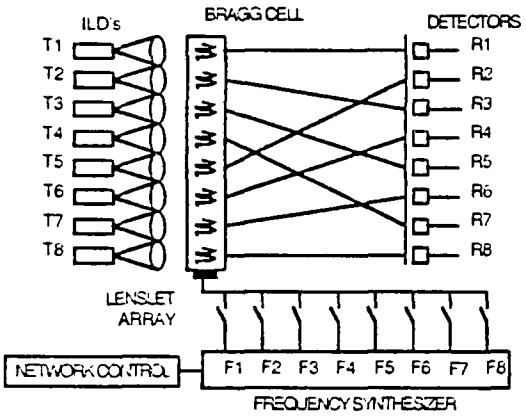

Fig. 5 Switch Connection - Perfect Shuffle

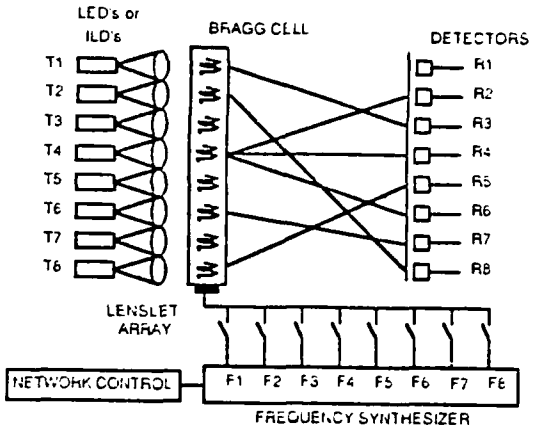

Fig. 6 Switch Connection - Fan out

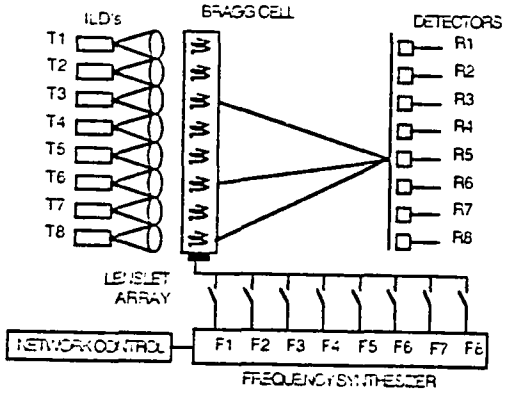

Fig. 7 Switch Connection - Fan in

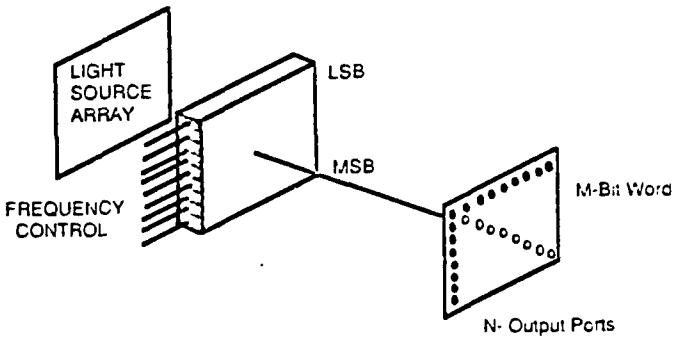

Fig. 8 Multichannel Approach

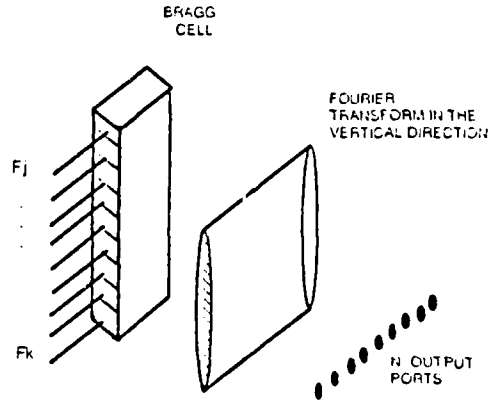

Fig. 9 Fresnel/Fourier Transform

APPENDIX H

ACOUSTIC SPREADING IN MULTICHANNEL BRAGG CELLS

REPRINTED FROM SPIE CONFERENCE

ON SPATIAL LIGHT MODULATORS AND APPLICATIONS

VOLUME 465, PAGE 152, 1984

Reprinted from SPIE Vol. 465—Spatial Light Modulators and Applications

Acoustic spreading in multichannel Bragg cells

A. VanderLugt, G.S. Moore, and S.S. Mathe

Harris Corporation, Government Systems Sector,
P.O. Box 37, Melbourne, Florida 32901

Abstract

In some applications, the performance of multichannel Bragg cells is compromised by the spreading of the acoustic waves as they propagate; the spreading causes the signals in the channels to overlap. The overlapping can be significantly reduced by a spatial filter in a Fourier/image plane; the spatial filter is shown to be equivalent to a cylindrical lens whose power is a function of the distance from the transducer.

Introduction

In some signal processing applications, multichannel Bragg cells are required to handle wideband parallel signals. One example is that of processing signals from a phased array antenna wherein we associate each channel of the Bragg cell with an antenna element. Multichannel Bragg cells were developed in the early 1960's by Lambert and his associates[1,2], and cells with as many as 128 channels have been described[3]. As the channels become more densely packed, the transducer heights are reduced causing the acoustic energy to spread over larger angles as it propagates through the interaction material. The acoustic waves from adjacent channels therefore overlap after a short propagation distance; if the overlapping could be compensated so that the diffracted light from each channel is confined to that channel, a more widely useful multichannel Bragg cell would result. We show how this can be achieved with a holographic element.

Theory

The model that we use for analyzing the acoustic spreading is the same as that used before[4] and is shown in Figure 1. An electrical signal drives a piezoelectric transducer having height H and an interaction width W. The transducer launches an acoustic wave within the Bragg cell which changes the index of refraction; this, in turn, causes the phase of light from a coherent source to be modulated in space and time. If the drive signal is an RF signal at frequency f_c, the acoustic wavelength is $\Lambda_c = V/f_c$, where V is the velocity of sound in the medium.

The acoustic wavefronts propagate in a fashion similar to optical wavefronts derived from a line source ($H \rightarrow 0$). If $W \gg H$, we can model the wavefronts as cylindrical sheets which, for an isotropic medium, spread at an angle $\pm\phi$ with respect to the x-axis. The degree to which acoustic spreading occurs is a function of the anisotropy of the medium, the acoustic wavelength, and the transducer height.

The first step is to calculate the Fourier transform of a single channel Bragg cell driven as shown in Figure 1. We wish to derive the transform in the y-direction only, while we image the Bragg cell in the x-direction. We begin by considering the transducer to be an infinitesimal line source and account for its finite height by multiplying the Fourier transform by a sinc-function. The Fourier integral to be solved is[4]

$$G(x,\xi) = \frac{1}{j\lambda x}\int_{-\phi_0 x}^{\phi_0 x} \exp[-j2\pi y^2/2\Lambda x(1-2s)]\exp(-j2\pi\xi y/\lambda)\,dy. \qquad (1)$$

where ξ is the angular spatial frequency, s is a parameter that characterizes the degree of anisotropy as given by the elastic constants,[4,5] Λ is the wavelength of the acoustic wave within the medium, and λ is the wavelength of light. The region of integration is over a wedge whose apex is at x = 0 and ϕ_0 is the angle at which the acoustic beam has its first nulls. The far field value of ϕ_0 is[6]

$$\phi_0 = \Lambda(1-2s)/H \qquad (2)$$

In reference 4, we solved (1) in terms of error functions having complex valued arguments. An equivalent result that is somewhat simpler to derive and provides more physical insight can be obtained through the use of Fresnel integrals. We let

$$\left.\begin{aligned} c &= \pi/\Lambda x(1-2s) \\ d &= \pi\beta/\lambda \end{aligned}\right\} \tag{3}$$

so that

$$G(x,\beta) = \frac{1}{\sqrt{j\Lambda x}} \int_{-\phi_o x}^{\phi_o x} \exp[-j(cy^2+2dy)]dy \tag{4}$$

By completing the square of the exponential and by changing variables, we obtain

$$G(x,\beta) = \frac{1}{\sqrt{j\Lambda x}} \exp(jd^2/c)\ \mathrm{sinc}(\beta H/\lambda) \int_a^b \exp(-ju^2)du, \tag{5}$$

where $a = -\phi_o x\sqrt{c} + d/\sqrt{c}$, $b = \phi_o x\sqrt{c} + d/\sqrt{c}$, and $\mathrm{sinc}(\beta H/\lambda)$ is the multiplicative factor needed to account for the finite height of the transducer. The integral is a Fresnel integral that further modifies the amplitude of $G(x,\beta)$. Depending on the values of the limits, this function may be nearly rectangular (similar to the near field diffraction pattern of a slit).

If we denote the total amplitude weighting of $G(x,\beta)$ by $f(x,\beta)$, we have that

$$G(x,\beta) = f(x,\beta)\exp[j\pi x\Lambda(1-2s)\beta^2/\lambda^2]. \tag{6}$$

We now concentrate on the phase part of $G(x,\beta)$. The key point is that the phase factor is quadratic in β and linear in x. At the transducer, where $x = 0$, there is no optical power, whereas the optical power is greatest at $x = L$. If the optical power could be canceled, the inverse Fourier transform would confine the light to rectangular channels with no spreading into adjacent channels. In principle, the optical power can be compensated by a section of a conical lens whose power varies linearly from zero, at $x = 0$, to a value of $L\Lambda(1-2s)/\lambda F^2$ at $x = L$. An alternative method is to construct a holographic correcting element from one channel of the Bragg cell; such an element will then correct the acoustic spreading for all channels simultaneously in the same fashion as would a matched filter (See Figure 2).

The use of a holographic element for comensating the acoustic spreading has been reported by Vodovatov, et al[7]. The derivation given there for the value of $G(x,\beta)$ does not agree with (6), particularly with respect to the phase factor having quadratic dependence on β and linear dependence on x. The result from (6) however, is consistent with the observation that the channels can be separated by focusing at a different plane using auxiliary optics.

Experiments

We constructed a holographic element from one channel of a 32-channel Bragg cell. This cell has a nominal bandwidth Δf = 80 MHz at a center frequency f_c = 135 MHz. The cell is fabricated from telurium dioxide material having a longitudinal velocity of 4.2 Km/sec. The active length of the crystal is L = 6 mm so that the time delay is ~1.5usec and the time-bandwidth product is ~120. The transducers have heights equal to 100 μm and they are placed on 250 μm center spacings. The acoustic wavelength at the center frequency is 31 μm. The light source is a 10 mW He-Ne laser for which λ = 632.8 nm. The holographic element was constructed on a SO-120 glass plate with a reference-to-signal beam ratio of unity near $x = 0$.

Figure 3 shows the uncorrected and the corrected output when channels are driven at the frequency corresponding to Λ_o. Figure 3a shows the degree of acoustic spreading for the uncorrected case. Of the twelve channels available, we drove the top channel to illustrate how rapidly the acoustic energy spreads and the bottom four channels to illustrate how the beams overlap and add coherently. We see that the beams are well separated only in the region near the transducer as noted earlier. If we wish to process a significant amount of time history, we find that the beams begin to overlap at a position that is only 10% of the available aperture. Figure 3b show the corrected output; we see that there is very little evidence of beam spreading and that the light has been confined to within channel heights as determined by the transducers. The amount of beam spreading is a function of the drive frequency; it is greatest at the low frequency band edge (due to a large Λ) and least at the high frequency band edge (where Λ is small).

Summary and Conclusions

We have shown that the effects of acoustic spreading within the Bragg cell can be compen-

sated in the sense that the diffracted light can be more nearly contained within channels as defined by the transducers. The results show that the best performance, in terms of correcting for the acoustic spreading is obtained when we use a Bragg cell interaction medium that has a large value of s. The correction for acoustic spreading can also be improved by a factor of two if the correction is optimized at the midpoint of the cell.

The use of a holographic corrector plate for the acoustic spreading, as well as a broader understanding of the basic diffraction patterns, opens the way for new application of multichannel Bragg cells. As the bandwidths of communication and collection systems increase, the need for such devices will expand because they help utilize the full parallel processing capabilities of optical systems. Multichannel cells may also find application in matrix/vector and matrix/matrix computing systems. A more complete discussion of this method for compensating for acoustic spreading is given in reference 9.

Acknowledgement

This work was supported by the U.S. Army Research Office.

References

1. L.B. Lambert, IRE Nato Conv. Record, Vol. 10, Part 6 (1962).
2. L.B. Lambert, M. Arm and A. Aimette, "Optical and Electro-Optical Information Processing," Ed. J.T. Tippett, et al, MIT Press, 1965.
3. A.M. Bardos, Appl. Opt., Vol. 13, p. 832 (1974).
4. A. VanderLugt, Appl. Opt., Vol. 21, p. 1092 (1982).
5. P.C. Waterman, Phys. Rev., Vol. 113, p. 1240 (1959).
6. M.G. Cohen, J. Appl. Phys., Vol. 35, p. 3621 (1967).
7. I.A. Vodovatov, N.A. Esepkins, V. Yu Petrun'kin, and S.A. Rogov, Pis'ma Zh. Tekh. Fiz, Vol. 7, p. 369 (1981). Appears in the American Institute of Physics translation of Sov. Tech. Phys. Lett. 7(3), 1981, page 159.
8. J.B. Thomas, Statistical Communication Theory, John Wiley & Sons, N.Y., 1969, p. 388.
9. A. VanderLugt, G.S. Moore, and S.S. Mathe, Appl. Opt., Vol. 22, p. 3906 (1983).

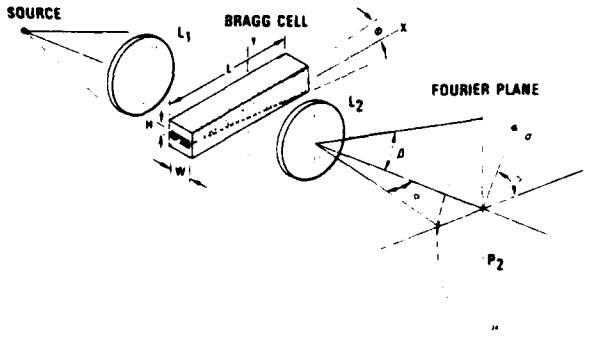

Figure 1. Model for Acoustic Spreading in a Bragg Cell

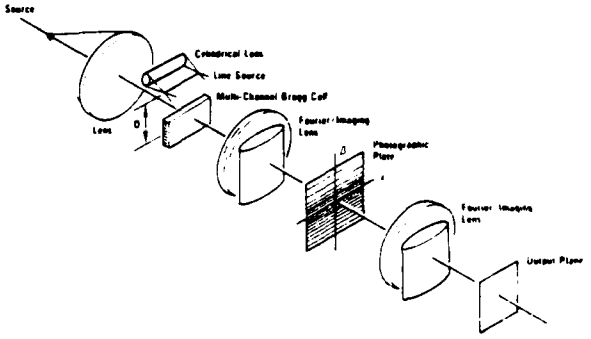

Figure 2. Optical System for Constructing the Holographic Element and Correcting the Acoustic Spreading

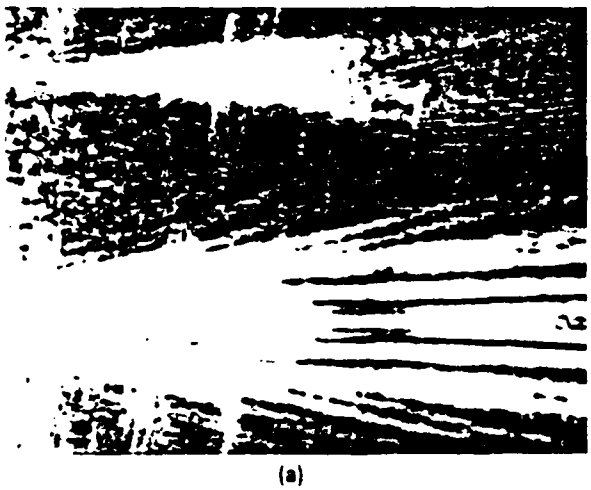

(a)

Uncorrected Case Showing Beam Overlap

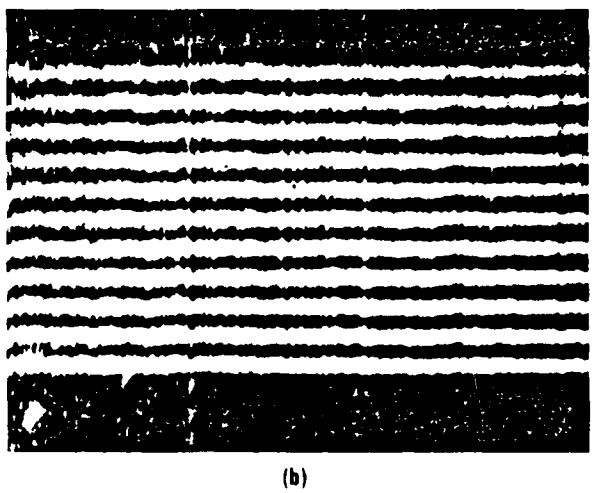

(b)

Corrected Beams at Optimum Acoustic Wavelength (123 MHz)

Figure 3. Multichannel Bragg Cell Diffraction Beams

END

2-87

DTIC